

Argonne National Laboratory

ARGONNE ADVANCED RESEARCH REACTOR CRITICAL EXPERIMENTS

by

K. E. Plumlee, J. W. Daughtry,
T. W. Johnson, W. R. Robinson,
R. A. Schultz, and G. S. Stanford

PROPERTY OF
ARGONNE NATIONAL LAB
LIBRARY

The facilities of Argonne National Laboratory are owned by the United States Government. Under the terms of a contract (W-31-109-Eng-38) between the U. S. Atomic Energy Commission, Argonne Universities Association and The University of Chicago, the University employs the staff and operates the Laboratory in accordance with policies and programs formulated, approved and reviewed by the Association.

MEMBERS OF ARGONNE UNIVERSITIES ASSOCIATION

The University of Arizona
Carnegie-Mellon University
Case Western Reserve University
The University of Chicago
University of Cincinnati
Illinois Institute of Technology
University of Illinois
Indiana University
Iowa State University
The University of Iowa

Kansas State University
The University of Kansas
Loyola University
Marquette University
Michigan State University
The University of Michigan
University of Minnesota
University of Missouri
Northwestern University
University of Notre Dame

The Ohio State University
Ohio University
The Pennsylvania State University
Purdue University
Saint Louis University
Southern Illinois University
University of Texas
Washington University
Wayne State University
The University of Wisconsin

LEGAL NOTICE

This report was prepared as an account of Government sponsored work. Neither the United States, nor the Commission, nor any person acting on behalf of the Commission:

A. Makes any warranty or representation, expressed or implied, with respect to the accuracy, completeness, or usefulness of the information contained in this report, or that the use of any information, apparatus, method, or process disclosed in this report may not infringe privately owned rights; or

B. Assumes any liabilities with respect to the use of, or for damages resulting from the use of any information, apparatus, method, or process disclosed in this report.

As used in the above, "person acting on behalf of the Commission" includes any employee or contractor of the Commission, or employee of such contractor, to the extent that such employee or contractor of the Commission, or employee of such contractor prepares, disseminates, or provides access to, any information pursuant to his employment or contract with the Commission, or his employment with such contractor.

Printed in the United States of America
Available from

Clearinghouse for Federal Scientific and Technical Information
National Bureau of Standards, U. S. Department of Commerce
Springfield, Virginia 22151

Price: Printed Copy \$3.00; Microfiche \$0.65

ARGONNE NATIONAL LABORATORY
9700 South Cass Avenue
Argonne, Illinois 60439

ARGONNE ADVANCED RESEARCH REACTOR
CRITICAL EXPERIMENTS

by

K. E. Plumlee, J. W. Daughtry,
T. W. Johnson, W. R. Robinson,
R. A. Schultz, and G. S. Stanford

Reactor Physics Division

February 1969

TABLE OF CONTENTS

	<u>Page</u>
ABSTRACT	17
I. SUMMARY	17
II. INTRODUCTION.	19
III. DESCRIPTION OF CORE ASSEMBLIES	20
IV. INTERNAL THERMAL COLUMN EXPERIMENTS.	27
A. Measurement of Flux-to-Power Ratios	27
1. Purpose	27
2. Summary of Results	27
3. Thermal Cross Sections for Gold and Uranium in the ITC	30
4. Effect of Errors in Measuring Cadmium Ratios and in Estimating Cadmium Cutoff Energy	31
5. Foil Self-shielding and Outer Flux Depression.	33
6. Flux Determinations	34
7. Absolute Determination of Total Core Power	34
B. Measurement of Neutron Temperature and Epithermal Index in ITCs by Cadmium Ratios	38
C. Reactivity Worths of Boron and Cadmium Absorbers in the ITC	42
D. Experiments with Aluminum, Beryllium, and Teflon in the ITC	44
E. Void Experiments in the ITC.	47
V. RELATIVE ACTIVATION AND POWER-DISTRIBUTION MEASUREMENTS.	52
A. Purpose.	52
B. Experimental Method	52
C. Horizontal Activation Distributions.	54
1. Effect of Increased Fuel Loading Densities	54
2. Radial Traverses Out to 152 cm	59
3. Flux-tilting Investigation	61
4. Foil Traverses inside Beam Tubes	63
5. Effect of Beryllium in the ITC.	65
6. Power Density in the Graded Loading, Assembly 5	66

TABLE OF CONTENTS

	<u>Page</u>
D. Vertical Activation Distributions	69
1. Effect of Reactor Operating Conditions	69
2. Effect of Increased Height of Beryllium Reflector. . . .	73
3. Influence of a Peripheral Blade on the Flux in the Reflector.	73
4. Effect of Voiding the ITC	75
E. Detailed Mapping near Control Blades.	76
F. Determination of an Improper Fuel Loading	77
VI. CADMIUM-RATIO MEASUREMENTS.	79
VII. NEUTRON-DENSITY MEASUREMENTS NEAR MOCKED-UP AARR PRESSURE VESSEL, BEAM TUBE, AND SHROUD. . . .	84
A. Flux Level at Location of AARR Startup Instruments	84
B. Startup Instrument Response to a Startup Source.	86
C. Radial Flux Perturbation near Beam Tubes	88
VIII. BEAM-TUBE YIELDS, REACTIVITY REQUIREMENTS, AND INTERACTIONS	94
A. Introduction	94
B. Yield and Reactivity Measurements with Horizontal Beam Tube.	94
1. Description of Beam Tubes.	94
2. Foil Activation Measurements in Beam Tubes	96
3. Use of BF ₃ Counter in Measuring Beam-tube Yields in 10.16-cm-sq Beam Tubes	99
4. Experiments with Plastic Slabs at Beam-tube Tip. . . .	100
5. Reactivity Losses Associated with Beam Tubes	103
C. Experiments with a Vertical Beam Tube	105
D. Effects of Flooding Beam Tubes.	107
E. Beam-tube Interaction Experiments	107
F. Status of Equipment Obtained for Future Experiments . . .	110

TABLE OF CONTENTS

	<u>Page</u>
IX. EXPERIMENTS WITH CONTROL AND SAFETY BLADES, VARIOUS ABSORBERS, AND ^{235}U ALUMINUM COUPONS	113
A. Introduction	113
B. Calibrations of Standard Hafnium Control and Safety Blades	114
1. Standard Blade Dimensions and Locations	114
2. Shadowing of Blade Worths	115
3. Worths of Standard Hafnium Blades with Aluminum Followers	116
4. Conclusions	117
C. Reactivity Worths of Thin Hafnium Blades	117
1. Description of Thin Blades	117
2. Purpose of the Thin-blade Experiments	118
3. Comparison of Thin and Standard Blades	118
D. Reactivity Worths of Thick Hafnium Blades	119
1. Purpose of Measurement	119
2. Description of Thick Blades	119
3. Comparison of Thick and Standard Peripheral Blades in Assembly 4b.	119
E. Dependence of Worths of Standard Hafnium Blades on Temperature and on ITC Void Fraction	120
1. General Nature of Dependence	120
2. Calibrations of Blades No. 6 and 10 in Assembly 4a	120
3. Calibration of Banked Blades 7-12 in Assembly 5	121
4. Conclusions	121
F. Comparison of Aluminum and Stainless Steel Blade Followers	121
1. Purpose of Comparison	121
2. Measured Loss of Reactivity-control Worth on Substitution of Stainless Steel for Aluminum Blade Followers	122
G. Measurements Related to Attachment of Beryllium Reflector to Safety-blade Follower	122
H. Experiments with an ITC Safety-liner Mockup	123

TABLE OF CONTENTS

	<u>Page</u>
I. Experiments with Europium Control-blade Specimen	124
1. Purpose	124
2. Description of Europia-Stainless Steel Plates	125
3. Measured Worths of Samples	126
4. Conclusions	128
J. Reactivity Worths of Small Samples in the AARR Critical Assemblies	129
1. Introduction	129
2. Description of Samples and Methods of Measurement	129
3. Measured Worths of Samples	131
4. Conclusions	132
K. Reactivity-period Constants Used for Rising-period Measurements of Reactivity	134
X. MEASUREMENTS OF TEMPERATURE COEFFICIENTS AND RADIAL-H ₂ O VOID WORTHS	136
A. Introduction	136
B. Results of Temperature-coefficient Measurements with ITCs Flooded	137
C. Temperature-coefficient Measurement in Assembly 3 with Massive Void in ITC	139
D. Measurements of Radial Void Worths	140
1. Simulation of Small Voids by Teflon	140
2. Volume-averaged Void Worths	141
3. Distributions of Radial Void Worths	142
E. Estimated Effects of Thermal Expansion on Temperature Coefficient	144
1. Expansion of Core Structure with Temperature	144
2. Expansion of Water with Temperature	144
3. Conclusions	145
XI. MISCELLANEOUS MEASUREMENTS	146
A. Measurement of Prompt-neutron Lifetime by Rossi-alpha Technique	146
B. Pulsed-neutron Measurements	147

TABLE OF CONTENTS

	<u>Page</u>
C. Measurement of Gamma-radiation Heating by Thermoluminescent Dosimetry	150
D. Experiments to Confirm Loading Predictions	153
E. Fast-neutron Yields from Beam Tubes	155
1. Measurement of the Fast-neutron Yield of a Tangential Beam Tube	155
2. Comparison of the Fast-neutron Yields from a Radial Beam Tube and a Tangential Beam Tube	156
ACKNOWLEDGMENTS	159
REFERENCES	160

LIST OF FIGURES

<u>No.</u>	<u>Title</u>	<u>Page</u>
1.	Plan View of AARR Critical Facility	21
2.	Sectional View of AARR Critical Facility	22
3.	Fuel Bundle Assembly.	23
4.	Fuel Plate Assembly.	24
5.	Small ITC.	28
6.	Large ITC.	29
7.	Plot of Trial (r) for Determination of Neutron Temperature in Large AARR ITC	39
8.	Sample Positions in the Small and Large ITCs, Used for Boric Acid, Cadmium, Aluminum, and Teflon Samples	43
9.	Reactivity Worth of Various Sizes of Absorbers in ITC of Assembly 4a	43
10.	Radial Distribution of Boric Acid Worth in ITCs of Assemblies 3 and 4a.	44
11.	Large Aluminum ITC with Beryllium Liners	47
12.	Void Location in Small ITC	48
13.	Void Location in Large ITC	48
14.	Reactivity Change upon Flooding Voided Tubes in the Small ITC of Assembly 3, for Sequences Shown in Table XVI	50
15.	Reactivity Effect of Large Partial Voidings of Small and Large ITC of Assemblies 4a and 4b.	51
16.	Retaining Method for 0.05-cm-diam Uranium-Aluminum Wires in AARR Critical Assemblies	53
17.	Manganese Radial Activation Traverses in Assembly 1.	54
18.	Manganese Radial Activation Traverse in Assembly 2a.	54
19.	Manganese Radial Activation Traverses in Assembly 2b	55
20.	Manganese Radial Activation Traverses in Assembly 3.	55
21.	Typical Foil Placement for Radial and Vertical Activation Traverses.	55
22.	Uranium-Aluminum Fission Traverses in Assembly 2b.	56

LIST OF FIGURES

<u>No.</u>	<u>Title</u>	<u>Page</u>
23.	Radial Fission Traverses in Assembly 3	57
24.	Radial Fission Traverses in Assembly 4a.	57
25.	Radial Fission Traverses in Assembly 4b.	58
26.	Radial Fission Traverses in a Graded Loading with the Large ITC (Aluminum ITC Shroud) in Assembly 5	58
27.	Radial Traverses with Indium Foils in Assembly 3.	60
28.	Radial Traverse with Indium Foils in Assembly 4a through Simulated Pressure Vessel	61
29.	Foil Locations for Flux Tilt Investigation with Manganese Foils in Assembly 3	61
30.	Flux Tilt Investigation with Manganese Foils in Assembly 3. . .	61
31.	Foil Placement for Radial Activations with Manganese Foils in Assembly 3	62
32.	Radial Activation Traverses with Manganese Foils in Assembly 3.	62
33.	Foil Locations in a Cross-sectional View of the Beam Tubes with Beam Tubes Voided.	63
34.	Foil Locations in a Cross-sectional View of the Beam Tubes with Beam Tubes Filled with Beryllium.	63
35.	Radial Traverses with Manganese Foils in Assembly 3 with Beam Tubes Voided	64
36.	Radial Traverses with Manganese Foils in Assembly 3 with Beryllium Filler Plugs in the Beam Tubes	64
37.	Traverse with Manganese Foils in the Through Tube in Assembly 3 with Beryllium Filler Plugs in the Through Tube. .	65
38.	Plan View of Cores Containing Enlarged ITC.	65
39.	Radial Fission Traverses through Beryllium Columns in the Large ITC	66
40.	Radial Fission Traverses through Beryllium Liners in the Large ITC.	66
41.	Approximate Channel Locations near the ITC in Assembly 5 . .	67
42.	Peripheral Subassemblies with Approximate Channel Locations, Assembly 5	67

LIST OF FIGURES

<u>No.</u>	<u>Title</u>	<u>Page</u>
43.	^{235}U Fission Distribution and Power Density for Regions of Fig. 41, as Measured with Wires through the Graded Section of Assembly 5	68
44.	^{235}U Fission Distribution and Power Density for Region 2, Fig. 42, as Measured with Wires through the Graded Section of Assembly 5 and Compared to Data from Assembly 4a	68
45.	^{235}U Fission Distribution and Power Density for Region 3, Fig. 41, as Measured with Wires in Assembly 5.	68
46.	^{235}U Fission Distribution and Power Density for Region 4, Fig. 42, as Measured with Wires through the Graded Section of Assembly 5	68
47.	Channel and Wire Locations near Fuel-foil Edges	69
48.	Vertical Fission Traverses in Assembly 3	70
49.	Vertical Fission Traverses for Assembly 4a.	71
50.	Vertical Fission Traverses for Assembly 4b.	71
51.	Vertical Activation Traverses with Manganese Foils in Assembly 3.	71
52.	Vertical Fission Traverse for Assembly 5; Graded Loading and Large Aluminum ITC, for Water Level Control	72
53.	Vertical Fission Traverse for Assembly 5; Graded Loading and Large Aluminum ITC.	72
54.	Locations of Vertical Activation Measurements in the Beryllium Reflector Region in Assembly 3	73
55.	Vertical Activation Traverse with Manganese Foils in the Beryllium Reflector Region of Assembly 3	74
56.	Vertical Activation Traverses with Manganese Foils in the Beryllium Reflector Region of Assembly 3; Beryllium Height 35 in.	74
57.	Vertical Activation Traverses with Manganese Foils in the Beryllium Reflector Region of Assembly 3; Hafnium Blade Tip 1-1/2 in. below the Top of the Fuel Region, Beryllium Height 31 in.	74
58.	Vertical Activation Traverses with Manganese Foils in the Beryllium Reflector of Assembly 3; Hafnium Blade Tip at the Core Midplane, Beryllium Height 19 in.	75

LIST OF FIGURES

<u>No.</u>	<u>Title</u>	<u>Page</u>
59.	Vertical Activation Traverses with Manganese Foils in the ITC under Flooded and 74% Voided Conditions in Assembly 3	75
60.	Vertical ^{235}U Fission Distributions as Measured with Wires near Half Inserted Control Blades in Assembly 4a	76
61.	^{235}U Fission Distribution as Measured with Wires near Control Blade Followers in Assembly 4a	77
62.	Positions where Cadmium Ratios Were Measured.	79
63.	Fission Cadmium Ratio as a Function of Lattice Moderating Ratio	81
64.	Cadmium Ratio of Dysprosium as a Function of Lattice Moderating Ratio	81
65.	Cadmium Ratio for 1.2-mil Indium as a Function of Lattice Moderating Ratio	82
66.	Cadmium Ratio for 1.1-mil Gold as a Function of Lattice Moderating Ratio	82
67.	Cadmium Ratio for Manganese as a Function of Lattice Moderating Ratio	82
68.	Cadmium Ratio for Copper as a Function of Lattice Moderating Ratio	82
69.	Composite Radial Traverse with Various Neutron Detectors . .	84
70.	Effect of Extending a "Neutron Window" in the Radial Direction	85
71.	Effect of Inclusion of H_2O in Aluminum Window	86
72.	Top View of AARR Critical Core with Mockup of Shroud, Pressure Vessel and Beam Tube.	89
73.	Effect of Aluminum Braces on Flux Distribution	90
74.	Traverse in Plane above Beam Tube	90
75.	Vertical Traverse at Radius of 67 cm	90
76.	Vertical Traverse behind Armor Plate.	90
77.	Traverses before Installation of Aluminum Shroud.	91
78.	Close-in Effect of Extending Beam Tube.	91
79.	Effect of Extending Beam Tube	92

LIST OF FIGURES

<u>No.</u>	<u>Title</u>	<u>Page</u>
80.	Traverses Parallel to Extended Beam Tube in Midplane	92
81.	Initial Installation of Beam Tubes	95
82.	Positions of Beam Tubes and Beryllium Fillers.	96
83.	Arrangements of Beam Tubes and Collimators	97
84.	Relative Subcadmium Activations with Indium Foils at Ends of Beam Tubes	98
85.	Indium Cadmium Ratios Using Different Beam Tube Geometries	98
86.	Tangential Beam Tube: Relative Yield vs Penetration into Beryllium Reflector	99
87.	Tangential Beam Tube: Relative Yield vs Penetration into Reflector, with Lucite Tip	100
88.	Initial Configuration for Relative Yield Measurements	100
89.	Arrangement for Measuring Yields, with Lucite at the Tip of a Beam Tube	101
90.	Relative Neutron Yield as a Function of Lucite Slab Thickness	101
91.	Reactivity Loss vs Depth of Beam-tube Penetration into Beryllium Reflector	104
92.	Through-tube Configuration for Measuring Reactivity Worth of 12-in.-long Beryllium Plug.	104
93.	Through-tube Configuration for Measuring Reactivity Worth of 4-in.-long Lucite Plug	104
94.	Reactivity Worth of 12-in.-long Beryllium Plug along Through Tube	105
95.	Reactivity Effect of 4-in.-long Lucite Insert in Through Tube	105
96.	Arrangement for Measuring Yields, with Adjustable Water Depth in a Vertical Beam Tube	106
97.	Relative Neutron Yield as a Function of Lucite or Water Thickness in a Vertical Beam Tube	106
98.	Cross Section of Beam Tubes and Reflector Used in Interaction Measurements	108
99.	Configurations of Beam-tube Contents in Vertical Interaction Measurements, Cases 1 and 2	108

LIST OF FIGURES

<u>No.</u>	<u>Title</u>	<u>Page</u>
100.	Configurations of Beam-tube Contents in Vertical Interaction Measurement, Case 3	108
101.	Configurations of Beam-tube Contents in Radial Interaction Measurement	109
102.	Measurement of Radial Interaction between Beam Tubes	109
103.	Plan View of Proposed Radial Reflector and Beam Tubes	110
104.	Elevation View of Proposed Radial Reflector and Beam Tubes	111
105.	Diagram Showing Blade Numbers and Special Control-blade Orientations 4a and 8a.	114
106.	Calibrations of Blade No. 6 with Different Temperatures and ITC Void Fractions in Assembly 4a	120
107.	Blade Worths at 26 and 65°C in Assembly 5.	121
108.	Europia-Stainless Steel Blade Assembly.	126
109.	Cadmium Sample Worth vs Thickness	132
110.	Hafnium Sample Worth vs Thickness	132
111.	Worths of Various Samples Traversed from Midplane of Assembly 4a through Bottom Reflector.	133
112.	Trends in Worths of Small Samples as Fuel Loadings Increased	134
113.	Plots of Reactivity vs Temperature in Assembly 2a	137
114.	Plots of Reactivity vs Temperature in Assembly 3.	138
115.	Plots of Reactivity vs Temperature in Assembly 4a	138
116.	Plots of Reactivity vs Temperature in Assembly 5.	138
117.	Plots of Reactivity vs Temperature with ITC Voided and Flooded, in Assembly 3	140
118.	Average Void Worths in Assemblies 1, 2a, 3, and 4a.	142
119.	Radial Dependence of Void Worth in Assembly 3	142
120.	Top View of AARR Critical Facility.	146
121.	Sectional View of AARR Critical Facility Showing Reactor and Pulsed-neutron Generator	147
122.	Schematic Diagram of Time-analysis System	148

LIST OF FIGURES

<u>No.</u>	<u>Title</u>	<u>Page</u>
123.	Response Curves a, b, and c (Left to Right) for Detector Positions	149
124.	Measured and Calculated Gamma-ray Heating outside the Core	152
125.	Loss of Reactivity When a 27/54 Type Subassembly Replaced an A Type 14/10 Subassembly in Assembly 2a	153
126.	Gain of Reactivity When a 27/27 Type Subassembly Replaced an A or B Type in Assembly 2a.	154
127.	Estimated Numbers of Boron-Stainless Steel Pieces for Reactivity Matching of 27-fuel-foil Subassembly to A or B Type Subassemblies in Assembly 2a	154
128.	Position of Detector, Collimator, and Through Tube during Measurement of Fast-neutron Yield for Tangential Beam Tube	155
129.	Yields of Fast Neutrons for Tangential Beam Tubes	156
130.	Neutron-energy Distribution, Emergent from Radial Beam Tube of HFIR	157
131.	Neutron-energy Distribution, Emergent from Tangential Beam Tube of HFIR	158

LIST OF TABLES

<u>No.</u>	<u>Title</u>	<u>Page</u>
I.	Basic Core Loadings	20
II.	Fuel-foil Description	25
III.	Calculated Relative Group Fluxes near Center of ITC	30
IV.	Effective Thermal Group Cross Sections for ITC	31
V.	Effective Gold and Uranium Thermal-absorption Cross Sections in ITCs for Various Loadings	31
VI.	Measured ITC Fluxes for Assemblies 3, 4a, 4b, and 5	34
VII.	Measured Reactor Power, and ITC Thermal-neutron Flux per Watt	37
VIII.	Cadmium Ratios in ITC and Correction to Infinite Dilution	39
IX.	Use of Activation Cadmium Ratios in Determining Neutron Temperature (T_n) and Epithermal Index (r)	40
X.	Reactivity of Boric Acid and Lucite in ITC of Assembly 3	43
XI.	Reactivity of Boric Acid in ITC of Assembly 4a	43
XII.	Reactivity of Cadmium Tubes in ITC of Assembly 4a	44
XIII.	Reactivity of Aluminum and Teflon in ITC of Assembly 3	45
XIV.	Reactivity Coefficients of Beryllium and Teflon in ITC of Assembly 4b	45
XV.	Effect of Aluminum Wall and Beryllium in ITC of Assembly 4b	46
XVI.	Reactivity Effects of Flooding Void Tubes in Small ITC of Assembly 3	49
XVII.	Reactivity Effects of Flooding Void Tubes in Large ITCs of Assemblies 4a and 4b	50
XVIII.	Description of Activation Foils and Wire	52
XIX.	Midplane Activation Ratios	59
XX.	Measurement of Flux Levels near Improper Loading	78
XXI.	Loadings in AARR Critical Facility	79
XXII.	Foil Materials Used in Cadmium-ratio Measurements	80

LIST OF TABLES

<u>No.</u>	<u>Title</u>	<u>Page</u>
XXIII.	Cadmium Ratios in Fuel Region	81
XXIV.	Reactor Instrument Responses to $\sim 1.5\text{-Ci } ^{124}\text{Sb}$ Source, for Various Reactor Configurations	87
XXV.	Reactor Instrument Response as $\sim 1.5\text{-Ci } ^{124}\text{Sb}$ Source Was Raised from Midplane.	87
XXVI.	Instrument Response vs Radial Position of Source	88
XXVII.	Shadowing Data for Control Blades of Assembly 4b.	115
XXVIII.	Standard Control-blade Worths, Using Aluminum Followers	116
XXIX.	Comparison of Worths of Thin and Standard Blades	118
XXX.	Loss of Reactivity-control Worth by Use of Stainless Steel Control-blade Followers, Replacing Aluminum.	122
XXXI.	Descriptions of Special Control-blade Plates.	125
XXXII.	Total Worths of Special Control Blades	127
XXXIII.	Adjusted Partial Worths of Control Blades	128
XXXIV.	Comparison of Reactivity Worths of Small Samples in Fuel Regions	131
XXXV.	Delayed-neutron Fractions Used in Reactivity- period Determinations.	134
XXXVI.	Comparison of Measured Temperature Coefficients of Assemblies 2a, 3, 4a, and 5	139
XXXVII.	Average Void Worths	141
XXXVIII.	Distributions of Radial Void Worths.	143
XXXIX.	Summary of Measurements of Prompt-neutron Lifetimes in AARR Critical Facility	146
XL.	Worth of Added Boron Strips	154

ARGONNE ADVANCED RESEARCH REACTOR CRITICAL EXPERIMENTS

by

K. E. Plumlee, J. W. Daughtry,
T. W. Johnson, W. R. Robinson,
R. A. Schultz, and G. S. Stanford

ABSTRACT

Critical experiments were performed to assist in the design of a high-performance, stainless steel-clad UO_2 - H_2O core, containing about 60 kg of highly enriched uranium, for the Argonne Advanced Research Reactor. Measurements reported include neutron flux and power distributions, critical loadings, flux levels in irradiation facilities and beam tubes, control-blade calibrations, worths of voids and of various neutron-absorbing materials, and temperature coefficients. Pertinent data on neutron spectrum and temperature, prompt-neutron lifetime, and the distribution of gamma radiation heating (which was measured by thermoluminescent dosimetry) are also given; however, some of these techniques and detailed results are to be reported separately.

Measurements made in the range of zero to 300 W in power level were in good agreement with calculations of flux and power ratios for the configurations assembled. Thus these data extrapolated to 10^{16} peak thermal flux at a reactor power of ~ 240 MW. However, the flux per unit power was estimated to be about 15% lower in the design system, which differed slightly from the critical assembly.

I. SUMMARY

Critical experiments were performed with a stainless steel-clad, highly enriched UO_2 (H_2O -moderated) core, as part of the design of the Argonne Advanced Research Reactor (AARR). The results are in excellent agreement with the calculated peak thermal-neutron flux of 4.2×10^7 n/cm²/sec in the internal thermal column (ITC) per watt of power in the fuel region fissions. This ratio corresponded to 10^{16} thermal-neutron flux in the ITC at ~ 240 MW operating power. The ratio varied slightly with changes in control-blade configurations and in fuel-loading density, and was estimated to be about 15% lower for the design core, which differed slightly from the critical assembly.

Flux levels at the tips of horizontal beam tubes inside the beryllium reflector were about a third as high as in the ITC peak and varied with control-rod positions and other factors. Investigation of the effect of positioning hydrogenous material in the tips of the beam tube produced significantly increased yields. As much as 15-20% improvement in yield was obtained using simple geometry. Further improvement might be found using more complicated arrangements.

The thermal-neutron temperature in the large ITC was measured to be $\sim 30^{\circ}\text{C}$ above the moderator temperature. This result was very close to the temperature inferred from the thermal-flux distribution obtained by THERMOS computations.

Reactivity gains as great as $1\frac{1}{2}\%$ in a small ITC and 3% in a large ITC were measured during experiments with massive voids. These measurements were needed in designing the ITC facility, to avoid risk of a damaging excursion resulting from loss of ITC coolant, air entrainment, or other operational difficulty.

The reactivity-temperature coefficients of these assemblies had the same shape and magnitude estimated for the combined expansion coefficient of the core structure and the coolant water.

Europium control blades were significantly more effective than hafnium blades in these cores. However, the reactivity taken by the stainless steel followers used with europium control blades was enough, in the peripheral location, that hafnium blades with aluminum followers were as effective as europium blades with stainless steel followers. In the hardened neutron spectrum of the fuel region, the advantage of aluminum blade followers was much less than near the radial reflector.

II. INTRODUCTION

Critical experiments have been performed with a stainless steel reactor core containing various loadings of highly enriched uranium, in support of the design effort for the Argonne Advanced Research Reactor (AARR). The core design is for high specific power, and it requires a fuel-loading density greater than that previously used in light-water-moderated research reactors. Without heavy fuel loading, the core life-time would be severely limited by the loss of reactivity accompanying fuel burnup, since the core was intended to operate at an average of $1\frac{1}{2}$ to 4 MW per liter of fuel-region volume. The design loading density was so great that the neutron-energy spectrum of the fuel zone included a strong epithermal component. Physics characteristics are not as well known for epithermal U-H₂O systems as for thermal reactors.

The critical experiments served several purposes. Various characteristics of the design were confirmed, assuring that calculated reactivities, power distributions, and irradiation yields should indeed be achievable. Accurate duplication of core geometry, fuel loading, and irradiation facilities was necessary for these measurements. Another purpose was to survey ranges of geometry and loading, thus examining advantages and disadvantages of variations being considered by the designers. In addition, there were measurements involving complicated geometry, which could not be adequately approximated by computation. There were measurements with two sizes of ITCs, various reactivity control materials, a graded or power-flattened fuel loading, a modified beryllium reflector, beam tubes, and many other components, all of which are described along with the experiments involved.

The AARR design was changed late in 1966 to use a lightly loaded aluminum core of the High Flux Isotope Reactor (HFIR) type. Critical experiments for the stainless steel core design were terminated.

Three major interests have governed the preparation of this report. First, much of the information presented was considered necessary for AARR design, safety analysis, and operating limits. This interest particularly involves the ITC and the beam-tube experiments. Second, any future evaluation of such a stainless steel core for use in a research reactor will require a reasonably detailed account of the experiments performed to date. Finally, this set of experiments supplements earlier work at Argonne National Laboratory involving other core designs.¹⁻⁴ Thus, information is now available for a range of fuel-loading density up to 1 kg of highly enriched uranium per liter of fuel zone, for two sizes of ITCs and for a number of compositions of materials in the ITC, the fuel zone, and the radial reflector.

III. DESCRIPTION OF CORE ASSEMBLIES

Fuel loadings were determined by the availability of fuel, for the most part. The first loading was with slightly more than the minimum amount of fuel necessary to achieve criticality without deviating from the nominal dimensions and the metal-to-water ratio specified for AARR. As indicated in Table I, there were five basic core loadings of which four were as uniformly loaded as feasible. The final loading was a mockup of a power-flattened physics reference design⁵ in which the fuel-loading density was graded to compensate for neutron-flux gradients near the inner and outer boundaries of the fuel zone. Deviations from the five basic loadings are described as part of the experiments involved. These deviations ranged from installation of fully loaded fuel subassemblies characteristic of Assembly 4, into the first core as a test of the predicted reactivity for core 4, to such minor changes as reversing the sequence of a few fuel foils in a graded zone to permit measurements of the flux and power distribution associated with hypothetical loading errors.

TABLE I. Basic Core Loadings

Assembly No.	Ratio by Pieces, Fuel/B-SS	²³⁵ U Loading, kg	Boron Loading, g	Measured Reactivity, %
1	315/none	16.07	0	0.4 ^a
2a	615/420	31.40	220	3.6 ^a
2b	615/420	31.40	220	4.8 ^b
3	810/810	41.37	425	2.7
4a	1215/1620	61.49	850	2.2 ^c
4b	1173/1347	59.37	707	3.5 ^c
5	(1132 eff)/1089	57.17	572	4.3 ^d

^aReflector for Assemblies 1 and 2a was 10% Plexiglas and 90% beryllium by volume.

Plexiglas and beryllium were in alternating layers 1.12 and 10.2 cm thick, respectively (see Fig. 2), except for a 5.1-cm top layer of beryllium.

^bPlexiglas was effectively removed from the reflector in Assembly 2b and subsequent loadings. The layers of Plexiglas below the source tube were relocated to be the base for the beryllium, thus supporting the source tube at the original level. The upper layers of Plexiglas were removed, and a 2.5-cm-thick layer of beryllium was added. The bottom beryllium layer was lifted by 2.24 cm and the beryllium stack was 48.3 cm in height after the change, compared to the initial 45.7 cm of beryllium.

^cReactivities reported for Assembly 4 were with beryllium-filled aluminum beam tubes installed. About 0.3% loss of reactivity was attributed to the tube walls and the necessarily incomplete filling of beryllium.

^dReactivity reported for Assembly 5 was with a through beam tube located about 5.1 cm from the safety blade, resulting in about 0.2% loss of reactivity.

The fuel region is hexagonal in shape. Its inner boundary is formed by the 0.16-cm-thick by 6-cm-wide sides of the small ITC liner or the stepped large ITC liner. The outer fuel boundary is the 0.64-cm-thick by 25-cm-wide slots for the six safety blades as shown in Figs. 1 and 2. The active fuel height is 45.7 cm. There are 1215 fuel positions having exchangeable contents. Normally the metal-to-water ratio is unity, with

① DRY THIMBLES FOR FLUX DETECTORS
(ROMAN NUMERAL INDICATES
CHANNEL NUMBER)

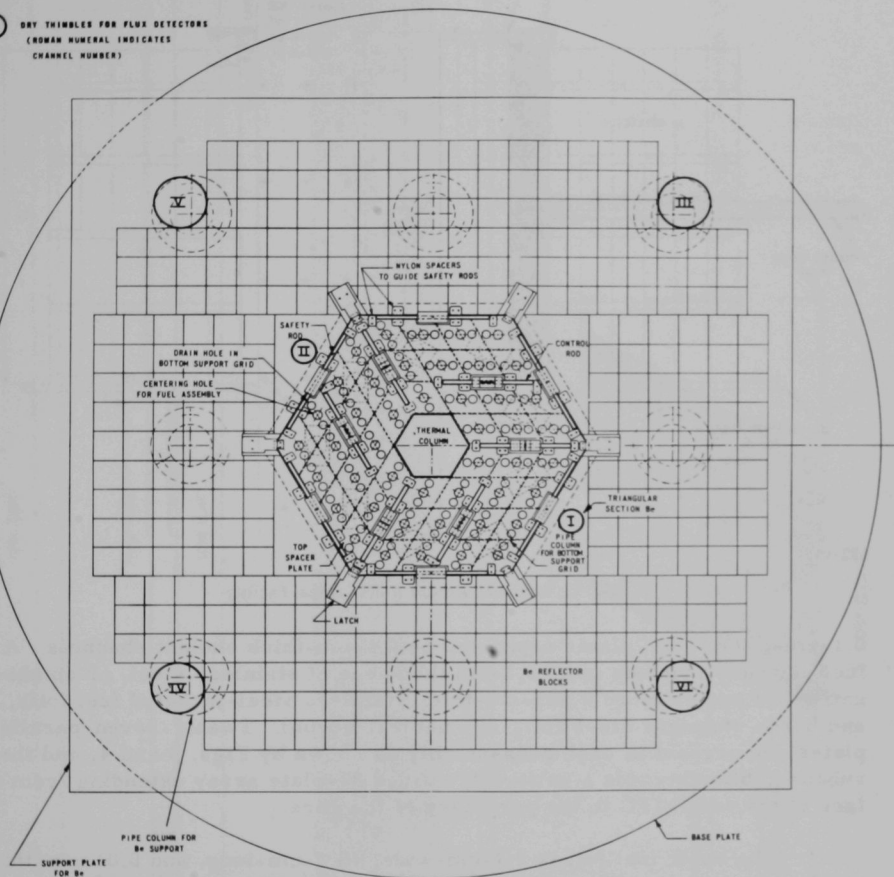
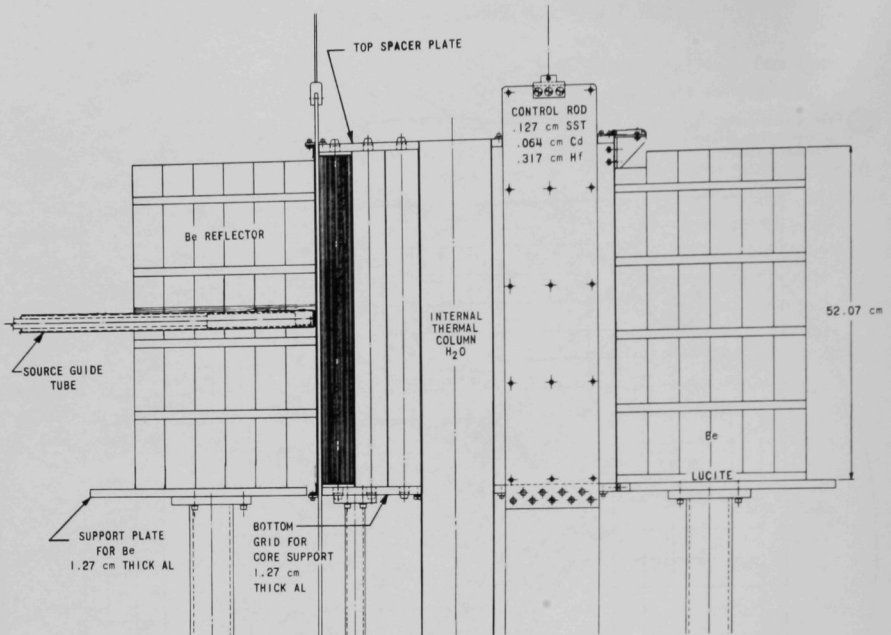


Fig. 1. Plan View of AARR Critical Facility



112-9031

Fig. 2. Sectional View of AARR Critical Facility

0.1-cm-thick metal plates separated by 0.1-cm-thick coolant channels. A fuel plate may include up to 0.1-cm thickness of stainless steel, or combinations of one or more 0.025-cm-thick stainless steel-jacketed fuel foils, and boron stainless steel foils (1% natural boron). Twenty-seven parallel plates are present in each subassembly as shown by Figs. 3 and 4, and three subassemblies provide a uniformly spaced 81-plate array extending from a face of the small ITC to the periphery of the core.

The basic fuel foil is 5.7-cm-wide, 45.7-cm-long, and 0.01-cm-thick highly enriched uranium metal weighing about 54.32 ± 1.0 g (rms deviation). Thinner pieces were obtained for graduated or power-flattened loadings. Table II lists the various fuel categories.

Each fuel foil has an envelope of 0.007-cm-thick (or thicker) stainless steel and the overall thickness was approximately 0.025 cm for each type of foil. One edge of each envelope was formed by folding, and the other three were sealed by electron-beam welding under about 10^{-5} atm vacuum. Most welding failures were evident within a few days; however, three fuel foils failed in the core with ballooning of the jackets; in one instance, this impeded the operation of a control blade. The gas causing the expansion was

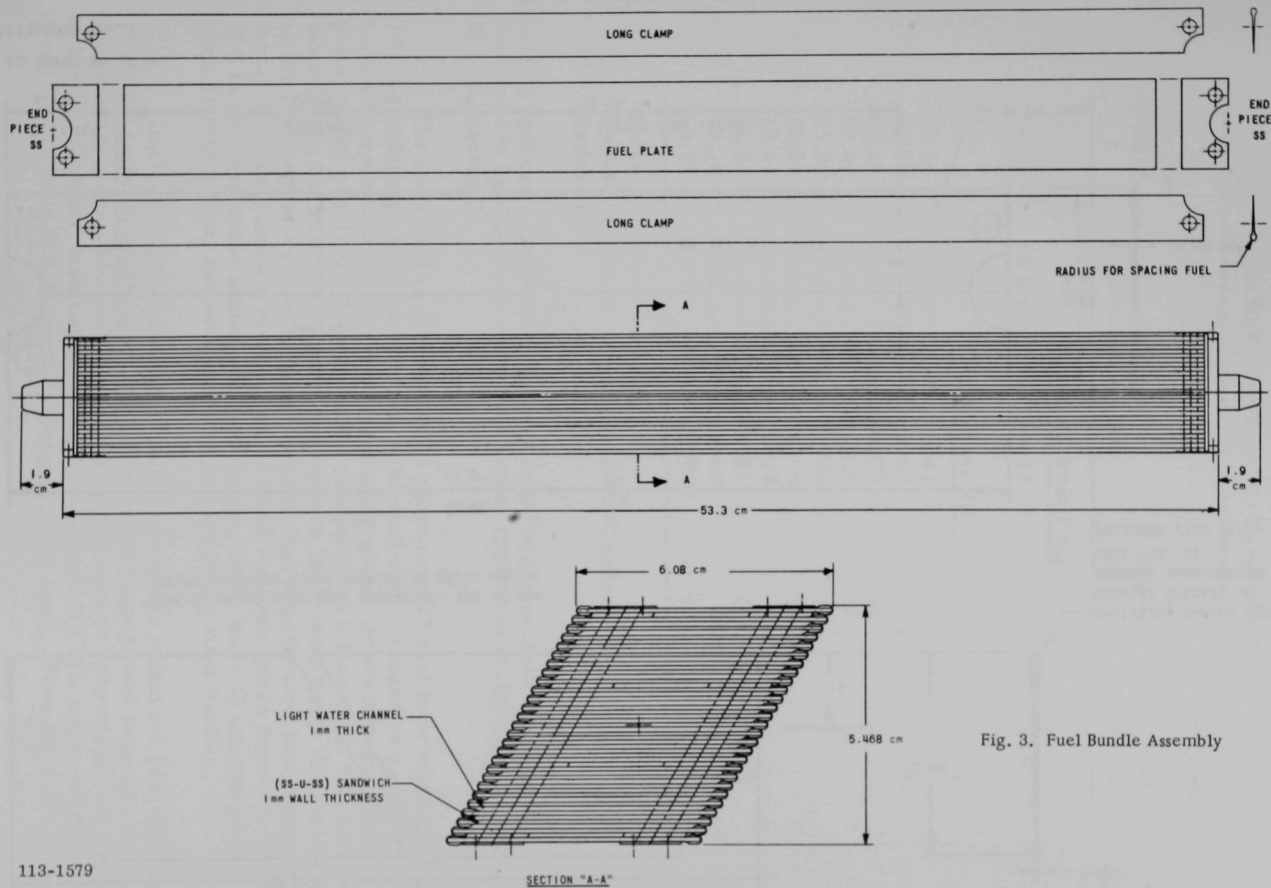
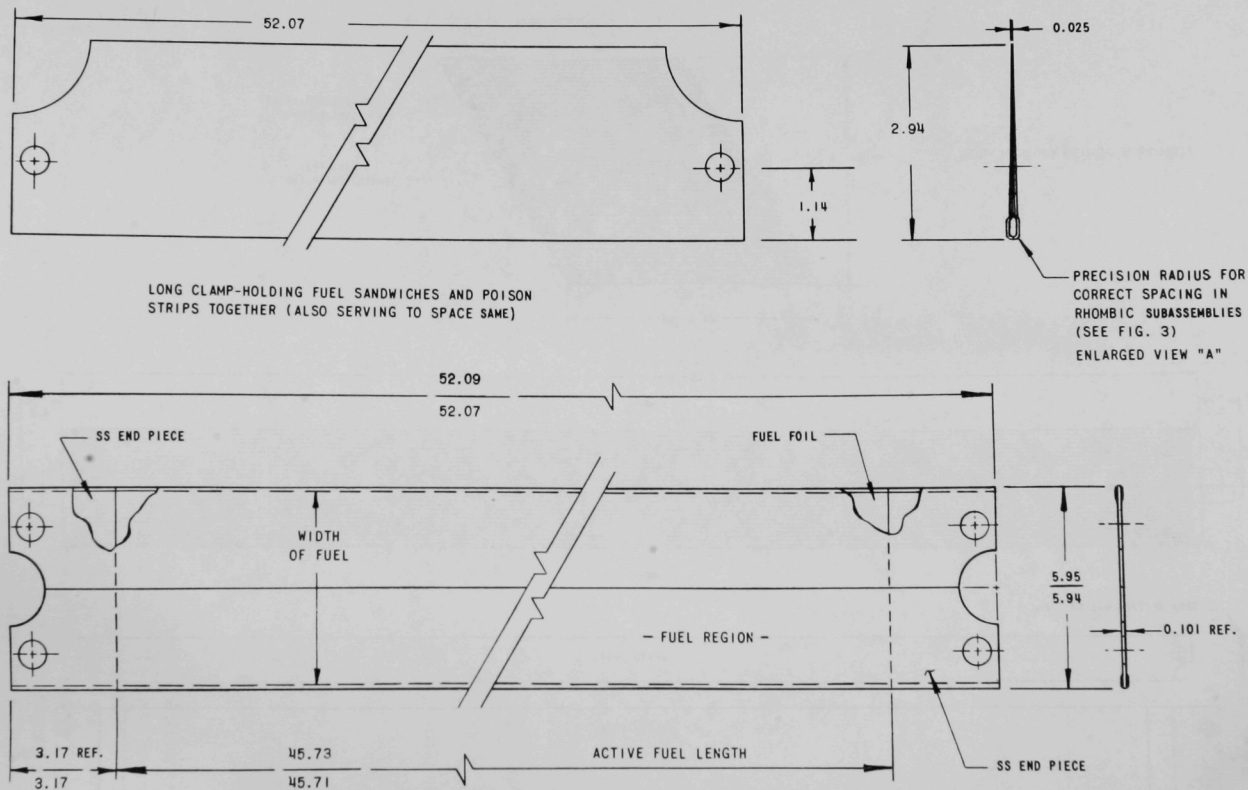


Fig. 3. Fuel Bundle Assembly



ALL DIMENSIONS IN cm

113-1570 Rev. 1

Fig. 4. Fuel Plate Assembly

TABLE II. Fuel-foil Description

Uranium Weight, g	Nominal Dimensions, in.	Number Available	Nominal Number in Fuel Assembly
<u>Standard Fuel Foil</u>			
54.32	18.0 x 2.234 x 0.0044	1259	27 ^a
<u>Thin Fuel Foil^b</u>			
51.14	18.0 x 2.234 x 0.0041	9	
47.54	18.0 x 2.234 x 0.0039	51	
40.68	18.0 x 2.234 x 0.0033	35	
29.65	18.0 x 2.234 x 0.0025	36	
25.23	18.0 x 2.234 x 0.0020	15	
20.50	18.0 x 2.234 x 0.0016	36	
16.41	18.0 x 2.234 x 0.0012	9	
11.32	18.0 x 2.234 x 0.0009	15	
9.16	18.0 x 2.234 x 0.0007	9	
6.9 ^c	18.0 x 2.234 x 0.00055	15	

^aExcept adjoining large ITC.

^bThin foils usually replaced standard foils.

^cEstimated.

mostly hydrogen. No water leak was found in the jackets of the three failed foils, and it has not been resolved whether there was in-leakage resulting in U-H₂O reaction.

The first loading (Assembly 1) contained 315 fuel foils totaling about 17.2 kg of highly enriched uranium. The fuel was arranged in a regular pattern with a nominal pattern of three dummy plates (of stainless steel) to each plate loaded with fuel. To maintain a consistent ITC boundary, the six positions facing the ITC were always loaded with fuel. Similarly, the perimeter of the fuel region was made up of loaded rather than dummy fuel plates insofar as feasible. Since a typical row of three subassemblies from the small ITC to the perimeter contained 81 positions, there were 60 dummy plates to each 21 fuel plates, rather than three to one, in the first loading.

Similarly, the second, third, and 4a loadings contained 615, 810, and 1215 fuel foils, respectively. During loading changes, fuel foils and other components were added or removed from the core to keep metal and water volumes constant. Natural boron was contained by 1.01% boron-stainless steel (B-SS) foils 0.025 cm thick weighing 52 g each. Thus the atom ratio

of $^{235}\text{U}/^{10}\text{B}$ was roughly 22 times the ratio of pieces of fuel/B-SS. The cores are sometimes referred to by the number of fuel foils/B-SS foils, i.e., 315/none, 615/420, 810/810, 1215/1620, 1173/1347, and effectively 1132/1089. At other times, the atom ratio was given.

The 4b loading was with an enlarged ITC, in comparison to 4a, and seven fuel positions were removed from each of six fuel subassemblies facing the ITC in making the room for the large ITC. The 1173/1566 loading resulting from this change was subcritical. The B-SS content was further reduced (to 1347 foils) to compensate for the loss of reactivity because of the enlarged ITC.

With the nominal foil thicknesses stated as fractions of the standard 0.011-cm (0.004-in.) thickness, the graded fuel region of Assembly 5 was loaded as follows: Starting next to the ITC in each of the six adjacent (altered) subassemblies: 0.22, 0.28, 0.37, 0.47, 0.60, 0.75, 0.91, and 1.0. At the periphery of the fuel region, only three instead of seven positions involved thinner than standard foils. Starting with the outermost foil, the fuel positions were loaded 0.42, 0.57, 0.78, and 1.0. Typically, there were 64 standard fuel foils between regions of reduced foil thickness. Some of the subassemblies could not be loaded to obtain graded fuel boundaries. Only those fuel subassemblies that were oriented with fuel plates parallel to the boundary of the fuel region could be graded.

The volumes of various regions were as follows: Small (5.9-cm equivalent radius) ITC, 4.8 liters; large (7.2 cm) ITC, 7.3 liters; fuel region and ITC combined, 77 liters including six interior control-blade channels at 0.55 liter each. The six peripheral safety-blade channels amount to 0.76 liter each.

IV. INTERNAL THERMAL COLUMN EXPERIMENTS

A. Measurement of Flux-to-Power Ratios

1. Purpose

A figure of merit for the maximum neutron irradiation level in the AARR ITC is the ratio of peak flux to reactor power, because the power level will be limited. This ratio was measured in the Critical Experiment to verify the calculated results on which the design of AARR was based. Absolute measurements were made of the ITC flux and of the fission rate in the fuel region of Assemblies 3, 4a, 4b, and 5. These assemblies ranged from two-thirds to fully loaded, and included two sizes of ITCs shown in Figs. 5 and 6, as well as uniformly loaded and graded, or power-flattened, fuel zones.

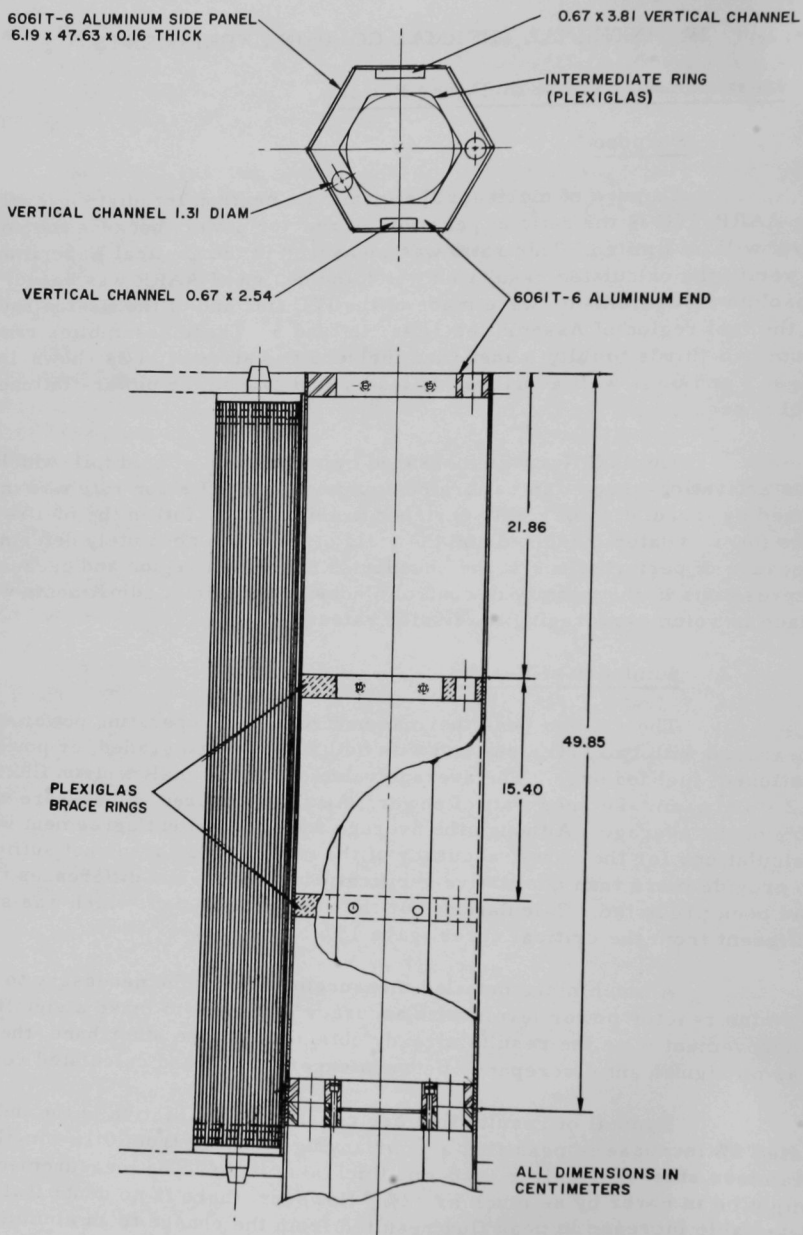
The ITC flux was measured by irradiation of gold foil, which was activation-counted in calibrated equipment. The fission rate was measured by irradiation of highly enriched uranium metal foil in the fuel region. The foil was later dissolved and the yield of ^{99}Mo was absolutely determined. Because of perturbations at the boundaries of the fuel region and because of depressions in the vicinity of control blades, a number of adjustments were made in volume-averaging the fission rates.

2. Summary of Results

The ratio of peak thermal-neutron flux to operating power was measured with two ITC sizes and with both uniform and graded, or power-flattened, fuel loadings. The average value of the thermal-neutron flux was 4.2×10^7 n/cm²-sec per watt of power. All the measured values were within 15% of the average. Although the average was in excellent agreement with calculations for the cores, accuracy of the measurements was not sufficient to provide more than qualitative verification of trends and differences that had been predicted. Calculations for the reference design, which was slightly different from the critical cores, gave 15% lower values.⁶

A much more detailed measurement would be necessary to determine reactor power levels with accuracy sufficient to make a significant improvement over the results already obtained. On the other hand, there was no significant discrepancy between experimental and calculated results.

Typical of results that are considered qualitative is the indicated 5% increase in peak flux accompanying a change from 0.16-cm-thick stainless steel ITC wall to 0.16-cm-thick aluminum. The measurement might be in error by as much as $\pm 2\%$. However, there is no doubt that a detectable increase in peak flux resulted from the change to an aluminum ITC wall.



112-8644 Rev. 1

Fig. 5. Small ITC

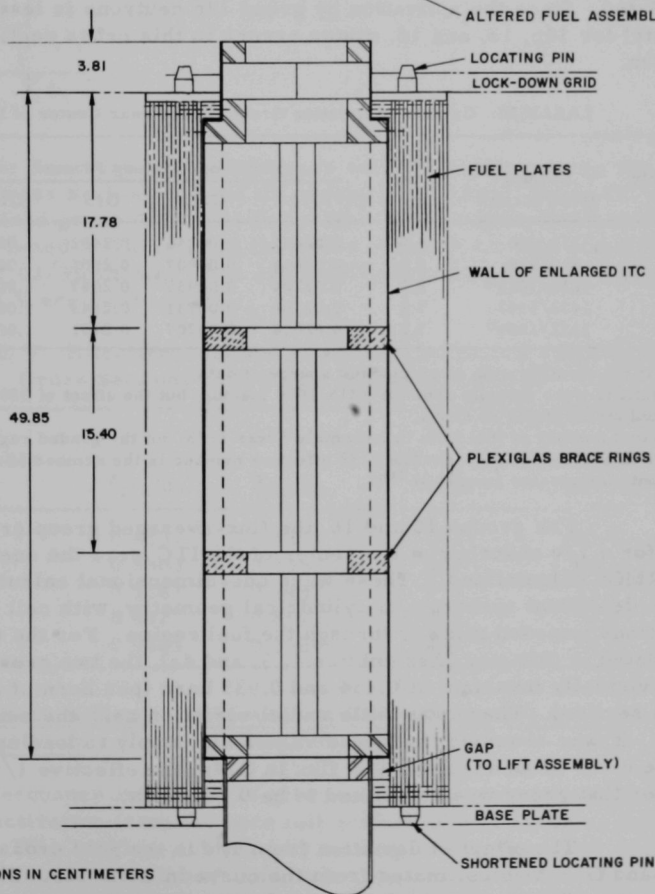
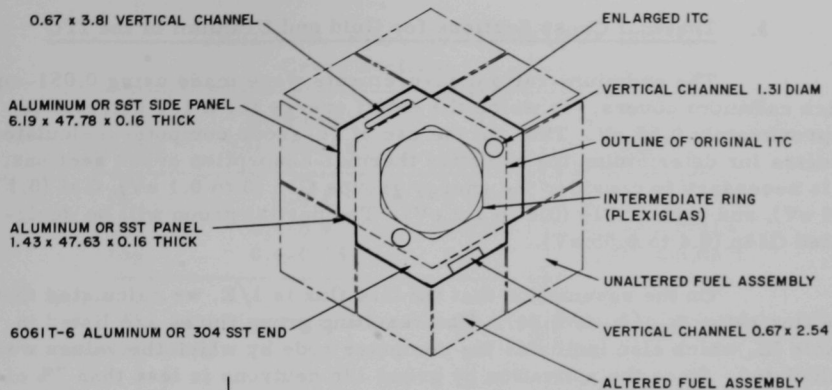


Fig. 6. Large ITC

3. Thermal Cross Sections for Gold and Uranium in the ITC

The cadmium-ratio measurements were made using 0.051-cm-thick cadmium covers, for which the cutoff energy for a $1/v$ detector is approximately 0.55 eV. Thus, in the use of 16-group computer-calculated spectra for determining the effective thermal-absorption cross sections, it is necessary to consider the energy groups G16 (0 to 0.1 eV), G15 (0.1 to 0.4 eV), and part of G14 (0.4 to 1.0 eV). The partial group will be designated G14p (0.4 to 0.55 eV).

On the assumption that the G14 flux is $1/E$, we calculated that the flux ratio Φ_{14p}/Φ_{14} is 0.347. The resulting group fluxes are listed in Table III, which also indicates the computer code by which the values were calculated. Since the activation by group 14p neutrons is less than 2% of the total for 14p, 15, and 16, minor errors in this cross section are of no concern.

TABLE III. Calculated Relative Group Fluxes near Center of ITC

Assembly No.	Loading (fuel/boron)	ITC Radius, cm	Normalized Group Fluxes ^a				Computer Program
			G14	G14p	G15	G16	
1	315/000	5.9	0.02437	0.00846	0.2402	1.0000	REX
3	810/810	5.9	0.02614	0.00907	0.2501	1.0000	REX
4a ^a	1215/1620 ^b	5.9	0.02704	0.00939	0.2547	1.0000	REX
4b	1173/1347	7.2	0.02106	0.00731	0.2143	1.0000	MACH-1
5	1132/1089 ^c	7.2	0.02038	0.00707	0.2101	1.0000	MACH-1

^aSee text for identification of groups and source of data.

^bCalculations were actually done for 1215/2000 loading, but the effect of 380 extra boron-poisoned strips would be small.

^cThe actual number of fuel foils in Assembly 5 was 1173, but the graded regions contained thinner than standard pieces. The 1132 effective number is the number of standard foils that contain the same amount of ²³⁵U.

For groups 15 and 16, the flux-averaged group cross sections used for a $1/v$ absorber at the center of the ITC were the ones provided by THERMOS calculations.⁶ These were one-dimensional calculations of the space-dependent spectrum in cylindrical geometry, with cell boundary conditions imposed midway through the fuel region. For the three loadings calculated in this way (Assemblies 1, 3, and 4a), the two cross sections were virtually invariant at 0.434 and 0.935 barn (per barn of 2200-m/sec cross section). There was little radial variation near the center of the ITCs. It was assumed that these values also apply to loadings 4b and 5. On the basis of an assumed $1/E$ flux in G14p, the effective $1/v$ cross section for that group was calculated to be 0.236 barn.

The effect of deviation from $1/v$ in the gold cross section, for G14p and G15, was estimated from the curve in BNL-325. The corrections used were $47 \pm 3\%$ and $18 \pm 3\%$. Table IV lists the group cross sections used.

TABLE IV. Effective Thermal Group
Cross Sections for ITC

Flux Group	Boundary Energies, eV	$\bar{\sigma}_{1/v}/\sigma_0$	$\bar{\sigma}_{Au}/\sigma_0$
16	0-0.1	0.9347	0.9347
15	0.1-0.4	0.4343	0.512 ± 0.013
14p	0.4-0.55	0.236	0.347 ± 0.007

The effective thermal-neutron-absorption cross sections, σ_{eff} , are calculated using

$$\frac{\sigma_{eff}}{\sigma_0} = \frac{\sum_i \sigma_i \Phi_i}{\sum_i \Phi_i}, \quad (1)$$

where σ_i is the flux-averaged group cross section (relative to σ_0 , the 2200-m/sec cross section) for the i th energy group, from Table IV; and Φ_i is the normalized group flux from Table III. Table V gives the results. The uncertainties listed in Table IV in the cross sections for G15 and G14p lead to an error of $<1/3\%$ in σ_{eff} . It is arbitrarily assumed that the cross sections in Table V are good to $\pm 2\%$.

TABLE V. Effective Gold and Uranium Thermal-absorption
Cross Sections in ITCs for Various Loadings

Assembly No.	$\bar{\sigma}_{1/v}/\sigma_0$	$\bar{\sigma}_{Au}/\sigma_0$	$\bar{\sigma}_{25}$ (fission), barns	$\bar{\sigma}_{Au}$, barns
1	0.8337	0.8494	481	83.9
3	0.8303	0.8466	479	83.6
4a	0.8287	0.8452	478	83.5
4b	0.8427	0.8572	486	84.7
5	0.8443	0.8584	487	84.8

4. Effect of Errors in Measuring Cadmium Ratios and in Estimating Cadmium Cutoff Energy

Resonance activation of gold makes it necessary to subtract the epicadmium activation from the bare foil activation in measuring thermal-neutron flux. This could be achieved by making an equal number of absolute activity determinations with bare and cadmium-covered foils. However, it is more convenient to limit the absolute determinations to bare foils. Use of

the cadmium ratio (CdR) obtained from relative measurements of bare and cadmium-covered gold foils permits use of the following equations in estimating the subcadmium activity A_s from the absolutely measured bare activity A_b :

$$A_s = A_b \frac{\text{CdR} - 1}{\text{CdR}} = A_b \left(1 - \frac{1}{\text{CdR}} \right); \quad (2)$$

$$\frac{dA_s}{A_s} = \frac{d(\text{CdR})}{\text{CdR}} \cdot \frac{1}{\text{CdR} - 1}. \quad (3)$$

As shown by the derivative of A_s , Eq. 3 should not introduce significant error because of error in measuring CdR. The CdRs for the small and large ITCs were 7.42 and 9.11, respectively. Thus an error in CdR measurement would cause only $\sim 1/6.4$ or $\sim 1/8.1$ as large a fractional error in A_s . This permits several absolute determinations for averaging of bare-foil activities rather than dividing the absolute measurements between bare and cadmium-covered foils.

Any error in the estimated cutoff energy of the cadmium-covered foils affects the average cross section estimated for group 14p. Using integral notation, we can show the average cross section of group 14p to be a straightforward function of the cutoff energy, as follows:

$$\begin{aligned} \bar{\sigma}_{14p} &= \frac{\int_{0.4}^{E_{Cd}} \sigma(E) \Phi(E) dE}{\int_{0.4}^{E_{Cd}} \Phi(E) dE} = \frac{X(E_{Cd})}{Y(E_{Cd})}, \\ \frac{d\bar{\sigma}_{14p}}{dE_{Cd}} &= \frac{1}{Y} \frac{dX}{dE_{Cd}} - \frac{X}{Y^2} \frac{dY}{dE_{Cd}} = \frac{1}{Y} \left[\frac{dX}{dE_{Cd}} - \frac{X}{Y} \frac{dY}{dE_{Cd}} \right] \\ &= \frac{\Phi(E_{Cd})}{\int_{0.4}^{E_{Cd}} \Phi(E) dE} \left[\sigma(E_{Cd}) - \bar{\sigma}_{14p} \right]. \end{aligned} \quad (4)$$

Assuming that $\Phi(E) = \Phi_0/E$, we get

$$\frac{d\bar{\sigma}_{14p}/\bar{\sigma}_{14p}}{dE_{Cd}/E_{Cd}} = \frac{\sigma_{E_{Cd}} - \bar{\sigma}_{14p}}{\bar{\sigma}_{14p} \ln(E_{Cd}/0.4)} \approx -0.7, \quad (5)$$

where $\sigma_{E_{Cd}}$ is taken to be 27 b at 0.55 eV, and $\bar{\sigma}_{14p}/98.86 = 0.347$ (from Table IV).

Thus, under the conditions of this experiment, a fractional change of about 0.1 in E_{Cd} changes $\bar{\sigma}_{14p}$ by about 7%. Such an error is negligible because the calculated reaction rate for group 14p is less than 2% of the total for groups 14p, 15, and 16. The 0.1 error in E_{Cd} would affect the calculated reaction rate by $\sim 0.2\%$, which is less than the measuring error for absolute activity of gold.

It can also be shown that in calculating A_s , the effects of transmission of subcadmium neutrons by the cadmium can be neglected, along with the epicadmium absorption by the cadmium. Therefore, for these measurements the cadmium can be considered to be a perfect filter with a sharp cutoff at 0.55 eV, with negligible error in the absolute flux measurement.

Similar measurements were made with highly enriched uranium foils. Because the cadmium ratios were larger (60 and 90) than with gold (7.4 and 9.1), the errors are smaller than with gold. However, the larger thermal cross sections of the uranium foils required greater corrections for thermal-energy self-shielding and flux perturbations, which are discussed in Section 5 directly below.

5. Foil Self-shielding and Outer Flux Depression

In 1-mil gold, there is a large amount of self-shielding at the 4.9-eV resonance. However, this does not pertain to the present determination of thermal flux, since only the subcadmium component of the bare-foil activation is used for the flux determination.

In the thermal-energy region, the effects of both self-shielding and outer flux depression were corrected using the following equation:⁷

$$G = \frac{A_s}{A_u} = \frac{\bar{\Phi}}{\Phi_u} \frac{[1/2 - E_3(\tau)]/\tau}{1 + [1/2 - E_3(\tau)]g}, \quad (6)$$

where A_u and Φ_u are the unperturbed thermal activation and flux, $\bar{\Phi}$ is the thermal flux averaged over the volume of the foil, τ is the optical thickness ($\Sigma_a t$) of the foil, and $E_3(\tau)$ is the third-order exponential integral. The factor g is a function of the foil diameter, foil thickness, and medium surrounding the foil. The gold and uranium foils used in these experiments were 0.28 cm in diameter. For those foils, in a water medium, g is approximately 1.4.

If we use an effective σ_a of 84 barns for gold, τ for a 1.1-mil foil is 0.0139, leading to $G = 0.946$.

For the enriched (93.2%) uranium foils, the self-shielding and flux-depression factor, G is to be calculated using the total absorption cross section (693 barns at 2200 m/sec), multiplied by the value of σ_{uv}/σ_0 from

Table V. The resulting values of G are 0.824 and 0.694, respectively, for the 1-mil foils used in Assembly 3 and the 2-mil foils used in Assembly 5.

6. Flux Determinations

The unperturbed subcadmium flux Φ_S at the location of the foil is given by

$$\Phi_S = \frac{\rho A_S}{N\sigma_{\text{eff}}G}, \quad (7)$$

where A_S is the subcadmium saturated activation per gram of foil, ρ is the density of the foil material, G is the correction factor for self-shielding and flux depression, N is the number of atoms per cm^3 of foil, and σ_{eff} is the spectrum-averaged subcadmium absorption cross section from Table V. Table VI lists the calculated fluxes for the seven runs that were made.

TABLE VI. Measured ITC Fluxes for Assemblies 3, 4a, 4b, and 5

Assembly No.	Foil	CdR ($\pm 10\%$)	$\frac{\text{CdR} - 1}{\text{CdR}}$ ($\pm 2\%$)	Saturated Activities, $\text{sec}^{-1} \text{g}^{-1}$		σ_{eff} (from Table V), barns	Subcadmium Flux, Φ_S , $\text{n/cm}^2\text{-sec}$ ($\pm 5\%$)
				A_b ($\pm 3\%$) ^b	A_s (Eq. 2) ($\pm 4\%$)		
3	Au	7.42	0.887	2.41×10^8	2.14×10^8	83.6	8.85×10^8
4a	Au	7.42	0.887	15.91×10^8	14.11×10^8	83.5	58.4×10^8
4b, Run 50-151 Run 50-156	Au	9.11	0.890	7.28×10^8	6.48×10^8	84.7	26.4×10^8
	Au	9.11	0.890	38.2×10^8	34.4×10^8	84.7	140.3×10^8
5, Run 53-1	Au	9.11	0.890	27.8×10^8	24.7×10^8	84.8	100.9×10^8
	²³⁵ U	90	0.989 ^a	$27.5 \times 10^{11}\text{C}$	$27.2 \times 10^{11}\text{C}$	487	102.3×10^8
5, Run 54-5	Au	9.11	0.890	38.9×10^8	34.6×10^8	84.8	141.0×10^8
	²³⁵ U	90	0.989 ^a	$45.4 \times 10^{11}\text{C}$	$44.9 \times 10^{11}\text{C}$	487	142.8×10^8
5, Run 54-6	Au	9.11	0.890	27.7×10^8	24.6×10^8	84.8	100.2×10^8
	²³⁵ U	90	0.989 ^a	46.2×10^8	$45.7 \times 10^{11}\text{C}$	487	105.7×10^8

^a $\pm 0.2\%$.

^b A_b is the saturated specific activation of the bare foil.
C Fissions/g.

In Assembly 5, foils of both uranium (2 mils) and gold were used in the ITC, on three occasions. As can be seen from Table VI, there is good agreement between the gold and uranium results. The first measurement in Assembly 5 (Run No. 53-1) was combined with an experiment for which there were several anomalously heavy fuel plates in the graded region near the ITC. As in the other cases, the calculation was performed for the core as it was when the run was made. In Run No. 54-6, the measurement was repeated with the regular graded loading. The results agreed within experimental precision.

7. Absolute Determination of Total Core Power

a. General Considerations. The reactor power was determined by absolute fission counting of uranium foils or fuel samples. Using

the known reactor running time, we could then determine the fission rate during the run for the sample or samples analyzed. Although there are limits on the accuracy of estimating core power from such numbers, it is possible to get numbers that are meaningful within stated limits. Fairly elaborate flux and power mapping would be necessary for substantially improved accuracy.

The principal uncertainty lies in the process of numerical integration over the core volume. The most clear-cut case occurs when all blades are withdrawn and criticality is controlled by water level. In this case, the radial and vertical fission-product traverses taken under the same conditions can be used directly to determine the actual power at which the reactor was running. (However, relating such results to the normal fully reflected operation of the reactor becomes somewhat tenuous.) The measurements in Assembly 4b, and one in Assembly 5, were done in that manner. In Assembly 3, the measurement was made with a full top reflector, and with criticality controlled by a cluster of three blades. The power depression in the vicinity of the control blades was not known in detail, and the uncertainty limits are larger. The same sort of problem arises for the measurement made in Assembly 4a, where criticality was controlled by means of two partially inserted control blades on opposite sides of the core.

None of the above-mentioned operating conditions corresponds to the anticipated operating configuration in AARR, which is with peripheral blades banked somewhat below the top of the fuel, and internal blades banked at the level required for criticality (which changes during the lifetime of a core). Consequently, measurements were made in the graded loading (Assembly 5) with both water-level critical and banked-blade critical configurations. For the latter, the peripheral blades were banked with their tips 2.5 cm below the top of the active fuel, and criticality was obtained with the tips of the in-core control blades approximately 5 cm below the midplane of the core.

The ITC fluxes reported here are normalized to 1 W of core power, for the actual operating configurations of the critical assembly.

b. Numerical Integration. The fission-rate determinations were made near the midplane of the core and near the center of a 27-plate subassembly. The fission foil was retained in a 0.1-cm-thick aluminum spear, which was inserted in the selected water channel. Experiments involving analysis of fuel-plate samples were done in Assembly 4b to investigate the relationship of these water-channel measurements to the actual fission rate in the fuel.

The following five steps were performed in estimating the core power:

(1) Since the fission rate is not constant across the width of a fuel plate, a factor consisting of the ratio of the average fission rate across the fuel plate to the measured fission rate at the center of the plate was used. On the basis of the above-mentioned fuel-sampling experiments in Assembly 4b, plus wire-activation measurements,⁸ the value 1.03 ± 0.01 has been used.

(2) A multiplying factor is needed to convert the fission rate observed for a foil in an aluminum spear between the fuel plates to the fission rate in the fuel. From the experiments in Assembly 4b, this factor was measured at 1.16 ± 0.02 . Such a measurement was not made in Assembly 3, but the factor would be expected to be somewhat smaller in that core, since the lighter fuel loading should lead to less shielding of the fission foil by the fuel. Consequently, for Assembly 3 the arbitrary factor 1.12 ± 0.04 was used.

(3) A factor for vertical averaging can be obtained by numerical integration of vertical fission-product traverses in the fuel region, given in Section V.D below. For the blade criticals in Assemblies 3 and 4a, the factor is 0.77 ± 0.04 . For Assembly 4b (water-level critical), the factor was 0.65 ± 0.03 . (This factor is for the entire fuel region, including the part not covered by the water.) The factors for Assembly 3 were obtained similarly.

(4) A factor for radial averaging can be obtained from the radial traverses. However, because of the very steep gradients at both the inner and outer boundaries of the fuel zone, and because of the generally nonhomogeneous nature of the core, the uncertainty in the result (as estimated by varying some of the input quantities) is of the order of $\pm 8\%$. The radial factors used for Assemblies 3, 4a, and 4b were 1.06, 1.18 and 1.11, respectively, each with an assigned error of $\pm 8\%$. For Assembly 5, the fact that the loading was graded made the result less sensitive to the values at the inner and outer boundaries of the core; the error assigned in that case was $\pm 5\%$.

(5) For the runs made with some of the control blades inserted, the reduction in fission rate near the inserted control blades must be taken into account. Data are not available to permit this factor to be much better than a rough estimate, but for Assembly 3, some guidance can be had from Figs. 31 and 32 in Chapter V. The figures indicate that the flux is depressed by a factor of about two, over approximately a fourth of the core volume. Averaged over the core, this reduces the power by $12 \pm 4\%$, leading to a multiplying factor of 0.88 ± 0.04 . For Assembly 4a, two peripheral control blades were approximately four-fifths inserted, inducing a perturbation estimated to be approximately three-fourths as large as for Assembly 3. Thus the blade-perturbation factor used for Assembly 4a was 0.91 ± 0.05 .

In the absence of detailed three-dimensional fission-rate surveys for the banked-blade configuration, the blade-perturbation factor must be estimated for the two runs in Assembly 5. Some relevant information can be taken from Fig. 60 (later in this report), which shows vertical activation traverses made near a half-inserted control blade. The uranium foils for the power measurements were slightly below the level of the tips of the interior blades, and in the middle of an adjacent fuel assembly. Thus it can be inferred that the flux at the foil position was approximately 5% less than the asymptotic value.

Some approximate averaging over the volume of the core on the basis of Fig. 60, leads to an estimated blade-perturbation factor of 0.85 ± 0.05 , including the 5% allowance for the foil position.

c. Results and Discussion. The data are summarized in Table VII, which gives the calculated power for each run, and also the calculated flux per watt of core power.

TABLE VII. Measured Reactor Power and ITC Thermal-neutron Flux per Watt

Assembly No. Run No.	3	4a	4b 50-151	4b 50-166	5 53-1 ^a	5 54-5	5 54-6
Criticality controlled by Reactor running time, sec	Blades 675	Blades 960	Water Level ^b 985	Water Level ^b 1900	Banked Blades ^c 329	Water Level ^d 389	Banked Blades ^c 535
10^{10} fissions/g at test point	$1.24 \pm 6\%$	$7.04 \pm 5\%$	$4.18 \pm 5\%e$	$39.8 \pm 5\%e$	$4.64 \pm 5\%$	$8.29 \pm 5\%$	$7.97 \pm 5\%$
<u>Correction Factors</u>							
(1) Average across fuel plate	$1.03 \pm 1\%$	$1.03 \pm 1\%$	$1.03 \pm 1\%$	$1.03 \pm 1\%$	$1.03 \pm 1\%$	$1.03 \pm 1\%$	$1.03 \pm 1\%$
(2) Rate in fuel/rate in channel	$1.12 \pm 4\%$	$1.16 \pm 2\%$	e	e	$1.16 \pm 2\%$	$1.16 \pm 2\%$	$1.16 \pm 2\%$
(3) Vertical average	$0.77 \pm 5\%$	$0.77 \pm 5\%$	$0.65 \pm 5\%$	$0.65 \pm 5\%$	$0.76 \pm 5\%$	$0.57 \pm 5\%$	$0.76 \pm 5\%$
(4) Radial average	$1.06 \pm 8\%$	$1.18 \pm 8\%$	$1.11 \pm 8\%$	$1.11 \pm 8\%$	$1.04 \pm 5\%$	$1.03 \pm 5\%$	$1.03 \pm 5\%$
(5) Blade perturbation	$0.88 \pm 5\%$	$0.91 \pm 5\%$	f	f	$0.85 \pm 12\%$	f	$0.85 \pm 12\%$
Composite factor:	$0.83 \pm 11\%$	$0.99 \pm 11\%$	$0.74 \pm 9.5\%$	$0.74 \pm 9.5\%$	$0.80 \pm 14\%$	$0.70 \pm 8\%$	$0.80 \pm 14\%$
Reaction rate, averaged over core, 10^7 fis/g-sec	$1.52 \pm 13\%$	$7.24 \pm 12\%$	$3.15 \pm 11\%$	$15.56 \pm 11\%$	$11.31 \pm 15\%$	$14.93 \pm 9\%$	$11.84 \pm 15\%$
Uranium present, kg	44.4	66.0	63.7	63.7	61.6 ^g	61.5	61.5
Core power, watts	$21.8 \pm 13\%$	$154 \pm 12\%$	$64.8 \pm 11\%$	$320 \pm 11\%$	$224 \pm 15\%$	$297 \pm 9\%$	$235 \pm 15\%$
Flux in ITC, 10^8 cm ⁻² sec ⁻¹ (from Table IV)	$8.85 \pm 5\%$	$58.4 \pm 5\%$	$26.4 \pm 5\%$	$140.3 \pm 5\%$	$101.6 \pm 4\%h$	$141.9 \pm 4\%h$	$103.0 \pm 4\%h$
Flux/watt of core power, 10^7 cm ⁻² sec ⁻¹ W ⁻¹	4.2 ± 0.6	3.8 ± 0.5	4.1 ± 0.5	4.4 ± 0.5	4.53 ± 0.70	4.8 ± 0.5	4.39 ± 0.70

^aFor Run 53-1, there were four extra-thick fuel plates in the graded region near the ITC.

^b85% of fuel was flooded.

^cIn-core blades banked with tips ~5 cm below midplane of core; peripheral blades banked with tips ~2.5 cm below top of fuel.

^d77% of fuel was flooded.

^eAnalysis of sample punched from center of fuel plate.

^fRuns were made with water-level control.

^gAverage of gold and uranium results.

Table VII indicates that, considering the rather broad error limits, the peak thermal-neutron flux in the ITC, per watt of core power, is roughly the same for all the runs, which include two ITC sizes, several blade and reflector configurations, and several fuel configurations. All the flux values lie within 15% of the average value, which is 4.2×10^7 cm⁻² sec⁻¹ watt⁻¹. The experimental precision is not sufficient to confirm the slight dependence on loading density that is indicated by theoretical calculations, which predict a 10% reduction in the flux-to-power ratio in going from Assembly 1 to Assembly 4a.⁶

The measurements extrapolate to a peak thermal-neutron flux at 100 MW of approximately $4 \times 10^{15} \text{ n cm}^{-2} \text{ sec}^{-1}$ and at 240 MW of close to $10^{16} \text{ n cm}^{-2} \text{ sec}^{-1}$.

As stated earlier, the design core calculations were less favorable than those for the critical experiment.

B. Measurement of Neutron Temperature and Epithermal Index in ITCs by Cadmium Ratios

Before irradiation of samples in the AARR ITC, preliminary estimates will be needed of reactivity requirements, reaction rates, yields, and cooling problems to be encountered. Conventionally this requires cross sections calculated as functions of neutron temperature (T) and epithermal index (r) characterizing the neutron-energy distribution of the ITC. Both the measurement and the application of those terms encounter some approximation; nevertheless this method provides a systematic basis for irradiation experiments.

Westcott's coefficients⁹ and terminology are used unless indicated otherwise. Other information than Westcott's tables was occasionally necessary. For infinite dilution condition, the flux-averaged cross section of a material is calculated by

$$\bar{\sigma}_a = \sigma_0(\pi T_0/4T)^{1/2}[g(T) + rS(T)], \quad (8)$$

where σ_0 denotes the absorption cross section for 2200-m/sec neutrons, T_0 is the neutron temperature corresponding thereto, T is the effective thermal-neutron temperature, $g(T)$ is the ratio between thermal-neutron absorption by the isotope and that of a $1/v$ material having the same σ_0 , r is the ratio between epithermal and thermal-neutron flux and is often referred to as the epithermal index, and the coefficient $S(T)$ relates resonance absorption to thermal absorption. For a pure $1/v$ cross section, $g(T) = 1$ and $S(T) = 0$. Several materials having resonances well above the cadmium cutoff have $g(T) = 1$ even though $S(T) \neq 0$. Westcott's coefficients used in this report were flux-weighted with a Maxwellian thermal-energy distribution joined at 4.95kT to a $1/E$ epithermal neutron-energy distribution.

The cadmium ratio (CdR) of a material (measured at infinite dilution) is often written according to

$$\text{CdR} = \frac{g(T) + rS(T)}{rS(T) + rP(T)} \quad (9)$$

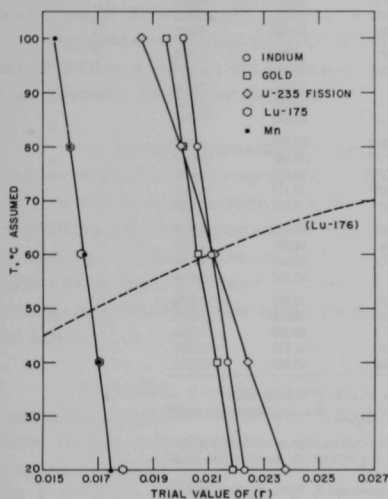
which may be solved instead for the epithermal index r as in

$$r = \frac{g(T)}{\text{CdR}[S(T) + P(T)] - S(T)} \quad (10)$$

If the infinite-dilution CdR is not available, modified versions of Eq. 9 must be used. The adjustment to infinite dilution may be estimated from reports by Jacks¹⁰ or Baumann,¹¹ and modified equations are indicated by Chidley, Turner, and Bigham.¹²

Regardless of the procedure followed, the terms and coefficients must be carefully examined to determine if they are appropriate for the intended use. As a simple example, Westcott apparently uses absorption

resonance integral RI, which is correct for reactivity calculations, in determining $S(T)$. For indium foils, this is 35% greater than the activation resonance integral,^{11,13} which should be used with activation cadmium-ratio measurements.



112-9099 Rev. 1

Fig. 7. Plot of Trial (r) for Determination of Neutron Temperature in Large AARR ITC

Figure 7 gives trial values of r resulting from measured CdRs and assumed temperatures. The information required for these plots is tabulated in Tables VIII and IX. The plot of r versus T for ^{176}Lu cuts sharply across the other plots and indicates a reproducible value of T for which Eq. 9 or 10 is satisfied. The plot for ^{176}Lu CdR would shift by about $\pm 5^\circ\text{C}$ within the range of corrections and adjustments considered to be subject to the discretion of the experimenter.

On the other hand, the assignment of reasonable error limits to the gold,

TABLE VIII. Cadmium Ratios in ITC and Correction to Infinite Dilution

Foil Material	Foil Size, cm		Uncorrected CdR AARR ITC ^a	AHFR ITC ^b	Correction Factor ^c	Infinite-dilution CdR	
	Thickness	Width				AARR ITC ^a	AHFR ITC
12.5% Lu-Al ^{176}Lu	0.040	2.54 (sq)	131.41 (L)	-	-1.0	131.41 (L)	-
			2.52 (L)	-	0.956	2.40 (L)	-
90% Mn-Cu ^{176}Lu	0.0064	0.817 (diam)	44 (S)	-	1.00	44 (S)	-
			50 (L)	-	-	50 (L)	-
80% Mn-Cu	0.0102	0.559 (diam)	-	55 (C-1 & -2)	1.007	-	55
Au	0.0025	1.0 (sq)	7.42 (S)	10.5 (C-1)	0.390	2.89 (S)	4.10
			9.11 (L)	9.4 (C-2)	0.390	3.55 (L)	3.67
17% U-Al	0.0051	0.817 (diam)	60 \pm 12 (S)	-	1.055	63.3 (S)	-
			90 \pm 9 (L)	-	1.055	95.0 (L)	-
	0.0660	0.999 (diam)	-	72 \pm 14 (C-1)	1.082	-	77.9
			-	31 \pm 1 (C-2)	1.082	-	33.5
4% Dy-Al	0.0203	0.559 (diam)	-	312 \pm 80 (C-1)	1.006	-	314
			-	290 \pm 30 (C-2)	1.006	-	292
In	0.0030	0.818 (diam)	8.2 (L)	-	0.464	4.34 (L)	-
	0.0127	0.559 (diam)	-	14.7 \pm 0.6 (C-1)	0.443	-	7.07
			-	13.5 \pm 0.2 (C-2)	0.443	-	6.54

^aS and L distinguish between large and small flux trap.

^bC-1 and C-2 are two different core loadings.¹

^cData from Refs. 10 or 11. This factor includes thermal-flux depression, cadmium thickness, and infinite-dilution corrections. The correction for ^{176}Lu would reduce the measured neutron temperature by about 3°C . However, it was omitted pending a revised value which is nearer unity, per telephone conversation with N. P. Baumann (SRL).

TABLE IX. Use of Activation Cadmium Ratios in Determining Neutron Temperature (Tn) and Epithermal Index (r)

Isotope	Assumed T, °C	g(T)	S(T)	P(T)	Denominator of Eq. 9	Resulting r
¹¹⁵ In	20	1.0192	13.04 ^a	0.482	45.645	0.0223
	40	1.0231	13.47 ^a	0.497	47.147	0.0217
	60	1.0271	13.90 ^a	0.512	48.648	0.0211
	80	1.0310	14.30 ^a	0.528	50.054	0.0206
	100	1.0350	14.71 ^a	0.562	51.570	0.0201
Au	20	1.0053	17.30	0.482	45.826	0.0219
	40	1.0064	17.88	0.497	47.358	0.0213
	60	1.0075	18.44	0.512	48.840	0.0206
	80	1.0086	18.98	0.528	50.273	0.0201
	100	1.0097	19.51	0.562	51.746	0.0195
²³⁵ U Fission	20	0.9759	-0.0502	0.482	41.071	0.0238
	40	0.9711	-0.0410	0.497	43.361	0.0224
	60	0.9665	-0.0324	0.512	45.594	0.0212
	80	0.9662	-0.0244	0.528	47.866	0.0201
	100	0.9581	-0.0169	0.562	51.801	0.0186
¹⁷⁶ Lu	20	1.7011	1.669	-0.169 ^b	183.326	0.0093
	40	1.8373	1.218	-0.174 ^b	138.887	0.0132
	60	1.9769	0.757	-0.170 ^b	93.451	0.0212
	80	2.1175	0.303	-0.185 ^b	49.117	0.0431
	100	2.2576	-0.130	-0.197 ^b	6.874	0.3284
¹⁷⁵ Lu	20	1.00	~39 ^c	0.482	55.757	0.0179
	40	1.00	~41 ^c	0.497	58.593	0.0171
	60	1.00	~42.6 ^c	0.512	60.869	0.0164
	80	1.00	~44 ^c	0.528	62.867	0.0159
Mn	20	1.00	0.666	0.482	56.734	0.0176
	40	1.00	0.689	0.497	58.611	0.0171
	60	1.00	0.710	0.512	60.390	0.0166
	80	1.00	0.731	0.528	62.219	0.0161
	100	1.00	0.752	0.562	64.948	0.0154

^aFor ¹¹⁵In activation, the activation resonance integral was taken from A. E. McArthur and P. J. Persiani, *ANL Reactor Physics Constants Center Newsletter No. 11*, Neutron Resonance Integral and Age Data (Jan 1965).

^bAt cadmium cutoff energy, the ¹⁷⁶Lu cross section appears to be ~0.35 as large as calculated for a 1/ν cross section, using the 2200-m/sec cross section of ¹⁷⁶Lu, and P(T) for 1/ν absorbers was multiplied by this factor.

^cApproximate S(T) values were obtained for ¹⁷⁵Lu from K. H. Beckurts and K. Wirtz, *Neutron Physics* (L. Dresner's translation), Springer-Verlag, New York Inc. (1964).

indium, and ²³⁵U fission measurements results in overlap such that any temperature within the range shown is at least a possibility that might satisfy Eqs. 9 and 10. The manganese and ¹⁷⁵Lu plots are mutually in agreement, but those data are incompatible with data from gold, indium, and ²³⁵U fission. Surprisingly, Westcott's S(T) values based on absorption RI for indium would cause apparently good agreement with the manganese and ¹⁷⁵Lu data rather than with gold and ²³⁵U fission. That discovery led to a literature search for alternative choices of S(T) used by other experimenters. Chidley, Turner and Bigham¹² had used equations, coefficients, and correction factors implying possibly ~18% smaller S(T) values for manganese than shown by Westcott⁹ or an equivalent error in Jacks' curves¹⁰ for correction of manganese CdR to infinite dilution. Use of the terms implicit in Ref. 12, rather than those of Table IX for the manganese S(T)'s, brought the manganese data into reasonable agreement with gold, indium, and ²³⁵U fission. However, the r estimated from gold data would be drastically affected by such a procedure. It was concluded that the Ref. 12 value of $G_T S_0 = 0.534$ was probably the best available value for manganese foils of the size and composition normally used. The Westcott S(T)'s for manganese are larger, but it is not clear whether the S(T) or the correction to infinite dilution should be changed.

Reference 14 recommends a remeasurement of the manganese resonance integral. In addition, a noticeable discrepancy¹³ is found between measured and calculated resonance integrals for manganese (i.e., calculated from resolved resonances), and this clearly suggests that the measured value should be higher. Comparison of the r values given by gold and manganese foils in a large D₂O-filled ITC shows that manganese gives a larger value for r than does gold, which is the opposite of the results for AARR ITC. This suggests again that the difficulty may result from errors in resonance self-shielding corrections. Improvement of cross-section data for manganese would assist in experiments such as neutron-source standardizations by the manganese bath technique as well as measurements of the variety reported herein.

Although a perturbation in the neutron-energy distribution of the fuel region would not be expected to extend as far into the ITC as the axial location where these measurements were made, there appears to be strong self-shielding of the manganese resonance activation by the stainless steel fuel cladding. This is discussed further in Section IV. Self-shielding may have had some minor effect on the manganese data, but the close agreement of manganese with ¹⁷⁵Lu indicated by Fig. 7 suggests an error that is common to both.

Finally, comparison with a summary of pulsed-source time-of-flight measurements¹⁵ of the spectrum in H₂O indicated that the neutron temperature in the AARR ITC was detectably above that expected for a large H₂O region. Table III-5 of Ref. 15 indicated a measured neutron temperature of $26 \pm 15^\circ\text{C}$ in $18^\circ\text{H}_2\text{O}$, or $8 \pm 15^\circ$ from the H₂O temperature. The foil data of this experiment would not indicate lower than 45°C neutron temperature under any likely method of analysis, and the reported value is $50\text{--}60^\circ\text{C}$, compared with an H₂O temperature of about 26°C . (The measurement followed a temperature-coefficient experiment.) Thus this experiment indicated a neutron temperature of $29 \pm 5^\circ\text{C}$ above the moderator temperature. However, the value reported depends almost entirely on the ¹⁷⁶Lu data and could easily be affected by a few degrees ($\pm 5^\circ\text{C}$) within the range of possibilities subject to the discretion of an experimenter.

The data of Tables III, IV, and V are sufficient for calculation of a neutron temperature that should be representative of the best available calculational methods. The value for $\sigma_{1/v}/\sigma_0 = 0.8443$ for Assembly 5, from Table V, can be used to solve for the ITC neutron temperature using a rewritten version of Eq. 10, and noting that $g(T) = 1$ and $S(T) = 0$ for $1/v$ cross sections.

$$\left. \begin{aligned} T_n &= (\pi/4)(\sigma_0/\bar{\sigma}_a)^2 [g(T) + rS(T)]^2 T_0; \\ T_n &= (\pi/4)(\sigma_0/\sigma_a)^2 T_0 = 323.5^\circ\text{K}. \end{aligned} \right\} \quad (11)$$

The calculations were for room-temperature (293.6°K) moderator; therefore the calculated neutron temperature is 30°C above the ITC H₂O temperature, compared with $29 \pm 5^\circ\text{C}$ measured by foil activation. Chidley, Turner and Bigham¹² claimed higher precision than $\pm 5^\circ\text{C}$, using ¹⁷⁶Lu, manganese, and indium foils. The AARR experiments did not include all the necessary measurements of their method; however, their equations and coefficients yield a neutron temperature very close to the calculated value when modified to use the available data, the gold data being an exception.

Errors of ± 5 or $\pm 10^\circ\text{C}$ might affect typical $1/v$ cross-section calculations by 1 or 2%, which should not greatly weaken irradiation predictions for AARR. Nevertheless, the agreement indicated here is not as firm as might be desired, even with well-known materials such as gold, manganese, and indium. This rather lengthy discussion was intended to illustrate the difficulty that could be encountered in planning ITC irradiations in AARR, as well as to supply the detailed information required.

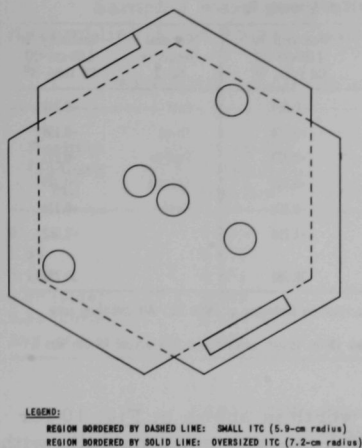
An ITC neutron temperature that is higher than expected for an H₂O region might be attributed to neutron diffusion into the ITC from the surrounding fuel region. Again, as stated in regard to the manganese CdR, such an effect extending to the axis of the ITC would be surprising, and other explanations may eventually be found.

The data listed in Table VIII, in Ref. 3, and elsewhere indicated that the cadmium ratios were lowest in the small ITC and with the greatest fuel loading density. Higher cadmium ratios than in AARR, except for ²³⁵U fission, could be achieved in AHFR.¹ Much higher cadmium ratios are achievable with graphite, beryllium, or D₂O than with H₂O moderator. As an example, in a 97.5% D₂O-filled ITC 68 by 68 cm square,³ gold and manganese cadmium ratios were 80 ± 5 and 400 ± 50 , respectively. The higher cadmium ratios appear to be achieved at a lower thermal-neutron flux.

C. Reactivity Worths of Boron and Cadmium Absorbers in the ITC

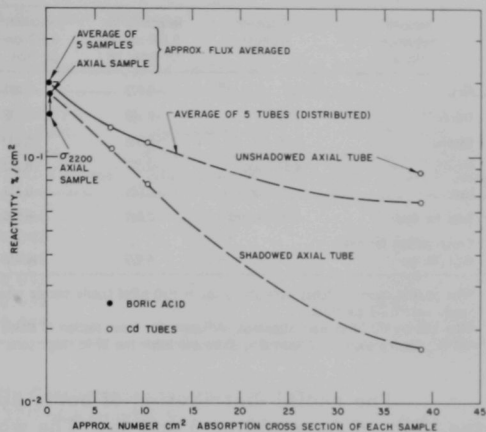
Measurements were made of the reactivity worths of dilute boric acid (H₃BO₃), and of various sizes and numbers of (hollow) cadmium tubes, in the small ITC. These measurements were made only in Assemblies 3 and 4a. The absorbers ranged from dilute samples to heavily shadowed arrays, positioned as shown by Fig. 8. Samples were withdrawn individually during reactor operation. Reactivities were measured by rising periods or by control-blade compensation.

The average reactivity worth per square centimeter of absorber distributed along the axis of the ITC in a core-length sample is plotted in Fig. 9 as a function of sample absorption cross section in square centimeters. Both shadowing and self-shielding are significant, even with fairly small samples. Data from these measurements are listed in Tables X, XI, and XII.



112-9045

Fig. 8. Sample Positions in the Small and Large ITCs, Used for Boric Acid, Cadmium, Aluminum, and Teflon Samples



113-1287

Fig. 9. Reactivity Worth of Various Sizes of Absorbers in ITC of Assembly 4a

TABLE X. Reactivity of Boric Acid and Lucite in ITC of Assembly 3

Sequence of Sample Removal	Position (radius), cm	1.27-cm-diam Lucite Rod, % ^b	H ₂ O-filled Lucite Tube, %	H ₃ BO ₃ -filled ^b Lucite Tube, % ^a	Net Reactivity of 21.7 mg B, %	2200-m/sec Cross Section of 21.7 mg B ^c	Average Reactivity/cm ² , %
Last	0.0	0.008	0.004	-0.018	-0.022	0.912	-0.0241
Third	1.59	0.009	0.004	-0.018	-0.022	0.912	-0.0241
First	3.18	0.009	0.004	-0.016	-0.020	0.912	-0.0219
Second	4.58 (edge)	0.006	0.003	-0.016	-0.019	0.912	-0.0208
Fourth	5.33 (corner)	0.006	0.0	-0.010	-0.010	0.912	-0.0110
Total of five	-	0.038	0.015	-0.078	(-0.093 for 0.1085 g)	(4.56)	-0.0204

^aThe Lucite tube was 1.27-cm OD and 0.95-cm ID and extended the full height of the core.

^bThe boric acid concentration was 3.81 g/liter for samples in Assembly 3, and 3.65 g/liter for Assembly 4a.

^cThe 2200-m/sec cross section for natural boron was taken to be $\sigma_0 = 755$ barns, or 42.03 cm²/g.

TABLE XI. Reactivity of Boric Acid in ITC of Assembly 4a

Sequence of Sample Removal	Position (radius), cm	H ₂ O-filled Lucite Tube, % ^a	H ₃ BO ₃ -filled ^b Lucite Tube, % ^a	Net Reactivity of 20.8 mg B, %	2200-m/sec Cross Section ^c of 20.8 mg B	Average Reactivity/cm ² , %
Last	0.0	-0.002	-0.011	-0.013	0.874	-0.0149
Third	1.59	-0.002	-0.016	-0.018	0.874	-0.0206
First	3.18	-0.002	-0.012	-0.014	0.874	-0.0160
Second	4.58 (edge)	-0.002	-0.010	-0.012	0.874	-0.0137
Fourth	5.33 (corner)	-0.002	-0.012	-0.014	0.874	-0.0160
Total of five	-	-0.01	-0.061	(-0.071 for 0.104 g)	(4.37)	-0.0163

^aThe Lucite tube was 1.27-cm OD and 0.95-cm ID and extended the full height of the core.

^bThe boric acid concentration was 3.81 g/liter for samples in Assembly 3, and 3.65 g/liter for Assembly 4a.

^cThe 2200-m/sec cross section for natural boron was taken to be $\sigma_0 = 755$ barns, or 42.03 cm²/g.

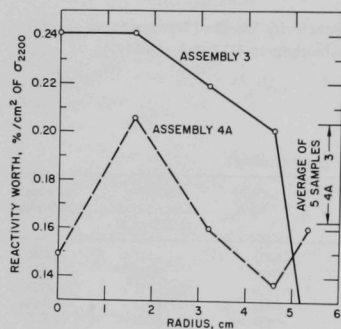
TABLE XII. Reactivity of Cadmium Tubes in ITC of Assembly 4a

Removal Sequence No. 1	Position (radius), cm	Reactivity for 0.190-cm-OD Cd Tube, % ^a	Reactivity for 0.292-cm-OD Cd Tube, % ^a	Reactivity for 1.08-cm-OD Cd Tube, % ^b	Removal Sequence No. 2	Reactivity for 1.08-cm-OD Cd Tube, % ^b
First	0.0	-0.073	-0.081	-0.064	Last	-0.341
Third	1.59	-0.100	-0.138	-0.284	Third	-0.159
Second	3.18	-0.098	-0.133	-0.257	Fourth	-0.271
Fourth	4.58 (edge)	-0.097	-0.133	-0.347	Second	-0.375
Last	5.33 (corner)	-0.079	-0.111	-0.306	First	-0.116
Total for five (distributed)		-0.447	-0.596	-1.256	-	-1.262
Cross section for one ($\pi DL/4$), cm ²	-	6.823	10.485	38.781	-	38.781

^aThe smaller cadmium tubes were placed inside H₂O-filled Lucite sample tubes described in footnotes of Table XI. All cadmium tube walls were 0.051 cm thick.

^bThe 1.08-cm-OD tubes were stoppered. Although the cross section is stated for an 18-in. length of cadmium, the actual length was 24 in., leaving about 3 in. extending above and below the 18-in.-high core.

The radial distribution of boric acid worth is shown in Fig. 10 for the ITCs of Assemblies 3 and 4a. The worth decreases monotonically with increasing radius in Assembly 3, but is quite irregular in Assembly 4a. Except at the corner, the worth is greater for Assembly 3 than for Assembly 4a.



113-1227

Fig. 10. Radial Distribution of Boric Acid Worth in ITCs of Assemblies 3 and 4a

As indicated by Table XII, the worth of an absorber varied with the presence or absence of neighboring absorbers, by as much as a factor of five. This dependence is shown by the two removal sequences which illustrate the difference in worth of the 1.08-cm-OD tube when removed first or last from the axial position.

D. Experiments with Aluminum, Beryllium, and Teflon in the ITC

Aluminum was of interest as a structural material in the AARR ITC, and also for use in alloying target material which might otherwise be unsuitable for irradiation exposure. Alloying with aluminum would provide convenient samples for irradiation of material having high absorption cross section, or other properties requiring dilution. Finally, aluminum or beryllium might be used to fill unoccupied ITC positions, or in sample changing during reactor operation. Beryllium is of interest as a filler or as an ITC liner which would reduce the water volume of the ITC and would thereby limit the magnitude of any accidental excursion accompanying possible loss of ITC coolant, boiling, or air entrainment. This hazard is discussed further in Section E below. Teflon and beryllium were found to be of nearly equal reactivity worth. The original purpose for use of Teflon was to simulate voids, and there was some duplication in the beryllium and Teflon experiments. Teflon measurements are also reported in Section X.D.

Samples were positioned as indicated by Fig. 8. Data taken in Assemblies 3 and 4b are given in Tables XIII and XIV, respectively.

TABLE XIII. Reactivity of Aluminum and Teflon in ITC of Assembly 3

Position (radius), cm	Reactivity (%) of 1.27-cm-diam Teflon Rod		Reactivity (%) of 1.27-cm-diam Aluminum Rod	
	%/% of ITC Volume		%/% of ITC Volume	
0	0.059	0.046	0.040	0.031
1.59	0.059	0.046	0.038	0.030
3.18	0.061	0.048	0.040	0.031
4.58 (side)	0.061	0.048	0.050	0.039
5.33 (corner)	0.039	0.031	0.022	0.017
Avg of five	0.056	0.044	0.038	0.030

TABLE XIV. Reactivity Coefficients of Beryllium and Teflon in ITC of Assembly 4b

Plan Areas (cm ²) Filled by			Reactivity Change, %	Reactivity Coefficient %/% of ITC Volume
H ₂ O	Beryllium	Teflon		
152.3	-	-	Reference run	
145.9	6.4 ^a	-	0.26 ^a	-0.062 ^a
126.5	25.8 ^b	-	0.94 ^b	-0.056 ^b
141.9	-	10.4	0.36 ^c	0.053 ± 0.005 ^c
139.3	6.4	6.6	0.24 ^d	0.055 ± 0.005 ^d
119.9	25.8	6.6	0.24 ^d	0.055 ± 0.005 ^d

^aReactivity of 2.54-cm-square axial column of beryllium, measured by difference in control-blade configuration from reference run.

^bReactivity of 5.08-cm-square axial column of beryllium, measured by difference in control-blade configuration from reference run.

^cReactivity of five 1.27-cm-diam Teflon rods and two pieces 0.64 x 2.54 and 0.64 x 3.81 cm, all extending the full height of the core, measured by remote removal with compensation by a calibrated control blade during reactor operation.

^dReactivity of the two outermost 1.27-cm-diam Teflon rods and two rectangular pieces as shown in Figs. 6 and 10.

The sample worths did not follow a simple correlation pattern, and the planning of ITC loadings does not appear to be simple. Comparison of the worths of aluminum and Teflon produced fair agreement, indicating that absorption cross section is the primary factor determining reactivity worth, provided that ITC water volume is not changed. If the absorption cross section of the 1.27-cm-diam aluminum rod is taken to be 0.8 cm², it should be 0.019% less reactive than the Teflon rod. The measured difference was 0.015%, which is in fair agreement.

The worths of Teflon and beryllium may be compared using the data of Table XIV. No significant reactivity difference is evident between the two materials.

The worths of equal volumes of Teflon in the ITCs of Assemblies 3 and 4b can be compared using the data of Tables XIII and XIV. The worth per percent of ITC volume occupied by Teflon is slightly less for Assembly 3 than for Assembly 4b. The reactivity effect of a given small void volume is almost the same in the ITC of Assembly 4b as in Assembly 2a or 3; however, the fraction of the ITC volume is less. Section E below shows that the positive coefficient extends to higher void fractions in Assembly 4b than in Assembly 3, and that the relationship described in this paragraph does not apply to large void fractions of the dimensions shown in Figs. 11-13. However, the Teflon worths agree well with the small void worths indicated by Figs. 14 and 15 (i.e., for zero void).

The side walls of the large ITC were changed from stainless steel to aluminum during the experiments with Assembly 4b. The 0.16-cm-thick wall panels are indicated in Fig. 6. The change was thought to reduce the $2200\text{-m/sec } \Sigma_a$ for 347 cm^3 of metal by ~ 0.1 , giving a total reduction of $\sim 35\text{ cm}^2$ in cross section. Judging by the water-level critical data listed in Table XV, the accompanying increase in reactivity was $0.68 \pm 0.03\%$. The reactivity coefficient for absorption cross section of roughly $0.02\%/cm^2$ is in good agreement with worths of absorbers in the other ITC measurements.

TABLE XV. Effect of Aluminum Wall and Beryllium in ITC of Assembly 4b

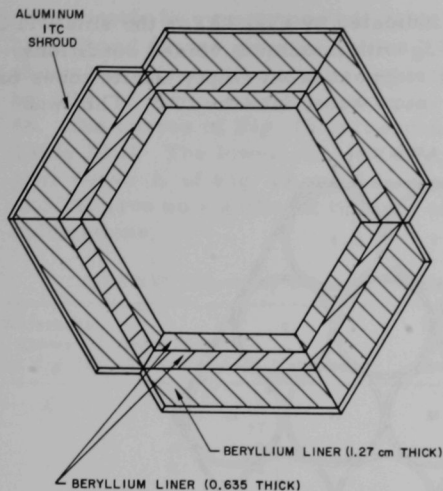
Condition of the ITC	Water Level ^b at Criticality, cm	Relative Reactivity Change, %
100% water ^a	120.72	0.0
2.5-cm-sq column of beryllium ^a	120.36	0.26
5.1-cm-sq column of beryllium ^a	118.70	0.94
100% water ^c	119.31	-
1.3-cm-thick beryllium liner ^c	115.22	-
1.9-cm-thick beryllium liner ^c	113.75	-
2.5-cm-thick beryllium liner ^c	112.64	-

^aStainless steel-walled ITC and axial beryllium columns.

^bThe top of the active fuel zone nominally is at 132.4 cm, and all control blades were withdrawn, for water-level control.

^cAluminum-walled ITC with up to 2.5-cm-thick beryllium liner inside aluminum wall.

Installation of beryllium ITC liners in the aluminum-walled ITC as indicated by Fig. 11 gave a slightly higher reactivity coefficient for the outermost (1.27-cm-thick) increment than shown for axial samples in Table XIV.



113-1213

Fig. 11. Large Aluminum ITC (7.2-cm equivalent radius) with Beryllium Liners

this is fairly similar to results obtained in Assemblies 3 and 4a, as well as those reported for AHFR.¹

E. Void Experiments in the ITC

Void worth was measured to determine the gain in reactivity obtainable by massive loss or displacement of water from the ITC. Incremental data were needed for the ITC design and to assist in writing operating procedures for sample loading and unloading. One-dimensional calculations were reported to underestimate ITC void worths, but two-dimensional calculations are considered to be in reasonably good agreement⁶ with the measured values for the small ITC. Calculations for the large ITC were not available when this report was written.

Dangerous increases in reactivity might occur in a poorly designed or improperly managed ITC, by accidental loss of ITC water because of air entrainment in the circulating system; or drainage; or by expulsion of ITC coolant by steam void formation accompanying an accidental power excursion; or loss of coolant flow. Teflon rod worths given in preceding pages of this report were taken as the worths of small-void fractions. Reference 1 reported full-length Teflon samples to be hardly distinguishable from air voids in the AHFR ITC, but reported a complicated reactivity curve for a plug of Teflon that was traversed axially in a void tube. No discrepancy was found in AARR experiments with Teflon and with voids.

Assuming a plan area of 47 cm^2 and a reactivity increase of 2% yields a coefficient of roughly 0.065% per percent of ITC volume filled by beryllium. As with the axial samples, the coefficient appears to diminish as the beryllium thickness increases.

As a rough approximation, the outer shell of beryllium recovered ~80% of the reactivity lost in changing from the small ITC to the large ITC and occupies a volume nearly equal to the reduction in fuel region because of the ITC change.

The beryllium and Teflon worths in the ITC of Assembly 4b are roughly twice as great as calculated from the absorption cross section of the water displaced, and

Locations of large voids are indicated by Fig. 12 for the small ITC and Fig. 13 for the large ITC. Starting with maximum voided conditions, the voids were removed by removing stoppers from empty Lucite tubes or by withdrawing Teflon rods to admit more water into the ITC. This was

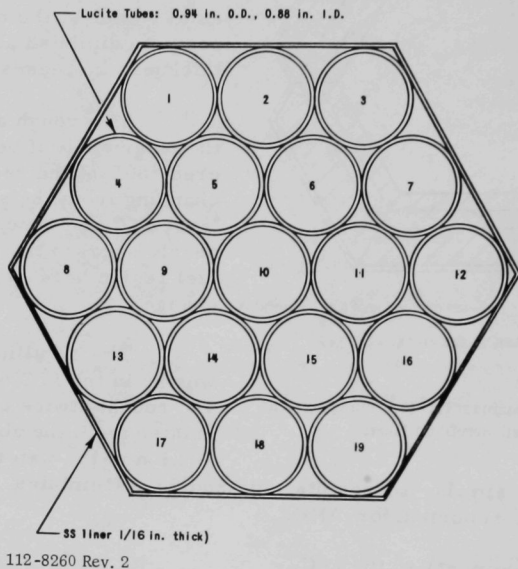


Fig. 12. Void Location in Small ITC

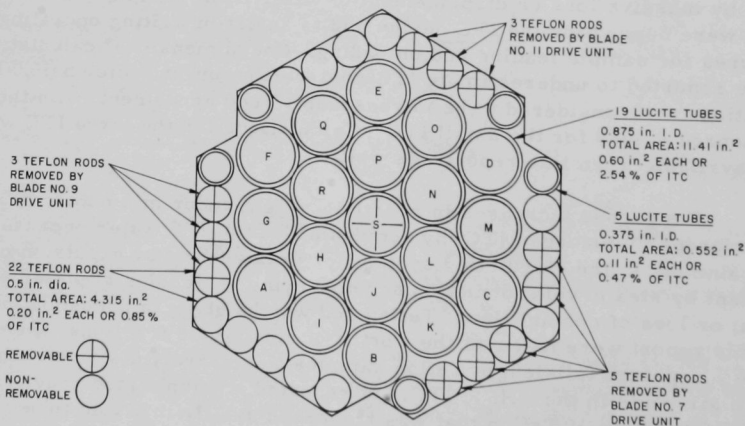


Fig. 13. Void Location in Large ITC

done mostly by remote control during reactor operation. Data for Assemblies 3 and 4b are given in Tables XVI and XVII, respectively. Figure 14 shows the effects of changing sequences of void removal for Assembly 3; but Fig. 15 shows only the most reactive sequences for Assemblies 4a and 4b. The curves of Fig. 15 correspond with the sequences given in Table XVII. The lower curve of Fig. 15 corresponds to the sequence that gave curve A of Fig. 14 and was part of an experiment at 24°C. A repeat at 53°C gave no significant change, after correction for changes in blade calibrations.

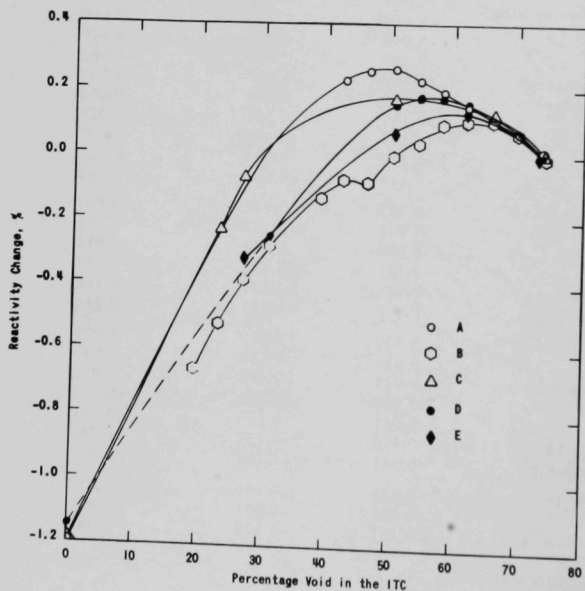
TABLE XVI. Reactivity Effects of Flooding Void Tubes in Small ITC of Assembly 3

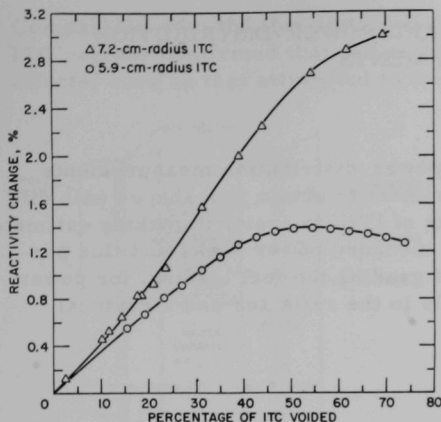
Reference Curve in Fig. 14	Sequence of Floodings	Tube No. ^a	Differential Change in Reactivity, %	Total Net Change in Reactivity, %	Average Differential Change in Reactivity per Tube, %
A	1	8	0.064	0.064	0.064
	2	17	0.049	0.113	0.049
	3	19	0.043	0.146	0.043
	4	12	0.044	0.190	0.044
	5	3	0.038	0.228	0.038
	6	1	0.034	0.262	0.034
	7	10 (center)	-0.008	0.254	-0.008
	8	16 (edge)	-0.030	0.224	-0.030
	9	Remaining 11	-1.431	-1.207	-0.130
B	1	10 (center)	-0.062	0.062	0.062
	2	15	0.038	0.100	0.038
	3	11	0	0.100	0
	4	6	-0.004	0.096	-0.004
	5	5	-0.060	0.036	-0.060
	6	9	-0.040	-0.004	-0.040
	7	14	-0.086	-0.090	-0.086
	8	8 (corner)	+0.008	-0.082	0.008
	9	16 (edge)	-0.056	-0.138	-0.056
	10	13, 17	-0.149	-0.287	-0.075
	11	18	-0.103	-0.390	-0.103
	12	19	-0.136	-0.526	-0.136
	13	4	-0.140	-0.666	-0.140
C	1	8 (corner)	0.067	0.067	0.067
	2	16 (edge)	0.055	0.122	0.055
	3	13, 17, 18, 19	0.046	0.168	0.012
	4	12, 7, 3, 2, 1, 4	-0.247	-0.079	-0.041
	5	10 (center)	-0.160	-0.239	-0.160
	6	Remaining 6	-0.962	-1.201	-0.160
D	1	8 (corner)	0.070	0.070	0.070
	2	10, 6	0.080	0.150	0.040
	3	16 (edge)	0.022	0.172	0.022
	4	12	0.002	0.174	0.002
	5	7	-0.021	0.153	-0.021
	6	5, 9, 14, 15, 11	-0.410	-0.257	-0.082
	7	Remaining 8	-0.891	-1.148	-0.011
E	1	5, 9, 14	0.126	0.126	0.042
	2	6, 11, 15	-0.065	0.061	-0.022
	3	17, 13, 8, 4, 1, 2	-0.387	-0.326	-0.065

^aTube numbers refer to tube locations shown in Fig. 12.

TABLE XVII. Reactivity Effects of Flooding Void Tubes in Large ITCs of Assemblies 4a and 4b

Void Flooded (Tube No., etc.) by Each Step ^{a,b}	% of ITC Volume Flooded by Each Step	Reactivity Change by Step, %	Reactivity Attributed to Remaining Void Volume, %	Remaining % of Void Volume in ITC
Assembly 4a				
None ^a	None	None	1.264 ^a	73.8 ^a
8	3.88	0.047	1.311	69.9
17	3.88	0.029	1.340	66.0
19	3.88	0.018	1.358	62.2
12	3.88	0.024	1.382	58.3
3	3.88	0.012	1.394	54.3
1	3.88	-0.007	1.387	50.5
10	3.88	-0.029	1.358	46.6
16	3.88	-0.049	1.309	42.7
15	3.88	-0.058	1.251	38.8
7	3.88	-0.102	1.149	35.0
11	3.88	-0.104	1.045	31.1
6	3.88	-0.133	0.912	27.2
2	3.88	-0.108	0.804	23.3
5	3.88	-0.139	0.665	19.4
4	3.88	-0.117	0.548	15.5
(Remaining four)	15.54	-0.548	0.000	Zero
Assembly 4b				
11 Teflon and 5 Lucite on Periphery ^b	11.7	0.521	0.521	11.7
Teflon on Blade Drive No. 11 ^b	2.6	0.120	0.641	14.3
Teflon on Blade Drive No. 7 ^b	4.3	0.179	0.820	18.6
Teflon on Blade Drive No. 9 ^b	2.6	0.108	0.928	21.2
Center Lucite P,Q,R ^b	2.5	0.118	1.046	23.7
Center Lucite M,N,O ^b	7.6	0.514	1.560	31.3
Center Lucite K,L ^b	5.1	0.245	1.992	38.9
Center Lucite G,H,I ^b	10.2	0.451	2.688	44.0
Center Lucite D,E,F ^b	7.6	0.195	2.883	54.2
Center Lucite A,B,C ^b	7.6	0.120	3.003	61.8
Center Lucite S ^b	2.5	0.115	0.115	2.5
Center Lucite P,Q,R ^b	7.6	0.343	0.458	10.1
Center Lucite M,N,O ^b	7.6	0.373	0.831	17.7

^aVoid location in Assembly 4a (see Fig. 12).^bVoid location in Assembly 4b (see Fig. 13).Fig. 14
Reactivity Change upon Flooding
Voided Tubes in the Small ITC
of Assembly 3, for Sequences
Shown in Table XVI



112-8218

Fig. 15. Reactivity Effect of Large Partial Voidings of Small and Large ITC of Assemblies 4a and 4b

The maximum reactivity changes obtained by ITC voiding in Assemblies 3, 4a, and 4b were 1.47, 1.35, and 3.0%, respectively. An even greater reactivity might have been achieved in Assembly 4b by redesigning the experimental equipment to achieve greater void fraction. ITC design should not permit accidental voiding of the nature that results in such large reactivity changes.

Void worth is further discussed in Section X.C.

As a generalization, the displacement of ITC water always reduced the thermal-neutron flux level in the ITC, and the hydrogen density appeared to be the governing factor.

V. RELATIVE ACTIVATION AND POWER-DISTRIBUTION MEASUREMENTS

A. Purpose

Foil-activation traverses and power-distribution measurements were made in the AARR critical experiment to obtain flux shapes with different loadings and with different sizes of ITC; to assist in making estimates of reactor power levels; to locate and measure power peaks and flux perturbations; to determine the results of grading the fuel loading, for power flattening; and to find irradiation levels in the reflector and structural components.

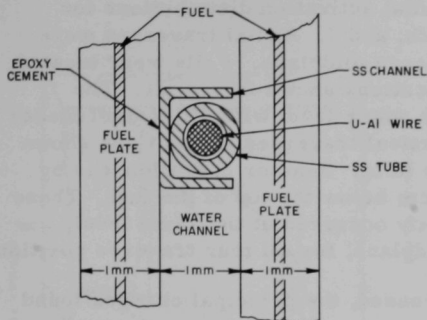
B. Experimental Method

Some of the activation traverses were made with disk-shaped foils, and some with wires of uranium-aluminum alloy. Table XVIII lists the foil and wire sizes and compositions. The disk-shaped foils were encased in 0.051-cm-thick cadmium or aluminum covers. In the ITC, these covers were supported by a Plexiglas strip. For the fuel zone, 1.27-cm-wide x 0.1-cm-thick aluminum spears were used to insert the covers in the 0.1-cm-thick coolant channels. For Assemblies 1 and 2a, Plexiglas foil holders supported the foil covers between the 10.16-cm-thick beryllium layers in the reflector. Assemblies following Assembly 2a contained 100% beryllium reflectors, and foil holders of Teflon were used instead of Plexiglas to avoid introduction of hydrogen into the reflector region. In the reflector of Assemblies 1 and 2a, a negligibly small flux perturbation was thought to result from displacement of water by the Plexiglas foil holder (dimensions 1.27 x 1.59 x 11.43 cm), which was inserted in a horizontal opening in the plastic of the reflector. The hydrogen density was 84% of that of the water displaced. A reactivity measurement for the foil holder gave a worth of 0.008% in reactivity in the ITC.

TABLE XVIII. Description of Activation Foils and Wire

Material	Composition	Diameter, cm	Thickness, cm
<u>Foils</u>			
Mn-Cu	88% Manganese 10% Copper	0.818	0.0064
U-Al	17.5 w/o Uranium (92.75 w/o enriched)	0.818	0.005
Indium	Pure metal	0.818 (or 1 x 1 cm sq)	0.005
<u>Wire</u>			
U-Al	16.5 w/o (enriched U)	0.05	

Comparison with the flux distributions found in beryllium or in voided ITC regions confirmed that the perturbation was small compared to other effects, such as that attributed to foil materials. (See Chapter IV).



112-6679

Fig. 16. Retaining Method for 0.05-cm-diam Uranium-Aluminum Wires in AARR Critical Assemblies

distributions, longer when the wire was to be cut up for a vertical traverse) were positioned inside the tubes before they were inserted into the channels.

For counting, the wire segments were wound into flat coils and placed on the regular foil planchets for the automatic counting equipment. The long wires used for vertical distributions were cut, after irradiation, into segments either 2.54 or 1.27 cm long, depending upon the spatial resolution desired.

The technique of coiling the wire segments for counting was tested by irradiating 16 wires, each 3.8 cm long, on a rotating wheel in a void in the graphite thermal column of the ATSR. The counting rates for the different wires, which were coiled in a variety of ways, showed no significant variations. Two-in.-diam NaI(Tl) crystals were used for gamma-counting the wire activities. For the fission-product investigations, energies below approximately 411 keV were biased out.

All counting data were processed by the computer codes RP-20¹⁶ or NURF,¹⁷ followed by further processing using the COMBO code.¹⁷ The latter code performs the normalizing and combining operations required when multiple detectors are used in counting, and when the results of two or more groups are to be compared using monitor foils. Statistical errors in the activation measurements were of the order of $\pm 0.5\%$ or less, except for some of the cadmium-covered manganese data points. In these cases, the statistical errors in the lower activations approached $\pm 3\%$.

The uranium-aluminum wires were used for measurements requiring a fine spatial resolution. For irradiation, they were retained as shown in Fig. 16. Small channels made from 0.013-cm-thick stainless steel were attached to the fuel-plate-retaining clips at the desired locations, extending from the bottom of the fuel element almost to the top. The channels were closed at the bottom. Stainless steel hypodermic-needle tubes of 0.075-cm OD were cut to such lengths that they protruded somewhat when inserted in the channels. Suitable lengths of the uranium-aluminum wires (4 cm for horizontal

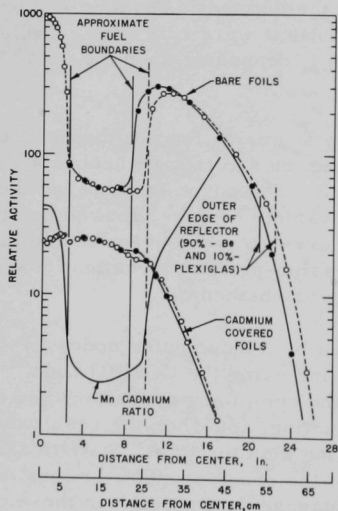
C. Horizontal Activation Distributions

1. Effect of Increased Fuel Loading Densities

Figures 17-20 show the radial activation distributions for manganese foils in Assemblies 1, 2a, 2b, and 3. Radial traverses were taken approximately 3.2 cm below the core midplane. Foils were located between the fuel plates at the radial locations shown in Fig. 21. The reactor was controlled by adjusting the water level with all control blades fully withdrawn. With Assembly 3, vertical traverses at positions shown in Fig. 21 were made using manganese foils. Reactor operation was by water-level control approximately 10 cm below the top of the fuel. These traverses indicated that the peak activity occurred at the same level, approximately 3 cm below the core midplane, for all four traverse positions.

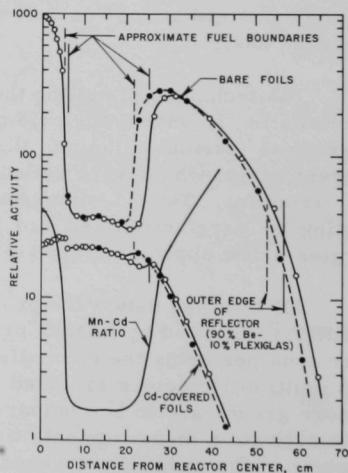
As the loading density increased, the principal changes found were these:

- Thermal-neutron activations of foils were noticeably lessened in the fuel region relative to those in the ITC and in the radial reflector.
- Cadmium ratios decreased in the fuel region. Cadmium ratios at or near the center of the ITC and in the radial reflector remained almost unchanged.
- A dip became more evident in the distribution of the manganese activity in the fuel region near the outer edge.



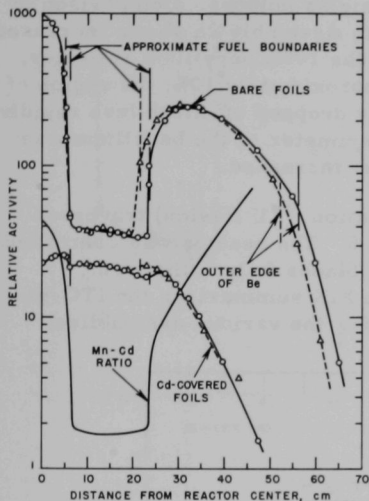
112-5718

Fig. 17. Manganese Radial Activation Traverses in Assembly 1



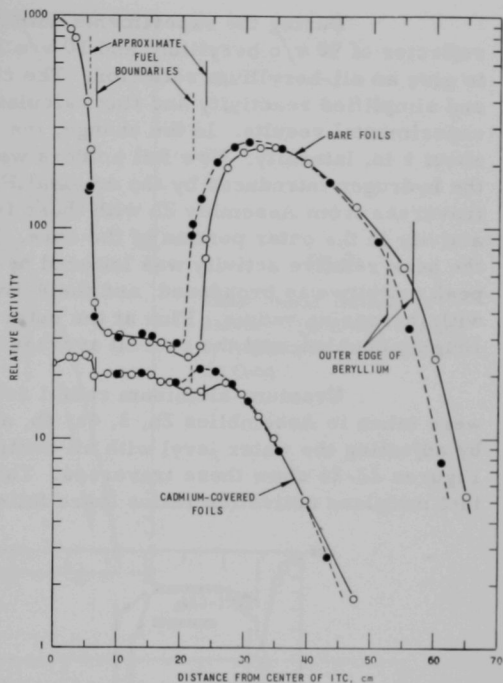
112-5719

Fig. 18. Manganese Radial Activation Traverse in Assembly 2a



112-5720

Fig. 19. Manganese Radial Activation Traverses in Assembly 2b (100% Beryllium Reflector)



112-5747

Fig. 20. Manganese Radial Activation Traverses in Assembly 3 (100% Beryllium Reflector)

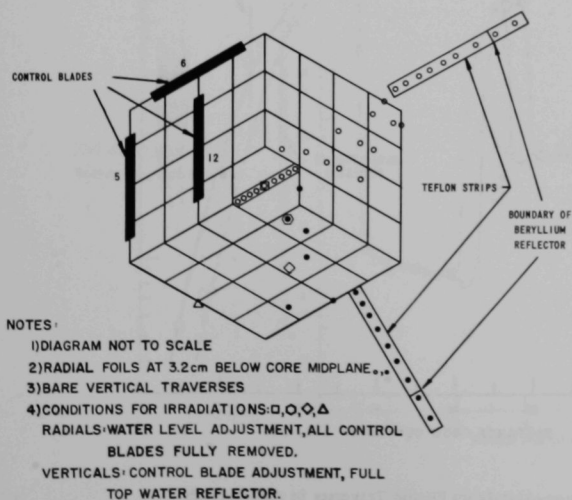
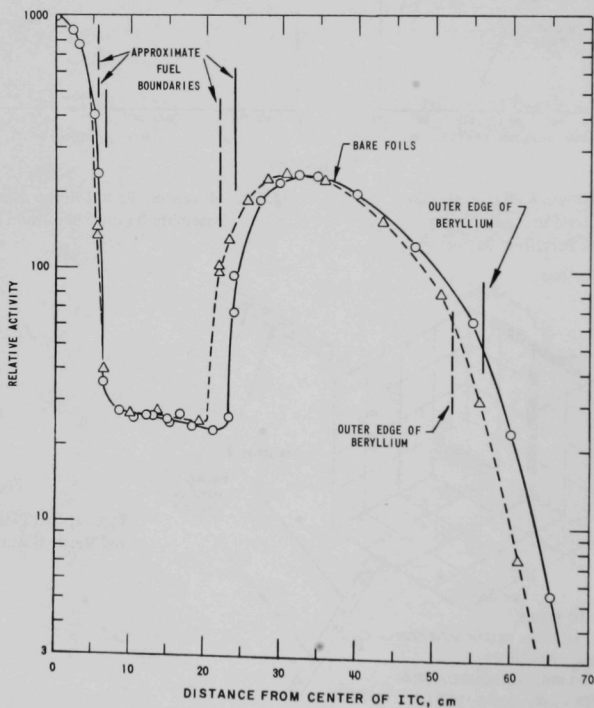


Fig. 21

Typical Foil Placement for Radial and Vertical Activation Traverses

During the experiments with Assembly 2, the original radial reflector of 90 v/o beryllium and 10 v/o Plexiglas by volume was modified to give an all-beryllium reflector. The change eliminated the heterogeneity and simplified reactivity and flux calculations, which were compared with experimental results. In the change, the traverse positions were shifted about 1 in. laterally. New foil holders were made of Teflon to eliminate the hydrogen introduced by the original Plexiglas holders. Comparison of traverses from Assembly 2b with those from Assembly 2a shows increased activity in the outer portion of the core. In the 100% beryllium reflector, the peak relative activity was lowered by approximately 10%, the region of peak activity was broadened, and the activity dropped off much less rapidly with increasing radius. Flux at the outer perimeter of the beryllium was roughly doubled, and the overall average was increased.

Uranium-aluminum radial activation (^{235}U fission) traverses were taken in Assemblies 2b, 3, 4a, 4b, and 5. The reactor was controlled by adjusting the water level with all control blades fully withdrawn. Figures 22-26 show these traverses. Table XIX summarizes the ITC-to-fuel midplane activation ratios (bare foils) for the various assemblies.



113-1282 Rev. 1

Fig. 22. Uranium-Aluminum Fission Traverses in
(No Plexiglas in the Beryllium)

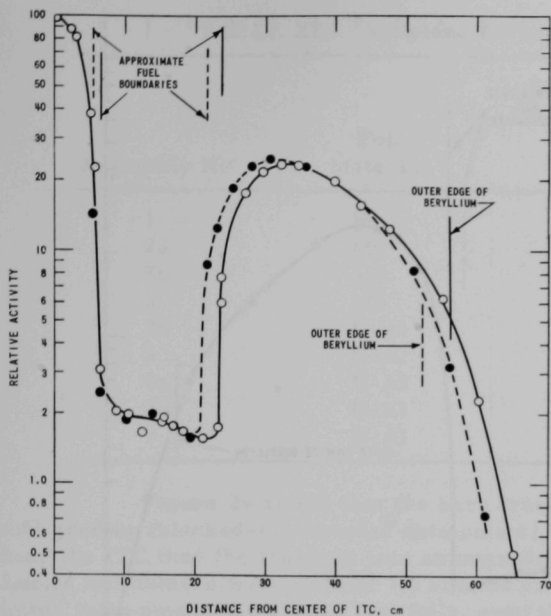


Fig. 23
Radial Fission Traverses in
Assembly 3 (Criticality Attained
by Adjusting Level of Water in
the Core)

113-1281

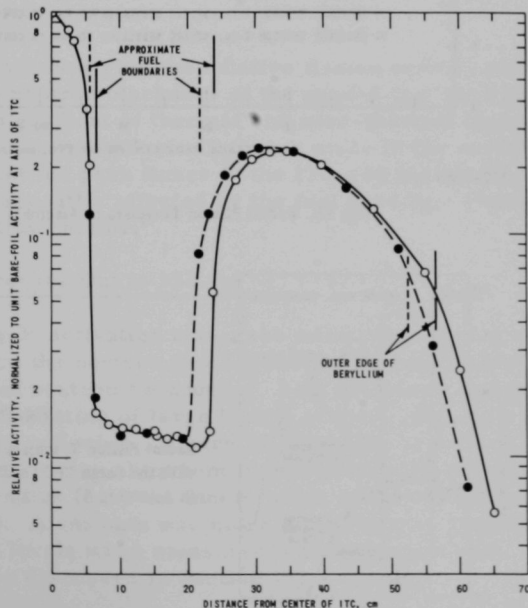
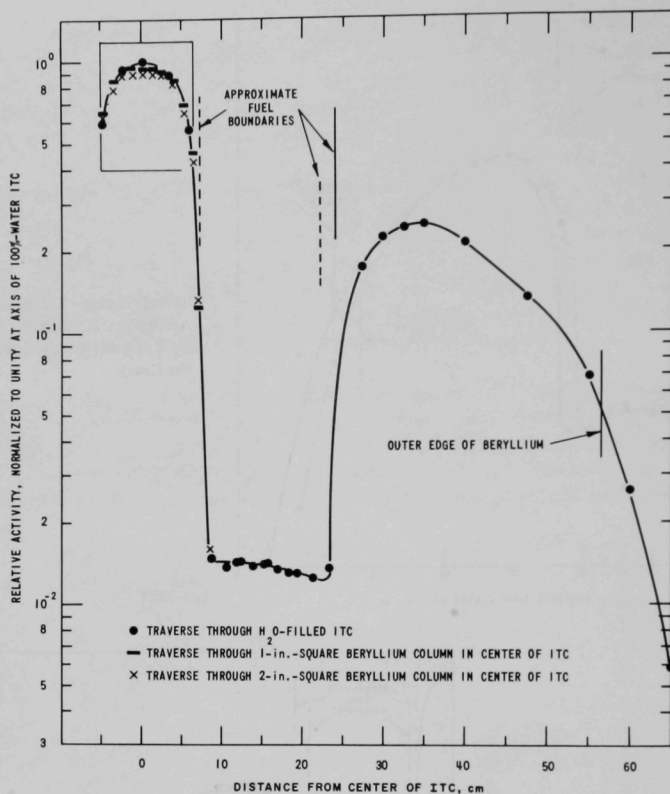


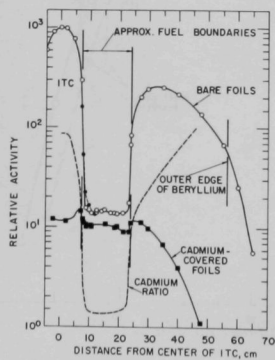
Fig. 24
Radial Fission Tra-
verses in Assembly 4a

112-7525



112-7558 Rev. 1

Fig. 25. Radial Fission Traverses in Assembly 4b



112-8220 Rev. 1

Fig. 26

Radial Fission Traverses in a Graded Loading
 with the Large ITC (Aluminum ITC Shroud)
 in Assembly 5

TABLE XIX. Midplane Activation Ratios

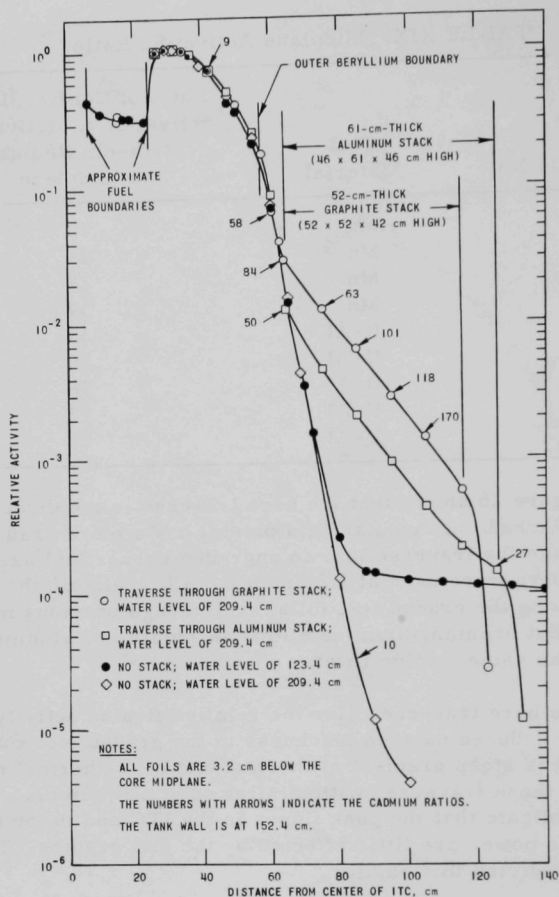
Assembly No.	Foil Material	Ratio of Central (ITC) Activation to Activation at 15-cm Radius, on Midplane
1	Mn	18
2a	Mn	28
2b	Mn	27
3	Mn	34
2b	U-Al	39
3	U-Al	55
4a	U-Al	78
4b	U-Al	72
5	U-Al	71

Figure 26 shows that the bare traverse in the direction of the fuel grading (blackened-in, circular data points) has a more gradual slope near the ITC than the traverse into an ungraded corner fuel assembly. Lucite foil holders were used at 7.6 and 8.2 cm to maintain the metal-to-water ratio among the graded fuel foils, even though previous measurements had indicated that uranium-aluminum foils in Lucite and aluminum foil holders yield the same fission rates.

The bare traverses give the relative fission activity per atom of ^{235}U , and the reduced neutron blackness of the graded fuel zone appears to result in a less steep gradient of thermal and near-thermal neutron flux. Comparison of these traverses with similar ones made in the ungraded Assembly 4b indicate that the peak fluxes in the ITC and in the beryllium per unit reactor power are little affected by the fuel grading. Theoretical analysis had predicted this earlier.²

2. Radial Traverses Out to 152 cm

In Assembly 3, activation traverses were taken during an investigation of ways to enhance the neutron flux beyond the reactor vessel, to help in determining designs of neutron "windows." Both aluminum and graphite "windows" were used, consisting of large blocks of these materials placed adjacent to the beryllium reflector. Figure 27 shows the traverses. Graphite proved to be more effective than aluminum in enhancing the thermal-neutron flux at a 152-cm (5-ft) radius (i.e., the inner radius of the vessel containing the critical experiment). Aluminum was more effective than graphite in later experiments where flux levels were measured outside a steel slab. Results of these experiments are discussed in Section VII.A below.



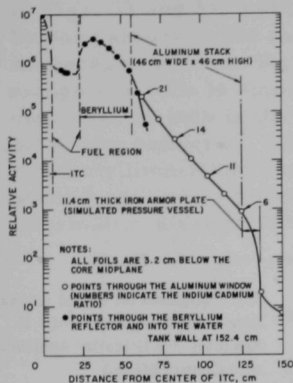
112-7371

Fig. 27. Radial Traverses with Indium Foils in Assembly 3

Indium-foil activations were too small to measure beyond 100-cm radius, unless water was displaced by aluminum, graphite, etc., or the top reflector was thin. Lowering the water level drastically, thus removing the top reflector, raised the activity distribution in the region beyond 80 cm. This apparently resulted from the increased flux of room-background neutrons that accompanies removal of the top reflector.

In a later experiment with Assembly 4a, an 11.4-cm (4.5-in.) thick slab of steel was installed at a radial distance of 122 cm (4 ft) from the vertical axis of the ITC, to simulate the presence of the wall of the

design pressure vessel, again using an aluminum window. Figure 28 shows the indium-foil traverse. It indicates that the operating flux level at the outer surface of the slab is about 2×10^{-6} times as high as the flux at the center of the ITC.



112-7459 Rev. 1

Fig. 28

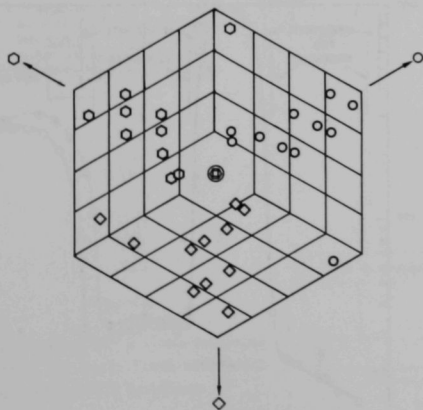
Radial Traverse with Indium Foils in Assembly 4a through Simulated Pressure Vessel

Other measurements have indicated that if more water is introduced between the beryllium and the pressure vessel (for example, as coolant passages in the aluminum), the measured thermal-neutron flux beyond the vessel drops significantly.

3. Flux-tilting Investigation

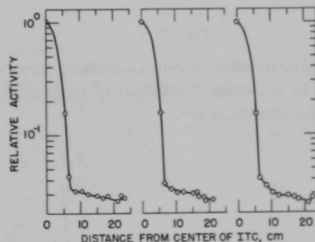
In Assembly 3, an experiment was performed to investigate the flux symmetry in the three 120° segments of the core. Manganese foils were used, with all control blades withdrawn, and the reactor was controlled by water-level adjustment. The foils were located as shown in Fig. 29, with the results given in Fig. 30. No large difference in core composition were indicated.

Also in Assembly 3, the flux-depressing effect of inserted control blades was examined. There was a full top reflector, and the blade configuration was as indicated in Fig. 31, which also shows the locations of the manganese foils used. Figure 32 shows the results



112-7457

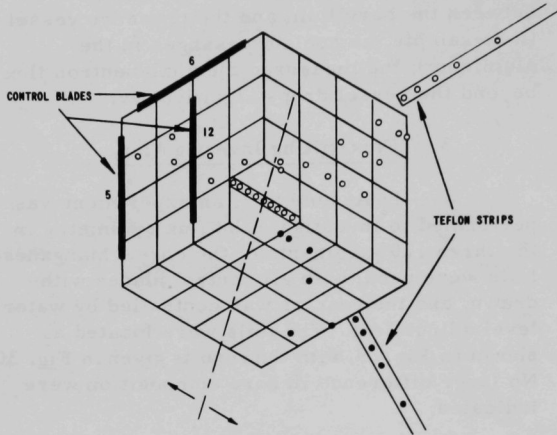
Fig. 29. Foil Locations for Flux Tilt Investigation with Manganese Foils in Assembly 3 (Criticality Achieved with Water Level Control)



112-7462

Fig. 30. Flux Tilt Investigation with Manganese Foils in Assembly 3

of this traverse. Comparing this figure with Fig. 20 shows that there is only a small (although noticeable) effect on the flux shape on the side of the core opposite the inserted control blades. The ITC flux shape remains nearly symmetrical.



NOTES:

1. FOILS AT 3.2 cm BELOW CORE MIDPLANE
2. DIAGRAM NOT TO SCALE
3. CRITICAL CONDITIONS: FULL TOP H_2O REFLECTOR
CONTROL BLADES NO. 5 AND 12 FULLY INSERTED
CONTROL BLADE NO. 6 AT 19.75 cm
ALL OTHER BLADES FULLY WITHDRAWN

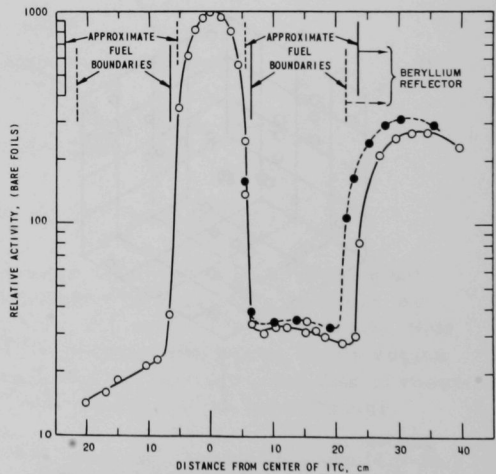
112-7529

Fig. 31

Foil Placement for Radial Activations with Manganese Foils in Assembly 3 (Criticality Achieved with Control Blades)

Fig. 32

Radial Activation Traverses with Manganese Foils in Assembly 3 (Criticality Achieved with Control Blades)



112-7554 Rev. 1

4. Foil Traverses inside Beam Tubes

Manganese foils were used to compare the activation levels along voided and beryllium-filled beam tubes. The foil locations are shown in Figs. 33 and 34, and the results in Figs. 35-37. These curves may also be compared with the radial traverse for Assembly 3 with no beam tubes in place, as given in Fig. 20. In general, the relative activity of the bare manganese foils is somewhat less in the beryllium-filled beam tubes, and considerably less in the voided beam tubes, than in the reflector peak of the beryllium reflector. The curve of Fig. 37, which is a longitudinal traverse in a beryllium-filled tangential beam tube, indicates a slight flux peak at about 8 cm beyond the corner of the core. These data are supplemented by information given in Section VIII.B.

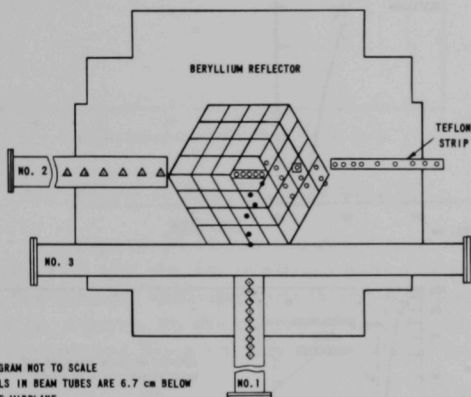


Fig. 33

Foil Locations in a Cross-sectional View of the Beam Tubes with Beam Tubes Voided

NOTES:

1. DIAGRAM NOT TO SCALE
2. FOILS IN BEAM TUBES ARE 6.7 cm BELOW CORE MIDPLANE
3. ALL OTHER FOILS ARE 3.2 cm BELOW CORE MIDPLANE
4. REACTOR CONTROLLED BY WATER LEVEL; ALL CONTROL BLADES FULLY WITHDRAWN

112-7527 Rev. 1

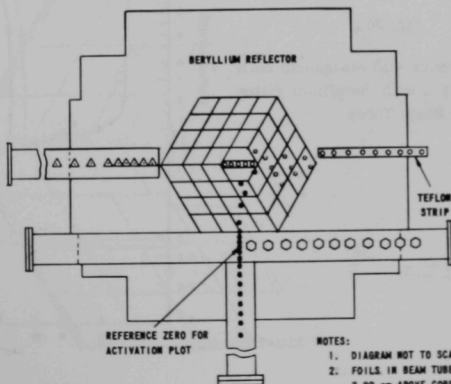


Fig. 34

Foil Locations in a Cross-sectional View of the Beam Tubes with Beam Tubes Filled with Beryllium

NOTES:

1. DIAGRAM NOT TO SCALE
2. FOILS IN BEAM TUBES ARE 2.99 cm ABOVE CORE MIDPLANE
3. ALL OTHER FOILS ARE 3.2 cm BELOW CORE MIDPLANE
4. REACTOR CONTROLLED BY WATER LEVEL; ALL CONTROL BLADES FULLY WITHDRAWN

112-7556

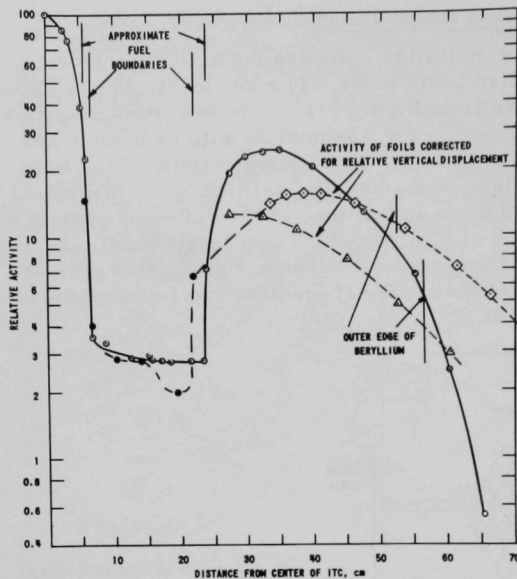


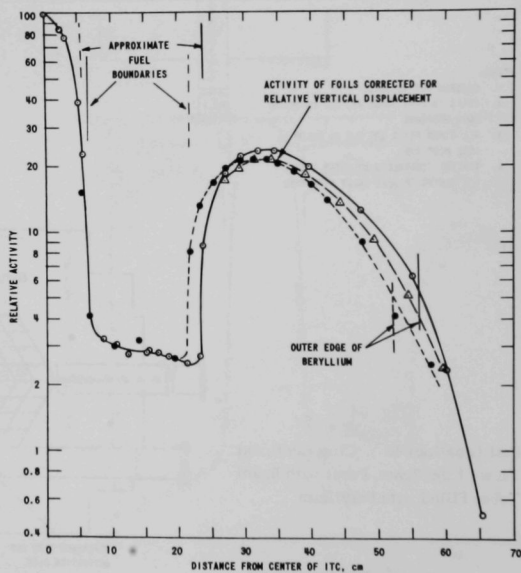
Fig. 35

Radial Traverses with Manganese
Foil in Assembly 3 with Beam
Tubes Voided

112-7528

Fig. 36

Radial Traverses with Manganese Foils
in Assembly 3 with Beryllium Filler
Plugs in the Beam Tubes



112-7526

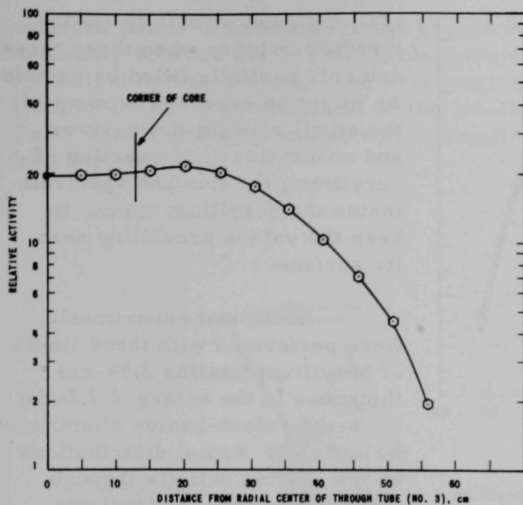


Fig. 37

Traverse with Manganese Foils in the Through Tube in Assembly 3 with Beryllium Filler Plugs in the Through Tube

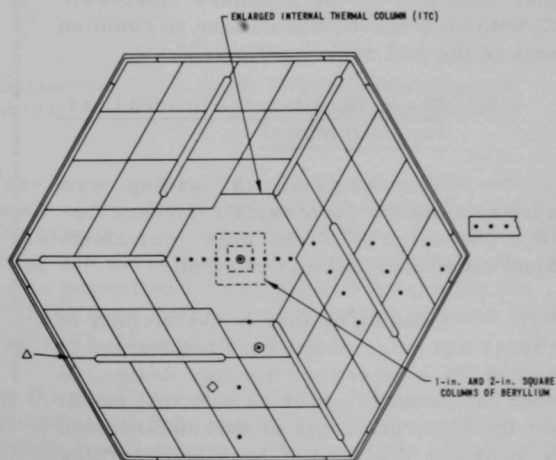
112-7551

5. Effect of Beryllium in the ITC

Figure 38 shows the placement of the large stainless steel-shrouded ITC and the six modified assemblies on its periphery. Figure 39 shows the activity distributions in the presence of columns of beryllium 1 and 2 in. square, in the center of the ITC (Assembly 4b). Beryllium is being considered for a variety of uses as a solid moderator in part of the

Fig. 38

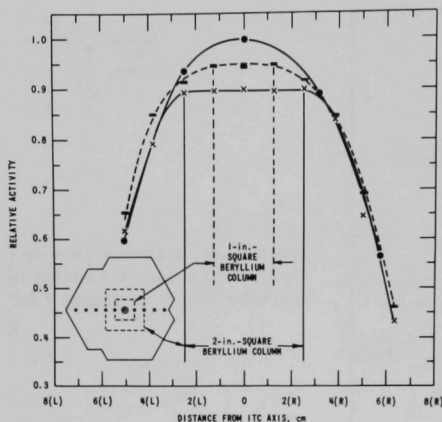
Plan View of Cores Containing Enlarged ITC



NOTES:

1. ● FOILS LOCATED 3.2 cm BELOW CORE MIDPLANE
2. VERTICAL TRAVERSES: ○ ○ ◇ △

112-7533



112-7532 Rev. 1

Fig. 39. Radial Fission Traverses through Beryllium Columns in the Large ITC

decreases monotonically as the thickness is increased. Successive irradiations with decreasing liners thickness were internalized through several foil activations in the fuel zone well away from the ITC shroud.

Radial ^{235}U fission-distribution curves for the 100% water-filled ITC show the aluminum-wall ITC peak value to be about 5% higher than that of the stainless steel-wall ITC, with both curves normalized to common values in the fuel zone.

6. Power Density in the Graded Loading, Assembly 5

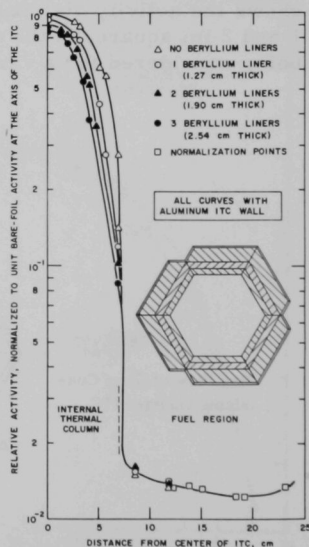
The Assembly 5 loading was graded to simulate the physics reference design. The large (7.2-cm area-equivalent-radius) aluminum ITC was present.

Grading of fuel in the vicinity of the inner and outer radial core boundaries is required in a practical reactor design, to reduce the peaks in power density that result from the steep gradients of thermal-neutron flux near the edges of a heavily absorbing core with highly moderating reflectors.

Activation traverses with wires of aluminum-uranium alloy were used to

ITC, e.g., for inserts in static-irradiation tubes when these tubes are only partially filled by samples. As might be expected because of the small slowing-down power and absorption cross section of beryllium, the flux and spectrum inside the beryllium appear to keep the values prevailing near its surface.

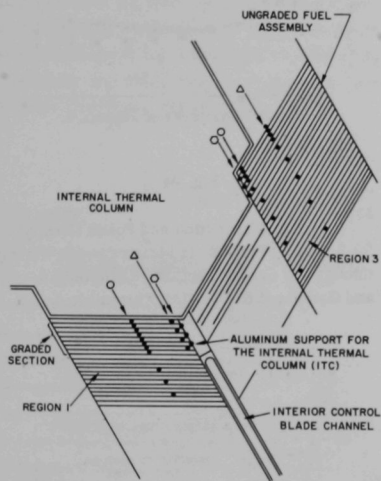
Additional experiments were performed with three liners of beryllium totaling 2.54-cm thickness in the enlarged 7.2-cm area-equivalent-radius aluminum-walled ITC. Radial distributions of ^{235}U fission activity through these liners (Fig. 40) indicate that the flux per unit power de-



112-8221 Rev. 1

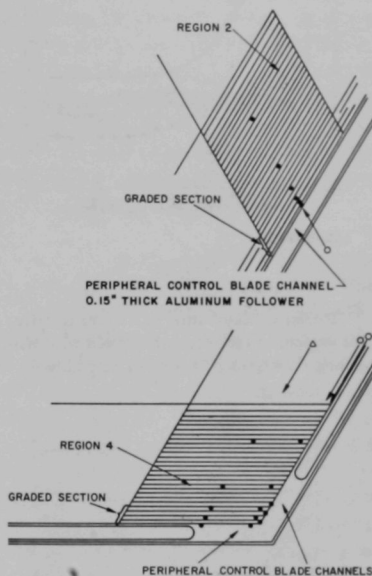
Fig. 40. Radial Fission Traverses through Beryllium Liners in the Large ITC

measure power distribution in the graded regions. The activations in Assembly 4c were made with all blades withdrawn, and with criticality controlled by water level. The wire segments were located approximately 3 cm below the core midplane, at the locations shown in Figs. 41 and 42. Two irradiations were made, with normalizing points located in Region 1 (see Fig. 41).



112-8994

Fig. 41. Approximate Channel Locations near the ITC in Assembly 5

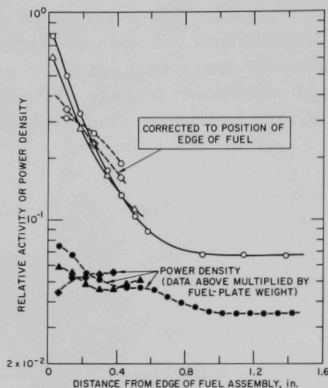


112-9004 Rev. 1

Fig. 42. Peripheral Subassemblies with Approximate Channel Locations, Assembly 5

The results are presented in Figs. 43-46, where the activation data are normalized to unity at the innermost point of Region 3 (shown in Fig. 41). To interpret the graphs, we must refer to Figs. 41 and 42, where the symbols used in plotting are correlated with location in the core. For Regions 1, 3, and 4, the data permitted interpolation to determine the activation rate that would have been observed at the edges of some of the fuel plates as shown by Figs. 43, 45, and 46.

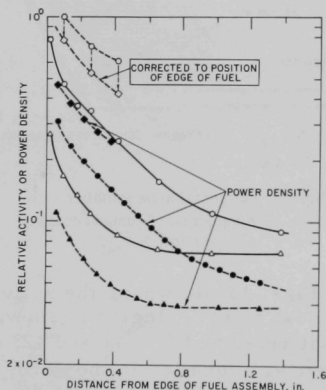
To determine the relative power density, we used the smooth curves drawn through the activation data and multiplied the ordinate at the location of each fuel plate by the weight of the fuel plate. These data are given as shaded points in Figs. 43-46. Each such point indicates a fuel plate, although not all fuel-plate locations have been explicitly shown outside the graded zones. The normalization is consistent from curve to



112-8993 Rev. 1

Fig. 43

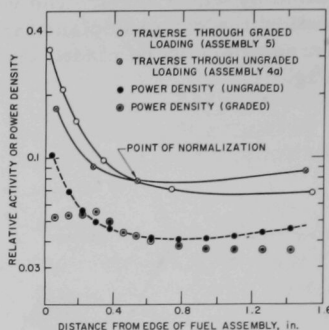
235 ^{235}U Fission Distribution and Power Density for Region 3, Fig. 41, as Measured with Wires through the Graded Section of Assembly 5



112-9002 Rev. 1

Fig. 45

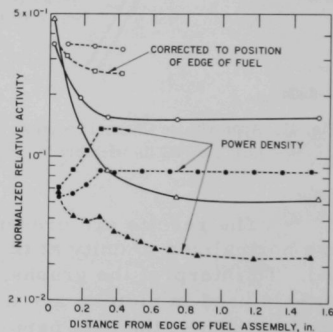
235 ^{235}U Fission Distribution and Power Density for Region 3, Fig. 41, as Measured with Wires in Assembly 5



112-9003

Fig. 44

235 ^{235}U Fission Distribution and Power Density for Region 2, Fig. 42, as Measured with Wires through the Graded Section of Assembly 5 and Compared to Data from Assembly 4a



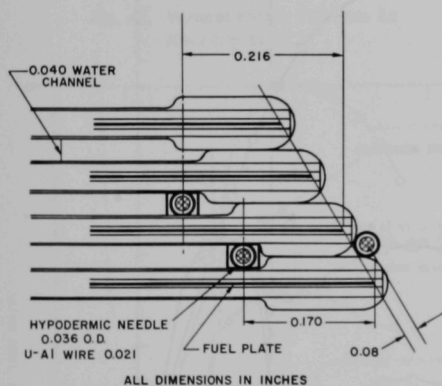
113-1223 Rev. 1

Fig. 46

235 ^{235}U Fission Distribution and Power Density for Region 4, Fig. 42, as Measured with Wires through the Graded Section of Assembly 5

curve and figure to figure, permitting direct comparison of the relative power density at all locations investigated.

Figure 43 (Region 1) shows the distribution through the graded region, near the ITC. Figure 44 (Region 2) shows the distribution in a graded assembly near the beryllium reflector; also shown is a traverse taken earlier through a uniformly loaded subassembly, with the data arbitrarily normalized to the later data at the indicated point. Figure 45 (Region 3) shows the area around one of the three re-entrant corners at the ITC where ungraded fuel protrudes. Figure 46 (Region 4) shows the distribution at the outer corner of the core where the graded fuel meets the reflector edge-on. The traverse points indicated by Figs. 45 and 46 were obtained by taping the wire segments to the edge of the fuel subassembly so that the centers of the wires were approximately 0.08 in. outside the fuel foils (Fig. 47).



112-8980

Fig. 47. Channel and Wire Locations near Fuel-foil Edges

A spot-check experiment was performed to confirm the assumption that the fission-rate distributions as measured with wires located between the fuel plates accurately indicated the fission-rate distributions in the fuel. A sample was punched from the middle of one of the 1.2-mil-thick fuel plates in the graded region, approximately 3 cm below the midplane, and the same was done for one of the regular 4.4-mil fuel plates located deeper in the core. The actual fuel-foil locations were 0.14 and 1.34 in. from the inner edge of a graded fuel assembly adjacent to the ITC. Radiochemical analysis of the fission

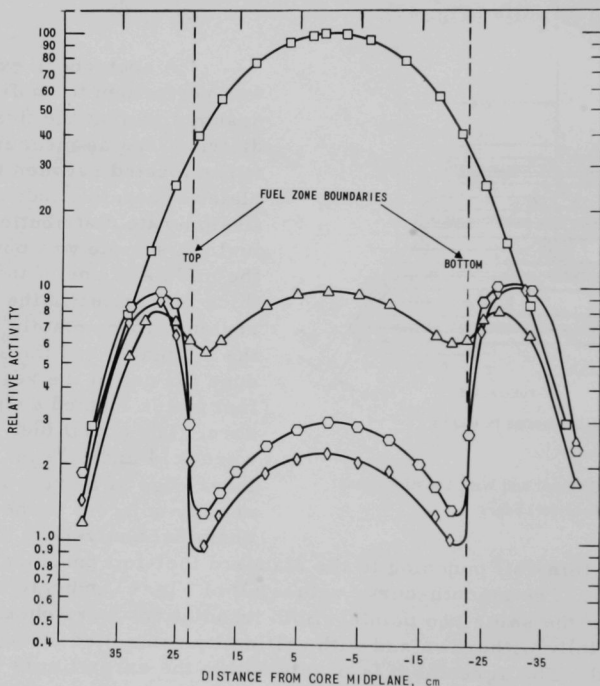
rate of the thin-foil punching to the standard fuel-foil punching yielded a ratio of 5.7. The smooth-curve values (O) of Fig. 43 indicate a ratio of 6.1 between the same two points. Both irradiations were obtained with all blades fully withdrawn and with criticality controlled by adjusting the water level. The agreement is barely within the error limits for these measurements.

D. Vertical Activation Distributions

1. Effect of Reactor Operating Conditions

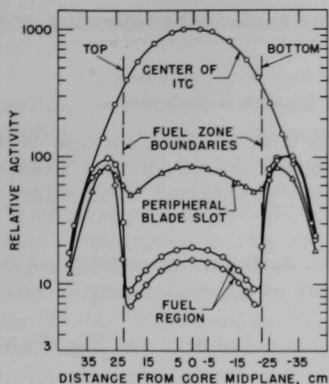
Figures 21 and 48 show the positions and relative activities of vertical uranium-aluminum (^{235}U fission) traverses for Assembly 3.

Figures 49 and 50 show similar curves for Assemblies 4a and 4b, respectively. For the vertical traverses in the enlarged ITC of Assembly 4b, the discontinuity in slope at the levels of the fuel-zone extremities correlates with the presence of heavy stainless steel rings at the ends of the large ITC. Foils on the periphery were taped to a simulated 0.20-in.-thick blade follower made of four sheets of 0.050-in.-thick aluminum. During irradiations, the reactor was controlled by the blades farthest from the traverse locations; a top reflector of ~37-cm H₂O for Assemblies 1, 2a, 2b and 3, and of ~78 cm for later cores, was present. In Assembly 3, a manganese radial traverse was irradiated with some inserted control blades (see Figs. 31 and 32). Results indicated that although the activations were depressed near the controlling blades, no perturbation occurred in the region of the normal vertical traverses.



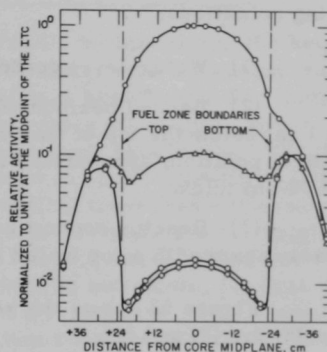
112-5749

Fig. 48. Vertical Fission Traverses in Assembly 3



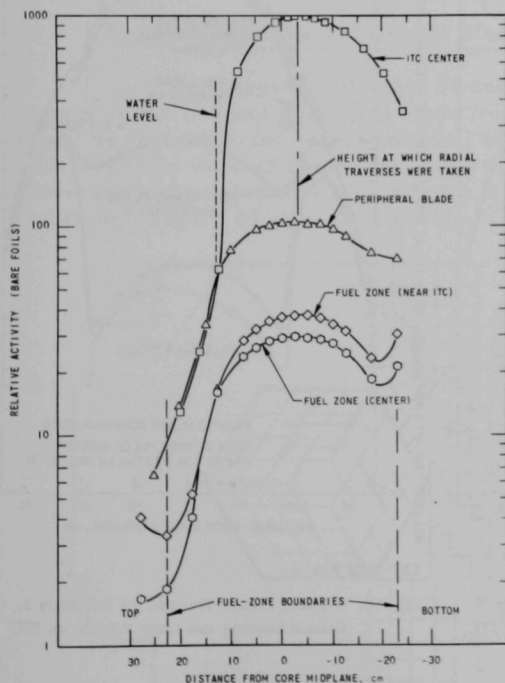
112-6543

Fig. 49. Vertical Fission Traverses for Assembly 4a



112-7464 Rev. 1

Fig. 50. Vertical Fission Traverses for Assembly 4b



112-7553

Fig. 51. Vertical Activation Traverses with Manganese Foils in Assembly 3 (Criticality Achieved with Water Level Adjustment)

For the radial traverses, the foils were 3.2 cm below the midplane of the fuel. Since these traverses were made with the reactivity controlled by water level and all blades withdrawn, some vertical traverses were made with water-level critical (in Assembly 3) to determine where the flux peak occurred, and whether this peak was at the same height in the different regions of the reactor. Figure 51 presents the results of this experiment.

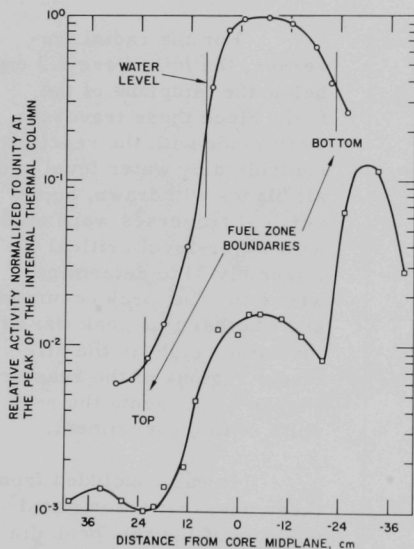
It was concluded from these data that the vertical position of the flux peak did not vary significantly from region to region, and that the peak was broad enough so that the level at which the traverses were located need not be varied from one set of irradiations to another.

For Assembly 5, vertical traverses were

made in the ITC and in the fuel zone under each of the following critical operating conditions:

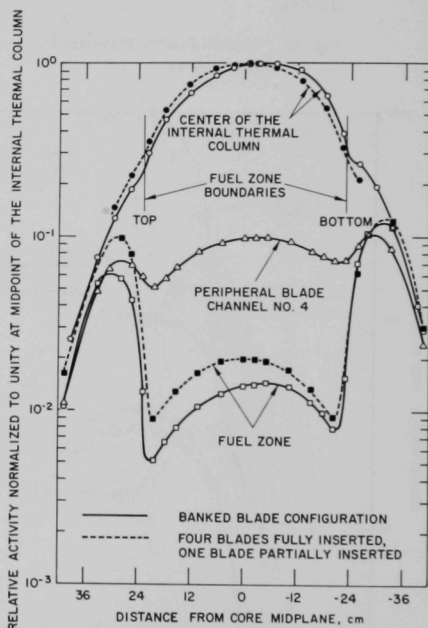
- (1) Water-level control, all blades withdrawn.
- (2) Banked peripheral blades with the hafnium tips of the blades 1 in. below the top of the fuel zone; the in-core blades banked at the critical position, approximately halfway withdrawn; a top water reflector 78-cm thick.
- (3) Reactor control by blades farthest removed from the two traverses, again with a top water reflector of approximately 78 cm.

Figure 52 shows the results for (1) above, and Fig. 53 shows the results for (2) and (3).



113-1229 Rev. 1

Fig. 52. Vertical Fission Traverse for Assembly 5; Graded Loading and Large Aluminum ITC, for Water Level Control



113-1228 Rev. 1

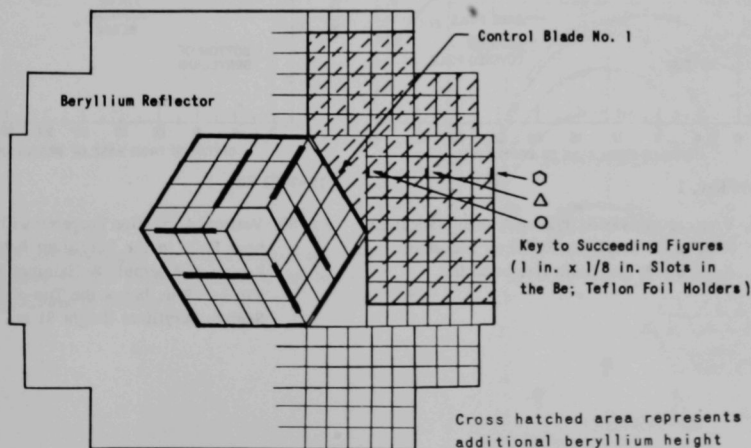
Fig. 53. Vertical Fission Traverse for Assembly 5; Graded Loading and Large Aluminum ITC

2. Effect of Increased Height of Beryllium Reflector

To investigate benefits obtainable by increasing the height of the beryllium reflector, we made vertical manganese activation traverses in the reflector with three different heights of beryllium. The installation of beam tubes in the added beryllium was under discussion, and the measurements were to determine the achievable flux levels. For the extra heights, beryllium blocks were added to almost one-third of the reflector, as indicated in Fig. 54, and vertical traverses were made at the designated locations. Figures 55 and 56 are plots for the original beryllium height of 48.3 cm (19 in.) and for 88.9 cm (35 in.). For the 78.7-cm (31-in.) intermediate height, which is not shown, the data inside the beryllium closely match the 88.9-cm (35-in.) data. These measurements indicate that extending the beryllium considerably above the fuel zone would substantially increase the neutron flux available in any beam tubes positioned at that level. A secondary consideration was the gain of about 1/4% in reactivity by addition of beryllium. An increase in height of the full reflector might add as much as 1% in reactivity.

3. Influence of a Peripheral Blade on the Flux in the Reflector

The traverses of Figs. 55 and 56 were made with an aluminum dummy in the channel of control blade No. 1. Since in the design reactor it might be desirable, for safety reasons, to have the peripheral blades poised with their tips near or somewhat below the top of the active fuel, the vertical traverses were repeated with blade No. 1 (see Fig. 54) at several different positions. Figure 57 shows the results when the tip of the hafnium was



112-7557

Fig. 54. Locations of Vertical Activation Measurements in the Beryllium Reflector Region in Assembly 3

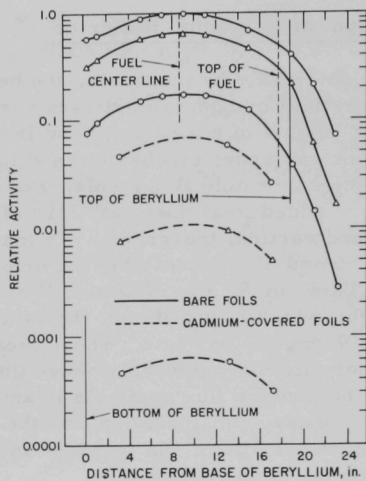
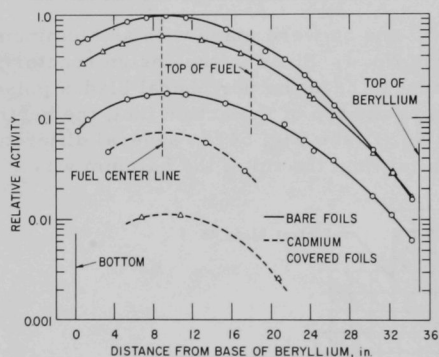


Fig. 55

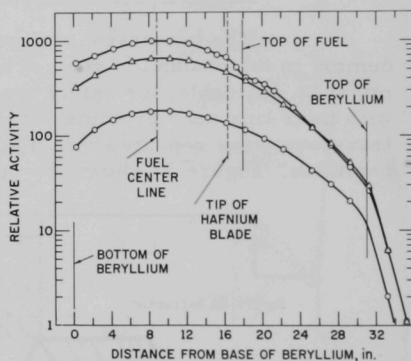
Vertical Activation Traverse with Manganese Foils in the Beryllium Reflector Region of Assembly 3 (Beryllium Height 19 in.)

113-1573 Rev. 1



113-1574 Rev. 1

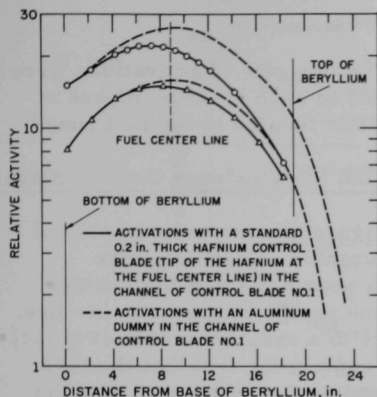
Fig. 56. Vertical Activation Traverses with Manganese Foils in the Beryllium Reflector Region of Assembly 3; Beryllium Height 35 in.



112-7461 Rev. 1

Fig. 57. Vertical Activation Traverses with Manganese Foils in the Beryllium Reflector Region of Assembly 3; Hafnium Blade Tip 1-1/2 in. below the Top of the Fuel Region, Beryllium Height 31 in.

3.8 cm (1.5 in.) below the top of the fuel [with 78.7 cm (31 in.) of beryllium]. Comparison with Fig. 56 shows that the flux at the upper end of the traverse at position A has been lowered by about 20%, but that there is no noticeable effect at the other two locations.



112-7466

Fig. 58. Vertical Activation Traverses with Manganese Foils in the Beryllium Reflector of Assembly 3; Hafnium Blade Tip at the Core Midplane, Beryllium Height 19 in.

1.27 cm wide \times 1/16 cm thick were used. The insert in Fig. 59 indicates the voiding pattern created by the 19 Lucite tubes and shows the locations

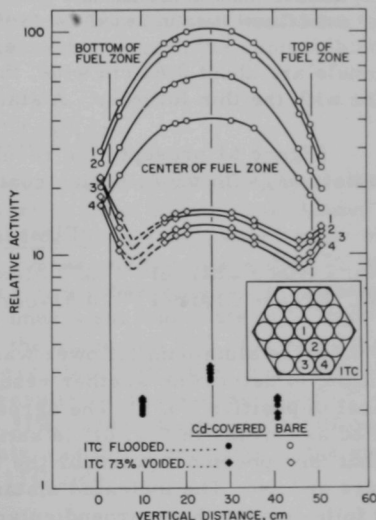
The effect on the reflector flux is more pronounced as blade No. 1 is inserted further. Figure 58 shows the results for a half-inserted blade, this time for the standard beryllium height of 48.3 cm (19 in.). Comparison with the broken lines, taken from Fig. 55, shows considerable flux depression at least as far out as position B (Fig. 54).

4. Effect of Voiding the ITC

In the course of investigating the effects of voids in the ITC for Assembly 3, as described in Section IV.E, vertical manganese activation traverses were made under conditions of 73% void and of full flooding (but with the Lucite tubes in place). Lucite-foil holders

Fig. 59

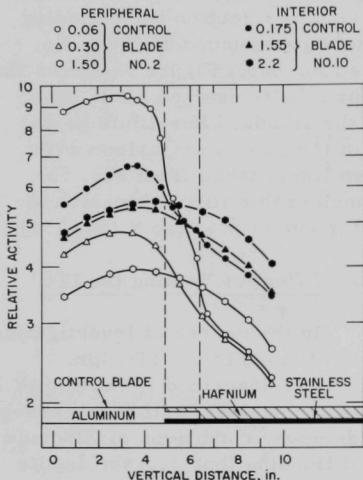
Vertical Activation Traverses with Manganese Foils in the ITC under Flooded and 74% Voided Conditions in Assembly 3



112-7465 Rev. 1

of the vertical traverses. Also presented in Fig. 59 are the traverse results, indicating the magnitude of the thermal-flux reduction due to removing 73% of the water. The cadmium-covered manganese activation was not very sensitive to the degree of voiding.

HORIZONTAL DIST. FROM EDGE OF SUBASSEMBLIES, in.



112-7467 Rev. 1

Fig. 60. Vertical ^{235}U Fission Distributions as Measured with Wires near Half Inserted Control Blades in Assembly 4a

channels are about 0.63 cm wide, there was approximately twice as much water with the thin follower. A stainless steel follower was also used.

Figure 61 presents the results. To obtain these data, we made two irradiations, with the following configurations:

	First Irradiation	Second Irradiation
No. 7 Blade Channel	SS follower	0.51-cm Al follower
No. 9 Blade Channel	0.51-cm Al follower	0.38-cm Al follower

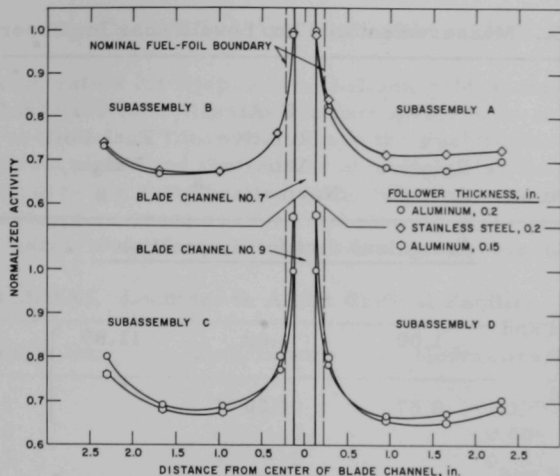
The 0.51-cm aluminum follower was used in each irradiation, once in each position, to determine whether results for position No. 7 would also be typical of position No. 9. The agreement between the two sets of data, plotted as circles in Fig. 61, is satisfactory. All data were internormalized so that the uppermost point for the 0.51-cm (0.2-in.) aluminum follower occurs at 1.00. The indicated distances are measured in the plane of the fuel foils, rather than perpendicular to the control blades.

The two sets of activations were normalized to each other by means of monitor foils located in the fuel zone.

E. Detailed Mapping near Control Blades

Figure 60 shows the results of vertical uranium-aluminum wire traverses near half-inserted control blades, one peripheral and one in-core. Reference to a radial traverse (Fig. 24) can help explain the fact that the peak flux in the interior of the fuel element near the peripheral blade is lower than for the in-core blade. There is typically a dip in the flux near the outer edge of the fuel zone.

The flux peaking due to the water-filled space beside control-blade followers was investigated using uranium-aluminum wires. Two different water thicknesses were obtained by using a thin (0.38-cm) aluminum follower and a regular (0.51-cm) aluminum follower. Since the blade



112-7463

Fig. 61. ^{235}U Fission Distribution as Measured with Wires near Control Blade Followers in Assembly 4a

These measurements indicate that the power peaking in fuel near control-blade followers is little affected by the use of a stainless steel rather than an aluminum follower. For the thin aluminum follower, which simulated more accurately the design control-channel water thickness, there was increased flux in the control channel itself, but little additional peaking in nearby fuel. The power peaking was most pronounced within the first $1/2$ cm of fuel at the control channel. The midplane maximum-to-average power ratio in a 27-plate subassembly next to the control-blade follower was approximately 1.25.

F. Determination of an Improper Fuel Loading

An experiment was performed with the graded loading (Assembly 5) to determine whether the mistaken insertion of an anomalously loaded fuel plate in place of one of the graded plates could be easily detected by an activation measurement. The six fuel subassemblies facing the ITC were used. Two of the six remained as reference subassemblies with unchanged graded loadings. Four subassemblies underwent fuel-plate substitutions at plate position 1 or 3 (counting from the aluminum ITC shroud). Uranium-aluminum foils on aluminum spears were placed on either side of the fuel foil in question. Table XX shows the results. For the cases studied, the activity perturbations range from 7 to 31%. The activity of the foil on the core side of the anomalous fuel plate was more sensitive to the anomaly than was the activity of the foil on the ITC side.

TABLE XX. Measurement of Flux Levels near Improper Loading

U-Al Foil Position	Relative Activity	U-Al Relative Activity Normalized ^a	Fuel Foil Weight, g	Approximate Thickness of Anomalous Fuel Foil, mils
<u>Anomalous fuel foil in position 1</u>				
Between				
ITC shroud and 1st fuel foil	1.00	1.00	11.89	0.9 (Ref.)
1st and 2nd fuel foils	0.67	1.00		
ITC shroud and 1st fuel foil	0.93	0.93	29.13	2.5
1st and 2nd fuel foils	0.54	0.81		
ITC shroud and 1st fuel foil	0.85	0.85	52.63	4.4
1st and 2nd fuel foils	0.46	0.69		
<u>Anomalous fuel foil in position 3</u>				
Between				
2nd and 3rd fuel foils	0.44	1.00	20.21	1.6 (Ref.)
3rd and 4th fuel foils	0.30	1.00		
2nd and 3rd fuel foils	0.41	0.93	38.80	3.3
3rd and 4th fuel foils	0.28	0.91		
2nd and 3rd fuel foils	0.39	0.89	52.69	4.4
3rd and 4th fuel foils	0.26	0.86		

^aEach foil position independently normalized to the activity of the reference foil.

VI. CADMIUM-RATIO MEASUREMENTS

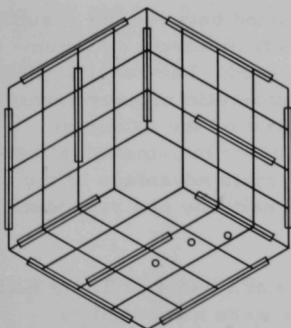
Cadmium ratios for dysprosium, indium, gold, manganese, copper, and ^{235}U (fission) have been measured in four AARR critical assemblies. The loadings are listed in Table XXI, where the Fuel/Boron column gives the number of fuel plates and the number of boron-poisoned stainless steel plates. The moderating ratio, defined to be $\xi \Sigma_s / \Sigma_a$, was calculated using 2200-m/sec absorption cross sections and slowing-down values ($\xi \Sigma_s$) of 20.4 and 0.45 barns/atom, for hydrogen and oxygen, respectively.

TABLE XXI. Loadings in AARR Critical Facility

Assembly No.	Fuel/Boron	Moderating Ratio ^a
1	315/000	1.190
2	615/420	0.606
3	810/810	0.447
4a	1215/1620	0.289

^aModerating ratio as defined in text.

Before irradiation, the foils were enclosed in capsules of 20-mil-thick cadmium or aluminum, which were then taped in holes cut in 40-mil-thick, 1/2-in.-wide aluminum strips. Each of these aluminum spears contained a pair of foils, one aluminum-covered and one, for the direct cadmium-ratio measurements, cadmium-covered. They were located so that they would be equidistant from the core midplane when the spear was inserted in one of the 40-mil water channels between the fuel-plate positions. The locations are indicated in Fig. 62. To preserve vertical flux symmetry, we used a full top water reflector and controlled the reactor by blades far removed from the foils.



112-5177

Fig. 62. Positions where Cadmium Ratios were Measured

When the cadmium ratio was close to unity, the "dysprosium substitution" (or "thermal activation") method was used. For a measurement of this type, each AARR location contained one dysprosium foil and one foil of the material

being used for the investigation. Simultaneously with the AARR run, an irradiation would typically be performed in the thermal column of ATSR, with the rising periods and times at power synchronized fairly closely. The thermal-column foils were mounted on a rotating aluminum wheel located in a 4-in.-wide void in the graphite stack. Typically there were two aluminum-covered foils and two cadmium-covered foils of each material.

The dysprosium substitution method provides fairly reproducible indications of the quantity cadmium ratio less one ($CdR - 1$), which is the ratio of subcadmium to epicadmium activation. Because of the transmission of errors, direct measurements result in large fractional variation of that quantity if the cadmium ratio is nearly unity. As described in Ref. 18, the following relationship was used:

$$\left[\frac{CdR_x - 1}{CdR_x} \right]_F = \left[\frac{A_y}{A_x} \right]_F \left[\frac{CdR_y - 1}{CdR_y} \right]_F \left[\frac{A_x}{A_y} \right]_T \left[\frac{CdR_x - 1}{CdR_x} \right]_T \left[\frac{CdR_y}{CdR_y - 1} \right]_T \cdot K, \quad (12)$$

where

$$K = \left[\frac{(\sigma \Phi)_x^{th}}{(\sigma \Phi)_y^{th}} \right]_F \left[\frac{(\sigma \Phi)_y^{th}}{(\sigma \Phi)_x^{th}} \right]_T. \quad (13)$$

Equation 12 permits estimation of the quantity $(CdR_x - 1)/CdR_x$ for a material x having a CdR of ~ 1 , by comparison of the activation rate with that of a material y which has a larger cadmium ratio in the same medium F. The subscript T refers to the thermal column. The evaluation of the factor K is described in Refs. 18 and 19, the latter being applicable to AARR neutron-energy distributions.

A small but systematic disagreement was found between the results of dysprosium-substitution measurements and data from direct cadmium-ratio measurements, wherever both methods were used. The results might indicate either an error of 1 to 2% in direct cadmium-ratio measurements (i.e., because of a lowering of the local fission source by the cadmium covers), or some difficulty with cross sections or other information affecting the application of the substitution method. The main advantage of the dysprosium-substitution method is the improved sensitivity and reproducibility in cores having hardened neutron spectra.

Foil materials for the AARR measurements are listed in Table XXII. All diameters were 0.818 cm. Relative activations were measured by gamma scintillation counting using NaI (Tl) detectors.

TABLE XXII. Foil Materials Used in Cadmium-ratio Measurements

Material	Nominal Thickness, cm	Isotope for CdR	Activation Half-life	Energy of Principal Resonance, eV
3.7 w/o Dy-96.3 w/o Al	0.023	^{164}Dy	2.3 hr	-
Iridium metal	0.0030	^{115}Ir	54 mo	1.457
Gold metal	0.0027	^{197}Au	2.7 days	4.91
90 w/o Mn-10 w/o Cu	0.0063	^{55}Mn	2.58 hr	337
Copper metal	0.0051	^{63}Cu	12.8 hr	580
17.5 w/o U-82.5 w/o Al (U of 92.75% Enrichment)	0.0051	^{235}U Fission	-	-

Table XXIII lists the observed cadmium ratios. Each value is the average for three to five locations inside the fuel region, the assigned errors being derived from the observed scatter of the individual measurements and from the estimated precision of the determination. For indium and gold, the direct cadmium-ratio measurements have been corrected for episcadmium absorption by the 0.051-cm-thick cadmium covers.²⁰

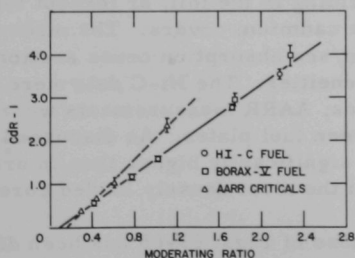
TABLE XXIII. Cadmium Ratios in Fuel Region

Assembly No.	²³⁵ U (Fission)	Dysprosium	Indium ^a	Gold ^a	Manganese	Copper
1	3.36 ± 0.10	10.8 ± 0.6	1.28 ± 0.02	1.23 ± 0.02	2.38 ± 0.06	2.11 ± 0.02
2	2.00 ± 0.04	5.87 ± 0.20	1.163 ± 0.020 1.130 ± 0.008 ^b	1.126 ± 0.006 1.111 ± 0.005 ^b	1.59 ± 0.02	1.54 ± 0.02
3	1.65 ± 0.05	4.36 ± 0.15	1.094 ± 0.010 ^b	1.080 ± 0.003 ^b	1.37 ± 0.01	1.29 ± 0.03
4a	1.37 ± 0.03	2.99 ± 0.16	1.060 ± 0.005 ^b	1.041 ± 0.004 ^b	1.21 ± 0.02 1.165 ± 0.008 ^b	1.14 ± 0.01 1.130 ± 0.009 ^b

^aIndium and gold activation data are corrected to foil thicknesses of 0.003 and 0.0028 cm, respectively.

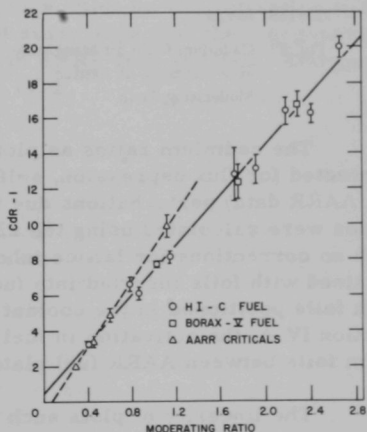
^bDysprosium substitution values for a cadmium cutoff energy of 0.53 eV.

Figures 63-68 are plots of the cadmium ratios from the AARR criticals (Table XXIII), along with cadmium ratios previously measured in the Hi-C series of critical assemblies.²¹ In these graphs, the solid lines are least-squares linear fits to the Hi-C and BORAX-V data points, and the dashed lines were drawn through the AARR data points. The lengths of the error bars are determined by the reproducibility of the determinations, or by the scatter of the measurements for several core locations which should give similar results. Error limits that are less than the height of the symbol are not shown.



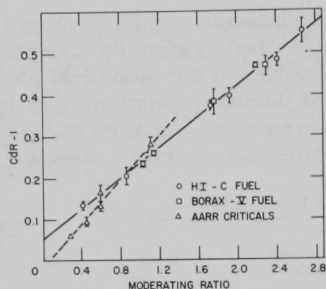
113-1587 Rev. 1

Fig. 63. Fission Cadmium Ratio as a Function of Lattice Moderating Ratio



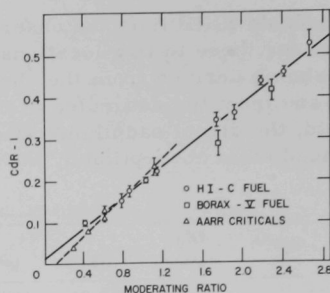
113-1567 Rev. 1

Fig. 64. Cadmium Ratio of Dysprosium as a Function of Lattice Moderating Ratio



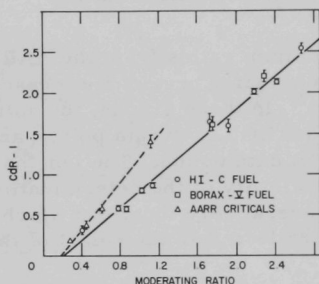
113-1592 Rev. 1

Fig. 65. Cadmium Ratio for 1.2-mil Indium as a Function of Lattice Moderating Ratio



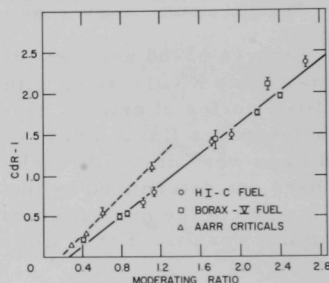
113-1585 Rev. 1

Fig. 66. Cadmium Ratio for 1.1-mil Gold as a Function of Lattice Moderating Ratio



113-1591 Rev. 1

Fig. 67. Cadmium Ratio for Manganese as a Function of Lattice Moderating Ratio



113-1588 Rev. 1

Fig. 68. Cadmium Ratio for Copper as a Function of Lattice Moderating Ratio

The cadmium ratios as plotted in these figures have not been corrected for flux depression, self-shielding in the foil, or (except for the AARR data) perturbations due to the cadmium covers. The moderating ratios were calculated using the 2200-m/sec absorption cross sections, with no corrections for lattice inhomogeneities. The Hi-C data were obtained with foils inserted into fuel rods; AARR measurements were with foils positioned in the coolant between fuel plates. As discussed in Section IV.A, the activation in fuel was significantly higher than in uranium foils between AARR fuel plates, in the most densely loaded core.

The linearity of plots such as those of Figs. 63-68 has been discussed elsewhere.^{21,22} The moderating ratio is the most important factor in determining the cadmium ratio, with other factors playing a secondary role.

A possible explanation for the difference in slope between the AARR and Hi-C results is as follows: An elementary two-group analysis²¹ shows that lattice inhomogeneities have little effect on cadmium ratios when the foils are exposed to a representative sample of the flux in the fuel, as was the case with the Hi-C and BORAX-V cores. In the AARR cores, measurements were with foils inserted into the coolant space between fuel plates. In the cores containing 315, 615, or 810 fuel foils, the remaining positions were stainless steel dummy plates, which resulted in thermal-flux peaks in the locality of the cadmium-ratio measurements. Thus it is logical that the cadmium ratios measured in the lighter AARR core loadings are higher than would have been measured in the fuel of AARR. Finally, there was a noticeable thermal-flux depression near the foils because of the increased absorption cross section and the water displacement associated with AARR activation foils, covers, and holders. This effect required a correction factor of 1.15 in the Assembly 4 absolute power determination, where samples punched from fuel plates were compared with bare foils irradiated in coolant channels. (This correction was not applied in Table XXIII or Figs. 63-68, because any similar effect on epicadmium activation has not been measured, and the effect on bare foils has been measured only in Assembly 4.)

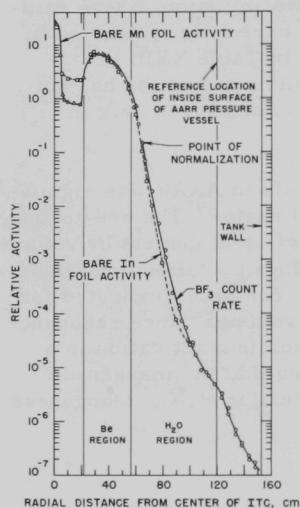
The epicadmium activation of manganese foils in AARR was significantly depressed by resonance shielding in the fuel region. The one-to-one, metal-to-water ratio results in nearly 45% stainless steel content by volume in the fully loaded core, and even more in the loadings containing stainless steel dummy plates. A maximum of 2% manganese content is indicated for Type 304 stainless steel, or nearly 1% of the core volume. Since resonance activation of manganese is roughly half of its epicadmium activation in a $1/E$ neutron-energy distribution, it is not surprising that the manganese cadmium ratios are substantially higher in AARR than in Hi-C. Manganese activation is discussed further in Section IV.B.

VII. NEUTRON-DENSITY MEASUREMENTS NEAR MOCKED-UP AARR PRESSURE VESSEL, BEAM TUBE, AND SHROUD

A. Flux Level at Location of AARR Startup Instruments (Measured in Assembly 3)

If no arrangements were made to increase leakage of neutrons locally through the 4-ft inside-radius pressure vessel of AARR by the use of neutron "windows," the flux detectors for reactor operation would have necessitated penetrations for access into regions providing more satisfactory geometry. Additional vessel penetrations would be difficult and expensive. The radial thermal-neutron flux distribution was measured with water filling the space beyond the beryllium reflector of the AARR Critical Experiment, out to the 5-ft inside-radius vessel (see Fig. 69). The BF_3 counter was used at large

radii because of its higher sensitivity to neutrons than manganese or indium foil. The flux is seen to be considerably less than 10^{-6} as great at 122-cm (4-ft) radius as at the ITC peak. Installation of 11.4-cm ($4\frac{1}{2}$ -in.) thick carbon steel pressure vessel reduced the flux still further, and it was desired to increase the flux by a factor of about ten at the radius of the AARR startup detectors (~ 137 cm). The desired ratio of flux at that point to flux at the ITC peak is about 10^{-6} .

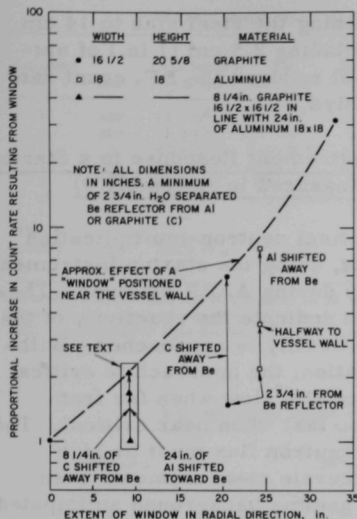


112-7370

Fig. 69. Composite Radial Traverse with Various Neutron Detectors

As indicated by Fig. 27, displacement of water by installation of a graphite thermal column, or by aluminum as well, substantially raised the flux level at the periphery. Figure 28 is a similar traverse made with the 11.4-cm-thick steel slab, simulating the pressure vessel of AARR design, positioned at 122-cm (4-ft) radius.

Several measurements were made using a stationary BF_3 neutron counter and various thicknesses of material in the "neutron window." Before the 11.4-cm-thick steel slab had been installed, the BF_3 counter was positioned at about 157-cm radius. It was end-on toward the reactor vessel and touched the outside. A collimator was constructed around the BF_3 detector to shield against room-scattered neutrons. The collimator wall included an inner liner of 1.27-cm thickness of Plexiglas, and layers of cadmium and Benelex. The shield thickness was about 12.7 cm.



113-1285 Rev. 1

Fig. 70. Effect of Extending a "Neutron Window" in the Radial Direction

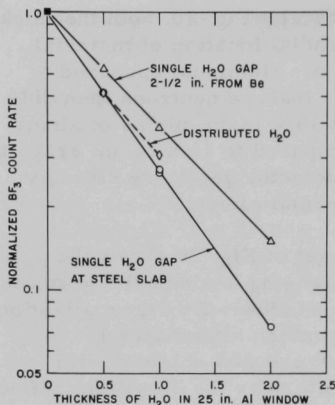
proportional change in the count rate was about the same as if no aluminum were present. However, the normalization count rate was representative of that expected from Fig. 70 for about 30 in. of aluminum.

Later, the 11.4-cm-thick steel slab was installed and the BF_3 detector was situated just outside the slab at about 137-cm radius to simulate AARR startup detector geometry. With a 46 x 46 x 63.5-cm aluminum stack situated between the steel slab and the beryllium reflector, the BF_3 detector count rate indicated a flux of $\sim 40 \text{ n/cm}^2/\text{sec}$ per watt of reactor power, which is $\sim 10^{-6}$ as great as at the ITC peak. The aluminum window was estimated to contain about 2 v/o of H_2O , which would be a reasonable coolant volume if distributed properly. However the desired distribution had not been determined at the time and a uniform distribution was used for the experiment.

Variations were made to cover the range of H_2O content of interest in the design. As shown by Fig. 71, the H_2O content data were nearly linear on a semilog plot. A water gap of a given thickness attenuated the count rate more effectively if positioned near the steel slab than at intermediate locations or near the beryllium reflector. Figure 71 differs from Fig. 70 in several respects, including the BF_3 detector position and the presence of the steel slab.

As shown by Fig. 70, both the thickness and the radial location of material were important. Aluminum appeared to transmit more leakage neutrons than did graphite, with 18 x 18-in. plates of aluminum being compared to 16 x 24-in. graphite stacks. The detector geometry strongly favored epithermal effects.

The inset of Fig. 70 shows the effect of rearranging a composite graphite and aluminum window. This normalization count rate was much higher than for the rest of Fig. 70, and was obtained with 8 1/4 in. of graphite near the beryllium reflector and 24 in. of aluminum between the graphite and the reactor vessel wall. The count rate increased as the graphite was moved out to the reactor vessel wall in two steps, each involving half of the graphite. The aluminum was moved 4 1/8 in. toward the beryllium during each step, to provide the reverse of the initial configuration after the second step. The pro-



113-1230 Rev. 1

Fig. 71. Effect of Inclusion of H₂O in Aluminum Window

Thickening the steel slab to 14 cm ($5\frac{1}{2}$ in.) by replacing 2.5 cm (1 in.) of aluminum by steel reduced the BF₃ count rate by almost a third.

B. Startup Instrument Response to a Startup Source (Measured in Assembly 3)

Subcritical neutron-multiplication measurements, using the startup instruments, are necessary during AARR startups. These measurements indicate the reactivity of the system as criticality is approached. Without this indication, the approach to critical might be wastefully slow when far from critical, or too fast when near critical. The source-level neutron flux must be high enough for accurate measurements even with the high gamma background anticipated in AARR after a few months of operation.

Measurements were made in the experimental facility to determine what instrument response could be obtained using a given source strength. Although a small, spherical (1.6-cm-diam) ¹²⁴Sb source was used for the experiment, several locations were tried to permit correlation between a spherical source and a rod-shaped source, and to indicate the effect of changing the radial location of the source.

This experiment was with a BF₃ detector geometry, approximately as described in Section VII.A. A flux of ~ 30 n/cm²/sec per watt of reactor power was indicated. The special source was calculated to have ~ 1.5 Ci of ¹²⁴Sb activity, with a radiation intensity as measured by gamma dosimeters, of ~ 26 R/hr at 30.5 cm (12 in.), in air. The source was inserted into a vertical air-filled tube extending to the midplane of the reactor, and the radial position was roughly midway between the inner and outer boundaries of the 30-in.-thick beryllium.

Table XXIV indicates the instrument responses as startup proceeded, reading from left to right, up to $k_{\text{eff}} \approx 0.993$. (Interlocks required the insertion of the old startup source, which was about 0.08 Ci, but in a more effective location than planned for AARR.)

Table XXV shows the instrument response as the special source was raised in 7.6-cm (3-in.) steps from the midplane. This measurement indicated that the source effectiveness decreased to half the value found at the midplane, when the source was raised to the height of the top of the fuel.

TABLE XXIV. Reactor Instrument Responses to 1.5-Ci ^{124}Sb Source, for Various Reactor Configurations

Instrument No.	Units	1.5-Ci Source In, No H ₂ O	Both Sources In	Blades 1 and 2 Raised	H ₂ O Raised	Blades 8, 10, and 12 Left In	Blade 12 Raised 25 cm	Old Startup Source Withdrawn
1	cpm	9.5×10^4	1.2×10^5	1.4×10^5	4.5×10^5	5.8×10^5	7.7×10^5	7.8×10^5
2	cpm	1.8×10^4	2.0×10^4	2.7×10^4	4.5×10^4	8.5×10^5	1.3×10^6	1.3×10^6
3	A	0.78×10^{-10}	0.78×10^{-10}	1.1×10^{-10}	2.5×10^{-10}	9.5×10^{-10}	13.0×10^{-10}	11.5×10^{-10}
4 ^a	A	0.16×10^{-10}	0.39×10^{-10}	0.53×10^{-10}	1.15×10^{-10}	10.5×10^{-10}	17.0×10^{-10}	14.2×10^{-10}
5	A	0.15×10^{-10}	0.17×10^{-10}	0.3×10^{-10}	0.48×10^{-10}	5.4×10^{-10}	8.2×10^{-10}	7.5×10^{-10}
6 ^b	A	0.71×10^{-9}	0.72×10^{-9}	0.75×10^{-9}	1.35×10^{-9}	1.9×10^{-9}	2.2×10^{-9}	2.07×10^{-9}
7	A	-	-	-	-	-	4.8×10^{-11}	4.0×10^{-11}
AARR location BF ₃	cpm	$3618 \pm 2\%$	$4074 \pm 2\%$	$5121 \pm 3\%$	$16.3 \pm 14\%$ (Background = $3 \pm 50\%$)	$273 \pm 2\%$	$447 \pm 2\%$	$377 \pm 2\%$

^aChannel 4 was instrument nearest old startup source, as shown in Fig. 1.

^bChannel 6 was instrument nearest special source, as shown in Fig. 1.

NOTE: The multiplication factor k_{eff} was estimated to be 0.90 with 10 blades fully inserted, and 0.993 with blades No. 8 and 10 inserted fully but No. 12 raised 25 cm.

TABLE XXV. Reactor Instrument Response as ~1.5-Ci ^{124}Sb Source Was Raised from Midplane

Instrument No.	Units	Old Startup Source Withdrawn	1.5-Ci Source Raised 3 in.	1.5-Ci Source Raised 6 in.	1.5-Ci Source Raised 9 in.
1 ^a	cpm	7.8×10^{5b}	6.0×10^5	4.9×10^5	3.0×10^5
2 ^a	cpm	1.3×10^{6b}	1.1×10^6	8.8×10^5	5.5×10^5
3	A	11.5×10^{-10b}	10.8×10^{-10}	9.0×10^{-10}	5.8×10^{-10}
4	A	14.2×10^{-10b}	13.3×10^{-10}	10.6×10^{-10}	6.8×10^{-10}
5	A	7.5×10^{-10b}	6.9×10^{-10}	6.0×10^{-10}	3.8×10^{-10}
6	A	2.07×10^{-9b}	1.85×10^{-9}	1.4×10^{-9}	0.83×10^{-9}
AARR location, BF ₃	cpm	$377 \pm 2\%$	$350 \pm 2\%$	$283 \pm 2\%$	$178 \pm 3\%$
Relative BF ₃ rate					
AARR location		1.00	0.93	0.75	0.47
Relative average for four instruments ^c		1.00	0.92	0.76	0.47

^aThe detectors for channels 1 and 2 were located far from the source but above the beryllium, roughly 10 in. above the midplane of the reactor.

^bFrom last column of Table XXIV.

^cChannel 7 was omitted because it was located near the source and higher than the source (resting on channel 3 detector).

NOTE: Reactor configuration was not changed during this experiment, except by raising the source from its initial midplane position.

The thermal flux at the BF₃ detector was estimated to be about $0.015 \text{ n/cm}^2/\text{sec}$ per curie of ^{124}Sb positioned at the midplane as described above, and with $k_{\text{eff}} \cong 0.9$. Extrapolating to AARR startup conditions indicated that a 1000-Ci ^{124}Sb source would produce about $1/2 \text{ W}$ of reactor power and ~9000 cpm response in the BF₃ detector, at the same reactivity level.

Following the experiments with the 1.5-Ci source in the vertical tube, it was used as a replacement for the old startup source. This permitted a measurement of instrument response versus radial position of the source. Unfortunately, the AARR BF₃ type detector had been removed, but the correlation with other instruments should be adequate. Table XXVI summarizes these measurements. Figures 1 and 2 show the geometry of the startup source mechanism.

TABLE XXVI. Instrument Response vs Radial Position of Source

Source-driven Interval, min		Source Location, in. Intended ^a Probable ^a		Channel 1		Channel 2		Channel 3, 10 ⁻¹¹ A	Channel 4, 10 ⁻¹⁰ A	Channel 5, 10 ⁻¹⁰ A	Channel 6, 10 ⁻¹⁰ A	Channel 7, 10 ⁻¹¹ A	Normalized Average, 1 and 2 Scalers	Normalized Average, 1-6 Detectors
				Scaler, cpm	Count-rate Meter, 10 ³ cpm	Scaler, cpm	Count-rate Meter, 10 ⁴ cpm							
0.00	0.00	Fully inserted		75,166	1.1	128,940	8.5	6.2	6.05	2.0	3.1	1.1	1.00	1.00
0.05	0.05	3.5	3.2	55,292	0.95	88,506	6.0	4.1	5.5	1.1	3.0	1.1	0.71	0.75
0.05	0.10	7.1	6.4	30,159	0.50	44,663	2.75	2.05	3.95	0.8	2.25	1.4	0.37	0.48
0.05	0.15	10.6	9.5	9,598	0.14	13,663	0.8	0.6	1.55	0.3	1.0	0.7	0.12	0.17
0.05	0.20	14.1	12.7	3,344	0.04	4,350	0.3	0.2	0.65	0.14	0.49	0.5	0.04	0.07
0.05	0.25	17.7	16.0	1,506	0.02	2,018	0.1	0.08	0.34	0.1	0.29	0.4	0.018	0.04
0.05	0.30	21.3	19.1	700	0.007	924	0.04	0.06	0.2	0.01	0.15	0.3	0.008	0.016
0.66	0.96	Fully withdrawn		6	0.001	19.5	0.01	0.00	0.002	0.01	0.01	0.1	0.0001	0.001
-	-	Fully inserted		74,789	1.4	128,214	9.0	6.3	6.0	1.8	3.1	1.5	0.995	1.04

^aSource location was estimated on the basis of timed intervals driven. There was no position indicator other than in-limit and out-limit lights, and the distance traveled between them was 66 in.

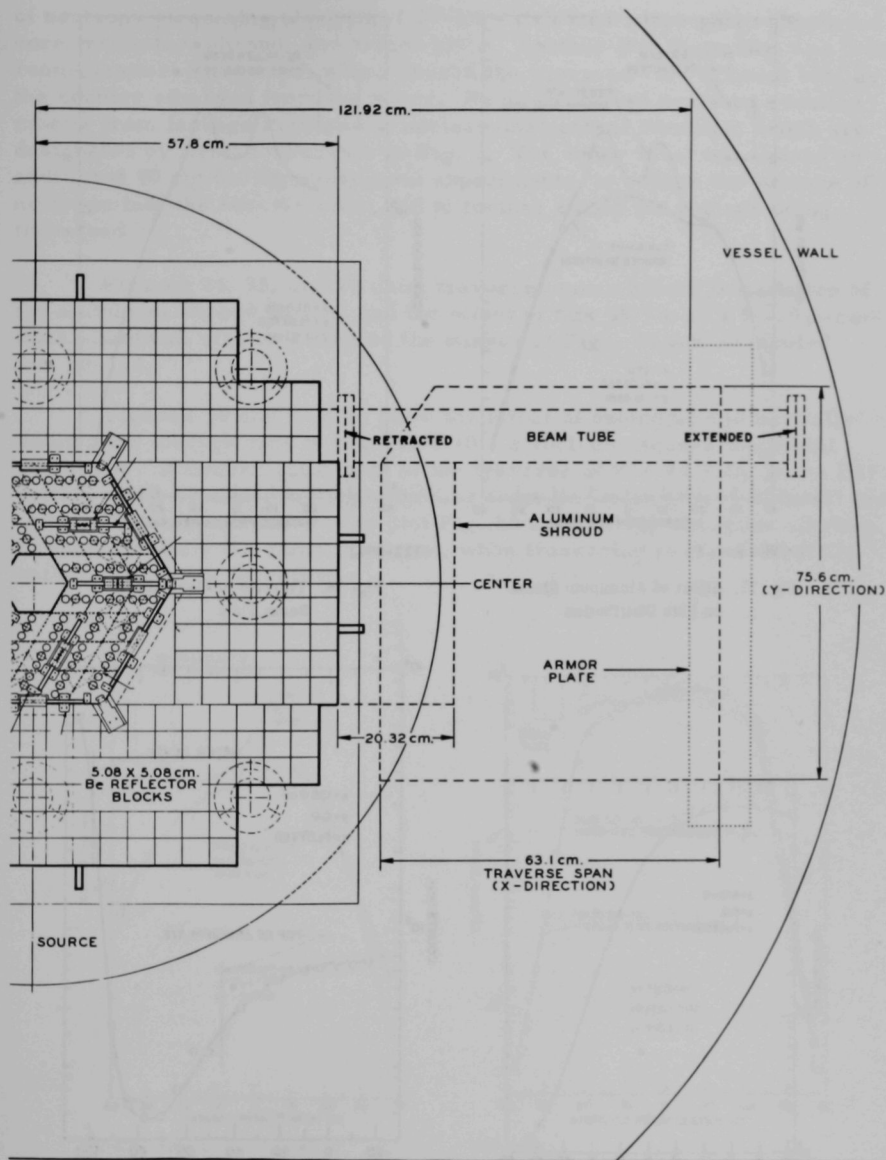
C. Radial Flux Perturbation near Beam Tubes (Measured in Assembly 4b)

Unavoidable leakage of neutrons from beam tubes results in increased radiation exposure locally of components through which these tubes pass. A number of traverses were made using a traveling BF₃ neutron counter to indicate the neutron distribution in the water near a 10.2-cm-square beam tube and other components perturbing the flux. Figure 72 shows the geometry of the region. The beam tube, when present, was a tangential one that passed completely through the beryllium reflector; both the retracted and extended positions are indicated. The traveling BF₃ counter could traverse the area shown and could also be raised and lowered by remote control. The piece of armor plate and the aluminum block that mocked up a portion of the reactor shroud were present for some of the experiments, as mentioned below.

The upper curve of Fig. 73 shows the count rate along a Y-direction traverse which passed close by the two aluminum braces (1.27 x 6.35 cm) attached to the 0.64-cm-thick aluminum retainer for the reflector blocks. The lower curve was made under identical conditions, except that the braces were removed. The twin peaks of the upper curve were attributed to streaming of neutrons through the braces, which nearly doubled the count rate in comparison to the unperturbed traverse.

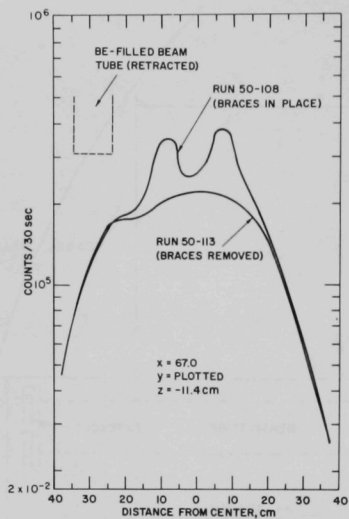
A perturbation near the beam tube is observable in Figs. 73 and 74. These traverses were made in planes above or below the beam tube, which was located at the midplane of the core (Z = 0). The beam tube was retracted during these traverses, with the portion inside the beryllium reflector filled with beryllium blocks. Filling was only about 80% complete because the selection of filler blocks was limited.

Traverses in the vertical (Z) direction are given in Figs. 75 and 76. The traverse at 67-cm radius intersects at the center traverses of Figs. 73 and 74. The traverse at 135-cm radius (Fig. 76) was just outside the armor plate, which was 70 cm high, 91 cm wide, and 11.4 cm thick. The armor plate roughly simulated a sector of 244-cm-ID pressure vessel. The shift downward in the peak flux indicated by Fig. 76 was attributed to leakage

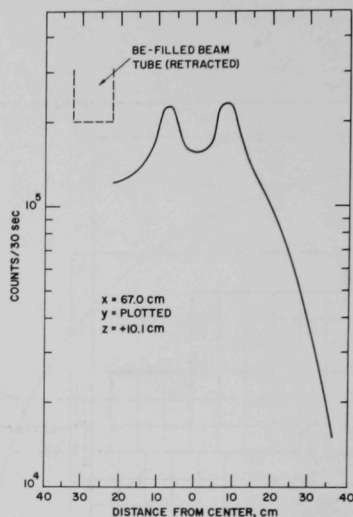


112-9006 Rev. 1

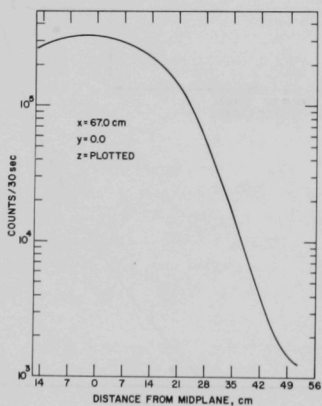
Fig. 72. Top View of AARR Critical Core with Mockup of Shroud, Pressure Vessel and Beam Tube



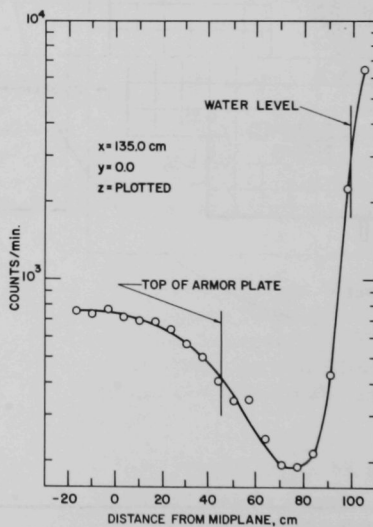
112-8985 Rev. 1

Fig. 73. Effect of Aluminum Braces
on Flux Distribution

112-8981

Fig. 74. Traverse in Plane above
Beam Tube

112-8989

Fig. 75. Vertical Traverse at Radius
of 67 cm

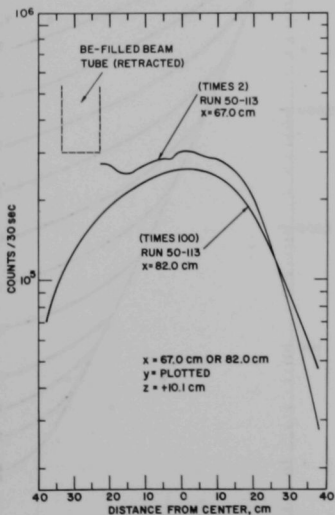
112-8987 Rev. 1

Fig. 76. Vertical Traverse behind
Armor Plate

of neutrons streaming along the 1.27-cm-thick base plate which supported core, reflector, shroud, and armor plate. Another flux distortion was from room-scattered neutrons, which caused the observed rise in count rate as the counter emerged from the water. Room-scattered neutrons resulted mostly from leakage through the nuclear-instrument thimbles, which are designated by Roman numerals in Fig. 1. The water level was raised an additional 90 cm during subsequent experiments, to reduce the leakage of neutrons into the reactor room and to further shield the regions being traversed.

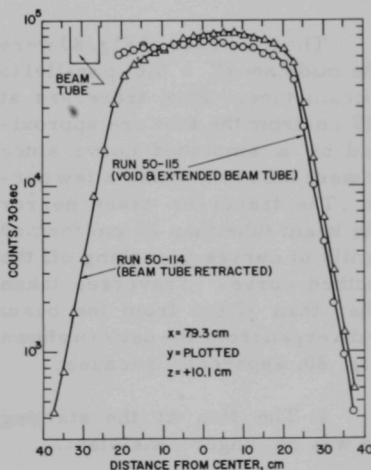
Figures 74, 75, and 77 show traverses taken before installation of the aluminum shroud sector, and the effect of this 45.7 x 45.7 by 20.3-cm-thick aluminum slab is shown by the curves of Figs. 78 and 79 labeled Run 50-114.

Figures 78 and 79 also show the effect of extending and partially voiding the through tube to provide a 10.1 x 10.1-cm-square tangential beam tube. A convenient aspect of the traverse at $x = 79.3$ cm is the flat (within a few percent) portion extending from the beam tube to about 37 cm away. This made it feasible to plot Fig. 80 as a family of curves starting at approximately the same flux level, when traversing in the x direction rather than the y direction.



112-8983 Rev. 1

Fig. 77. Traverses before Installation of Aluminum Shroud



112-8986

Fig. 78. Close-in Effect of Extending Beam Tube

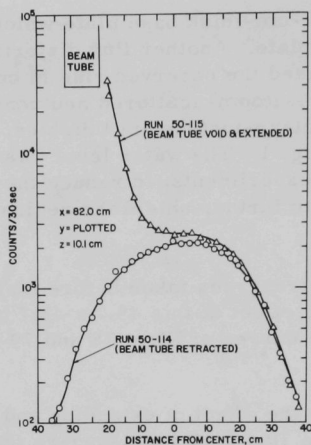


Fig. 79
Effect of Extending Beam Tube

112-8984 Rev. 1

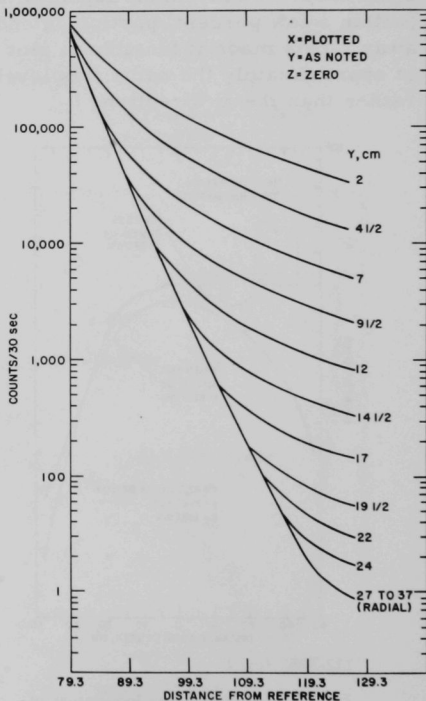
The traverses of Fig. 79 ($x = 82$ cm) indicate that the beam tube is a major source of the neutrons detected in this vicinity. The perturbation is noticeable in this traverse as far as approximately 40 cm from the beam tube.

The traverses of Fig. 80 were in the midplane ($Z = 0.0$) parallel to the beam tube. Five traverses at 27-37 cm from the tube are approximated by a smoothed curve since they were the same within a few percent. The traverses taken nearer to the beam tube than 27 cm formed a family of curves branching off the smoothed curve. Traverses taken farther than 37 cm from the beam tube diverged from the pattern shown in Fig. 80, apparently because:

1. The flux at the starting point was no longer consistent.

2. The traverse direction was noticeably off the radial direction.

3. The edge of the aluminum slab was near enough to affect the flux distribution in that direction.



112-8998 Rev. 1

Fig. 80. Traverses Parallel to Extended Beam Tube in Midplane

The data presented here are sufficient for estimation of flux perturbations around beam tubes of the geometry tested. Because of the strong dependence on details of geometry, the results shown here should be used with caution in relating to other situations.

VIII. BEAM-TUBE YIELDS, REACTIVITY REQUIREMENTS, AND INTERACTIONS

A. Introduction

The horizontal beam tubes of AARR were planned to extract thermal-energy neutrons from the beryllium radial reflector. The epithermal and fast-neutron energy components of the emerging beam are generally objectionable and should be minimized to avoid radiation damage and competing reactions in samples. The fast flux also causes high background levels, which require added shielding in the vicinity of experimental equipment. Consequently, the thermal-neutron yields of the beam tubes should be maximized, but the relative epithermal and fast yields should be minimized insofar as is feasible. Section XI.D shows the results of measurements of the fast-neutron distribution from a beam tube.

The reactivity loss from beam-tube installation was measured, to assist in estimating the core composition of AARR which would provide the desired reactivity margins. Differential measurements were made which indicate the relationship between beam-tube yields and reactivity requirements. The reactivity effect of flooding beam tubes with water was measured to aid in estimation of the safety hazard inherent in accidental flooding. The interaction of adjacent beam tubes was also measured in terms of the effect on their yields.

B. Yield and Reactivity Measurements with Horizontal Beam Tube

1. Description of Beam Tubes

The 10.16-cm (outside dimensions) square beam tubes were manufactured for slip fit in the beryllium reflector, which consisted of closely packed beryllium blocks sized in 5.08-cm modules. The beam tubes were formed by bending and welding 0.318-cm (1/8-in.) thick aluminum sheet stock. The four corners were formed by bending to ~0.3-cm (inside) radius. The welded edges formed a seam centered along one side of each tube. The weld beads were dressed down, even with the surfaces of the aluminum. One end of each radial tube was closed by welding an 0.318-cm-thick aluminum plate into the end of the tube.

Flanged ends were welded to the open ends of the beam tubes, and watertight closures were provided by the use of O-rings between the removable end caps and the welded flanges. Standpipes, or risers, were threaded into some of the end caps for entrance of control wiring, cords, radiation-detector cables, etc. Extra sections were provided which were used to lengthen the beam tubes as necessary, without the difficulty of replacing the entire tube.

The beryllium fillers installed in the beam tubes were assembled from available pieces, leaving fairly large clearances, of necessity. The fillers amounted to $\sim 81\%$ of the volume of beryllium removed in installing the 10.16-cm-square beam tubes. Thus, within the beryllium reflector region the beam tubes could be filled to the extent that 81% of their volume was beryllium, 12% was the aluminum making up the tube walls, and $\sim 7\%$ was void. During some experiments requiring repositioning of the filler in the through tube, an additional strip of aluminum was often inserted underneath the beryllium filler for attachment to a remote-controlled drive motor.

The 15.2-cm (6-in.) square beam tubes were of similar construction to that of the 10.16-cm tubes.

Figure 81 shows the initial locations of the 10.16-cm (4-in.) square beam tubes.

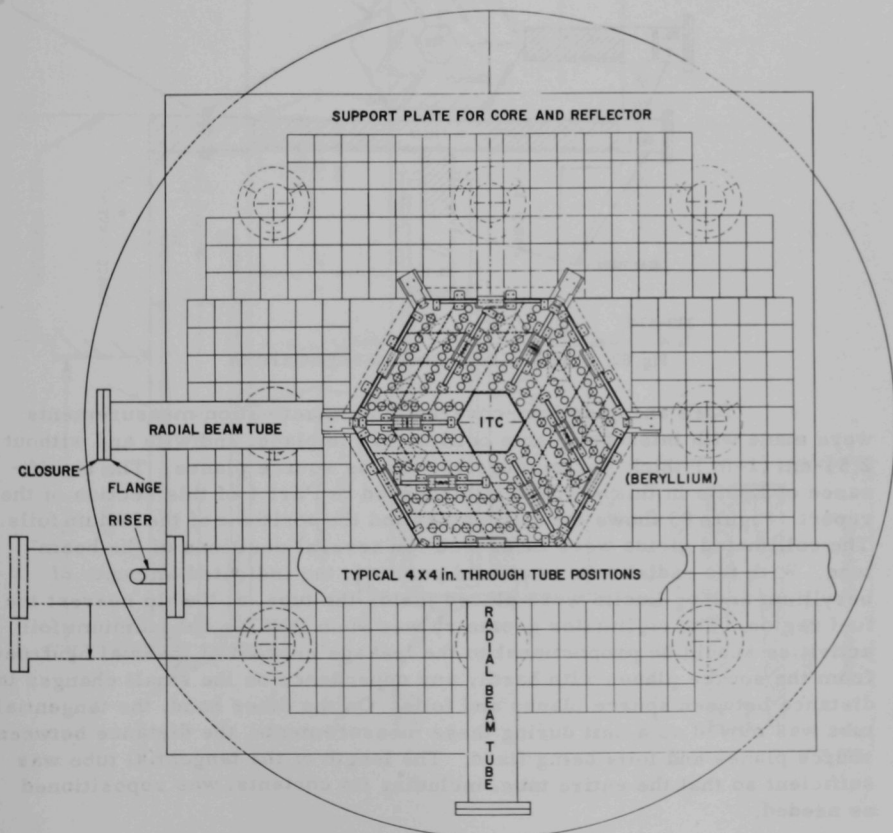
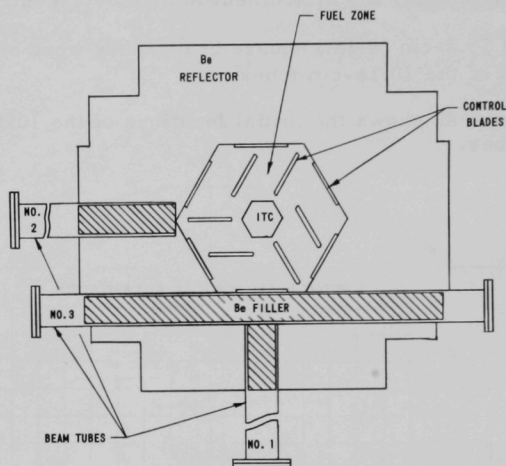


Fig. 81. Initial Installation of Beam Tubes

2. Foil Activation Measurements in Beam Tubes

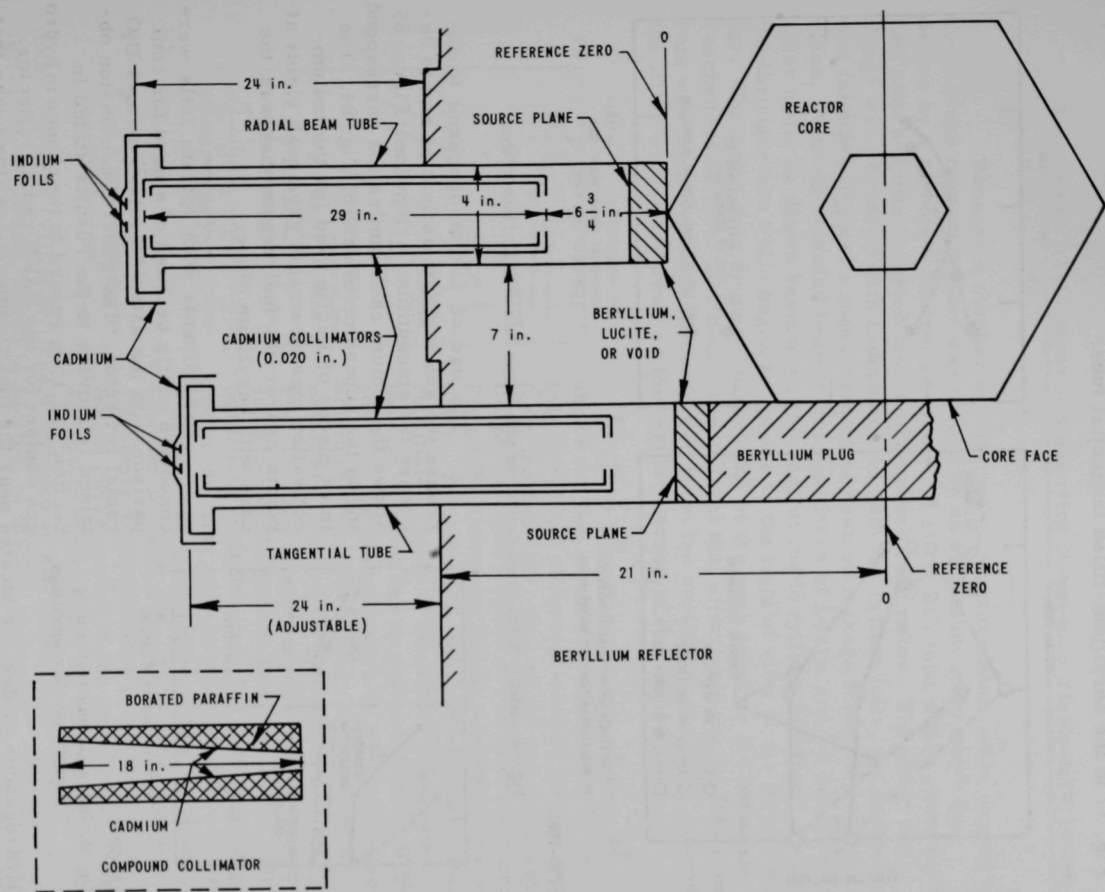
Several activation traverses were made to indicate the effect of beam tubes on the radial flux distribution, when the beam tubes are voided or filled with beryllium. These traverses were taken in Assembly 3 and were discussed in Section V.C.4, with foil locations as shown in Figs. 33 and 34, and traverses in Figs. 35-37. Figure 82 shows the beryllium filler locations during these measurements.



112-5748

Fig. 82. Positions of Beam Tubes and Beryllium Fillers

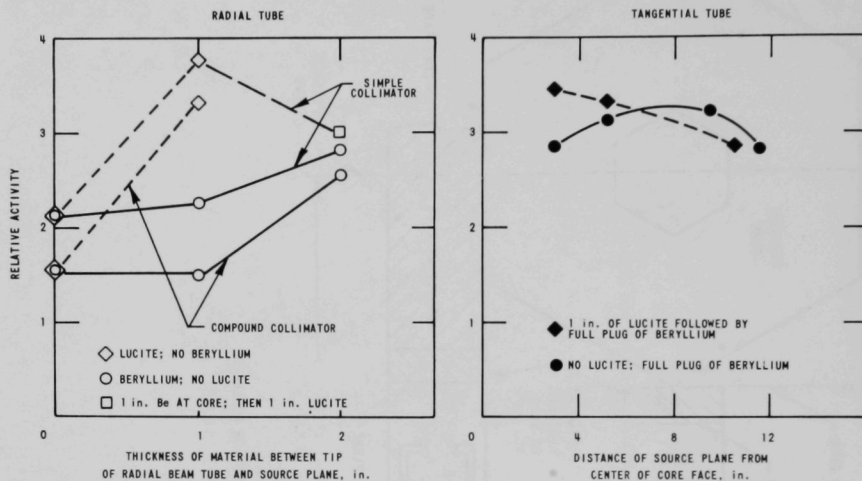
Bare and cadmium-covered indium activation measurements were made with interchangeable collimators in place, and with and without 2.54-cm (1-in.) thick Lucite plugs serving as source planes. The significance of Lucite in this position is discussed in Part 4 of this section of the report. Figure 83 shows the collimators and the positions of the indium foils. The collimated yields were measured for several positions of the beam tube. With the radial tube in a fixed position, the indicated amounts of beryllium and/or Lucite were placed inside the tube, at the tip nearest the fuel region. The collimator geometry was such that the subcadmium foil activities should be proportional to the leakage current of thermal neutrons from the source planes with hardly any dependence on the small changes in distance between source planes and foils. On the other hand, the tangential tube was moved as a unit during these measurements, the distance between source planes and foils being fixed. The length of the tangential tube was sufficient so that the entire tube, including its contents, was repositioned as needed.



112-6888

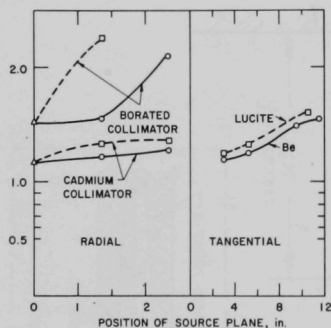
Fig. 83. Arrangements of Beam Tubes and Collimators

Figure 84 shows the subcadmium indium activations. A broad peak was obtained in the tangential beam tube when beryllium alone was used as filler. That peak is at the same position as the reflector peak shown by Fig. 37 in the beryllium-filled tangential tube.



113-1283

Fig. 84. Relative Subcadmium Activations with Indium Foils at Ends of Beam Tubes



113-1226

Fig. 85. Indium Cadmium Ratios Using Different Beam Tube Geometries

The use of Lucite appeared to increase the subcadmium activation and to decrease the epicadmium activation. Figure 85 shows the indium cadmium ratios corresponding to the subcadmium data of Fig. 84. The thick pieces of Lucite used for the indium-activation measurements gave peak yields at points nearer the fuel region than was the case with beryllium alone.

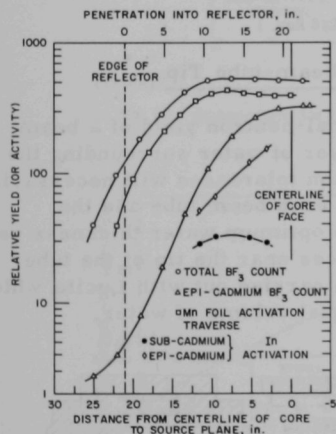
Experiments with indium foils were conducted partly because of a need for comparison with the data of Kouts,²³ using a D₂O radial reflector. The general conclusion obtained is similar to the results stated in Section V.C.1, in regard to the change in hydrogen content for the AARR radial reflector.

Hydrogenous moderator located near the fuel region causes flux peaks that are sharper and more intense than in materials such as beryllium or heavy

water. The reactivity loss accompanying flux peaking in a radial reflector region is somewhat more position-dependent than in the ITC; however, the qualitative arguments are the same as in Section IV.D.

3. Use of BF_3 Counter in Measuring Beam-tube Yields in 10.16-cm-sq Beam Tubes

Because a number of differential measurements were needed in the through tube, the filler was placed on an aluminum strip which was driven by a remotely controlled motor. A short BF_3 tube with a preamplifier attached was inserted into the compound collimator. The riser and flange were covered with cadmium. As with the indium foils, the geometry was intended to yield a measurement of neutron leakage from the source plane. With an extended beam tube, the blocks of Lucite and/or beryllium filler could be drawn beyond the far edge of the beryllium reflector, so that the through-tube walls began to appear in the field of view of the BF_3 detector. The count rate dropped to about 8% of the peak level as the material reached its farthest position. It is thought that effectively all the BF_3 count rate was from neutrons that emerged from the surface of the filler, unless the filler was as far away as the farther corner of the fuel region.



112-6139

Fig. 86. Tangential Beam Tube: Relative Yield vs Penetration into Beryllium Reflector

The uppermost curve of Fig. 86 shows the BF_3 count rate taken as a 12-in.-long beryllium filler was shifted farther away from the detector, thus effectively deepening the penetration into the beryllium reflector. Figure 87 shows the initial position of the filler. This curve is thought to indicate the collimated yields of tangential beam tubes, the tips of which are positioned at the indicated points. The second curve is the manganese activation traverse of Fig. 37, taken with beryllium filler in the position indicated by Fig. 82. The manganese traverse is representative of the flux distribution in the solid beryllium reflector, and the similarity between the first and second curves is readily evident. The third curve of Fig. 86 is the epicadmium BF_3 count rate. This has a strikingly different slope from that of the fourth curve, which is the epicadmium indium activation obtained during the foil-activation

measurements (VIII.B.2). The difference is attributed to the resonance activation of indium, which is additive to the $1/v$ activation. The lowest curve shown in Fig. 86 is the corresponding curve from Fig. 84 for subcadmium indium activation. The agreement is satisfactory between subcadmium indium activation and subcadmium BF_3 count rate (not shown).

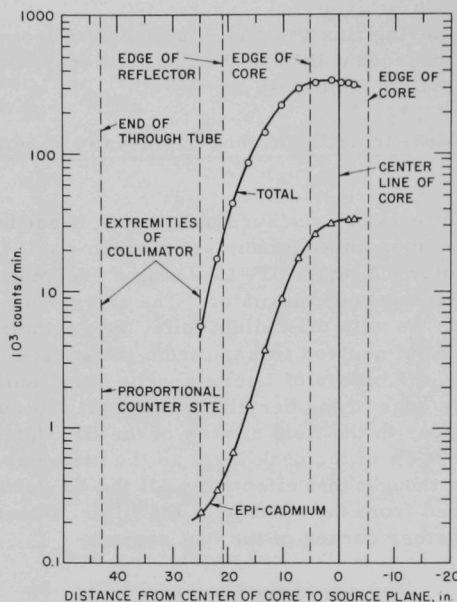


Fig. 87

Tangential Beam Tube: Relative Yield vs Penetration, into Reflector with Lucite Tip

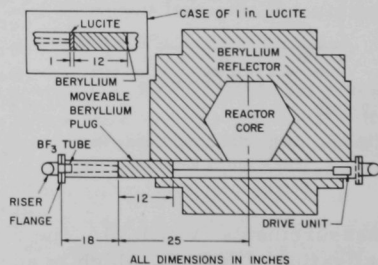
113-1286 Rev. 1

4. Experiments with Plastic Slabs at Beam-tube Tip

It had been predicted that the thermal-neutron yield of a beam tube would be enhanced by the presence of a layer of water surrounding the tip inside the beryllium reflector.²⁴ Construction tolerances will necessarily result in a variable water-filled space between each beam tube and the beryllium, and it is necessary to determine the optimum water thickness as well as the precision required in fixing tolerances near the tip of the tube. Experiments in the horizontal beam tubes were carried out with Lucite, which contained about 84% as much hydrogen as an equal volume of water.

Figure 87 indicates the BF_3 count rate with a 2.5-cm (1-in.) thickness of Lucite and 30.5 cm (12 in.) of beryllium filler combined as shown by Fig. 88 (inset portion). These traverses indicate a higher cadmium ratio and also a significant longitudinal displacement relative to the curves obtained with the beryllium filler alone.

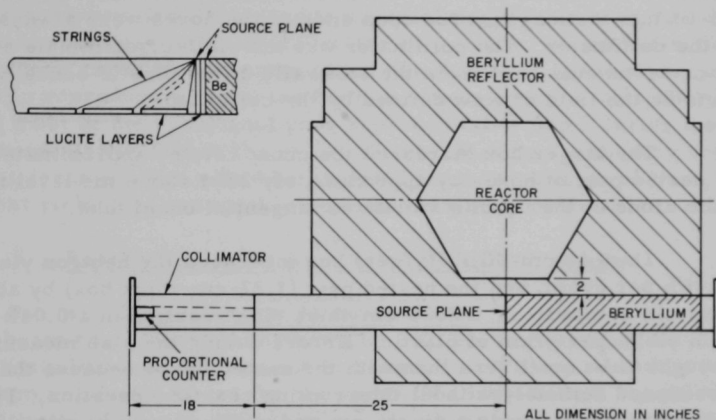
With the BF_3 counter and the compound collimator described in Section 3 above, and a number of Lucite



113-1288 Rev. 1

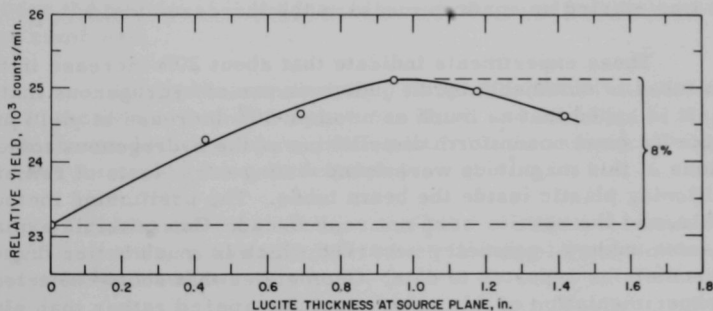
Fig. 88. Initial Configuration for Relative Yield Measurements

plates as indicated by Fig. 89, the BF_3 count rate was recorded as a function of Lucite slab thickness. The experiment involved repetitively reading the BF_3 count rate as cumulative thicknesses of Lucite were raised into the field viewed through the collimator. The resulting yield curve is given in Fig. 90, which shows a maximum of about 8% improvement in yield with a 2.5-cm (1-in.) thickness of Lucite.



112-8817

Fig. 89. Arrangement for Measuring Yields, with Lucite at the Tip of a Beam Tube



112-8890 Rev. 1

Fig. 90. Relative Neutron Yield as a Function of Lucite Slab Thickness

Since AARR beam tubes will be rounded off at the tip, the surrounding water space will be dished rather than slab-shaped. A crude test of dished geometry was carried out by inserting one and both of a pair of nested plastic boxes into the beam tube in place of the slabs indicated by Fig. 89. The larger box was 9.2 x 9.2 x 9.2 cm (outside dimensions) with one side left open. The walls were made of 0.63-cm (1/4-in.) thick Plexiglas or Lucite. The smaller box was of similar construction and was dimensioned for slip-fit into the larger. The open ends of the boxes were always turned toward the collimator. The collimator was known to discriminate strongly against neutrons scattered from the sidewalls of the plastic boxes, which were outside the field of view defined by the collimator.

The larger box increased the count rate by approximately 16%, and the nested pair of boxes by approximately 22%, above the level found with beryllium alone at the tip of a simulated tangential beam tube.

The 0.63-cm-thick (larger) box increased the neutron yield by about 0.06% per gram, and the nested pair (1.27-cm-thick box) by about 0.05% per gram. In comparison, a 1.09-cm-thick slab resulted in a 0.04% increase in yield, per gram of plastic. Errors during the slab measurements were thought to be much less than with the nested boxes because the slabs were positioned remotely without interrupting reactor operation. Typical slab data were taken during a single run and within a span of about 2 hr, during which only minor reactivity adjustments were necessary because of the worths of the plastic pieces that were moved about. On the other hand, it was necessary to take a reference run before loading a box. Following this, the reactor was shut down, the box was inserted in the beam tube, and the reactor was started up again to measure the increased yield.

These experiments indicate that about 20% increase in the yields of beam tubes is obtainable by the judicious use of hydrogenous material at the tip. It is hoped that as much as another 30% increase in yield might be obtainable by some nonuniform distribution of the hydrogenous material. Indications of this magnitude were found during early tests of remote methods for positioning plastic inside the beam tubes. The positioning methods were unreliable, and the results were not reproduced. One possible explanation is that some unknown geometry occurred which is much better than those known geometries reported to date. Geometries that should be tried in any future experimentation of this nature include tapered rather than slab-shaped plastic liners and particularly should provide arrangements permitting use of different thicknesses of plastic along different sides of the beam tube. The plastic slabs resting on the bottom of the beam tube (as shown by Fig. 89) do not affect yields significantly until raised into upright positions. This suggests that the vertical walls of the plastic boxes may be the effective portions, and that the horizontal walls may be much less effective than the vertical walls.

The maximum yield with the plastic boxes at the tip of the beam tube occurred with about 4 cm deeper penetration into the beryllium reflector than with the plastic slabs.

Numerous improvements were suggested in regard to the work with horizontal beam tubes. The suitability of plastic in simulating water was tested in a vertical beam tube as described in Section VIII.C. For greater accuracy, the hydrogenous material might have been outside rather than inside the beam tube. Because the BF_3 counter preamplifier failed during these experiments, some of the data had to be discarded. Small errors in reproducing geometry from one measurement to another may have caused most of the occasional poor reproducibility found during the yield measurements. If this is the cause, then beam-tube design may require closer tolerances than would be expected from the data given here, to ensure that yields are reasonably near the maximum obtainable.

5. Reactivity Losses Associated with Beam Tubes

a. Integral-worth Measurements. The installation of three empty beam tubes, located as shown by Fig. 82, in Assembly No. 3 caused a reactivity loss of 1.3%. Insertion of beryllium filler, restoring 81% of the beryllium volume removed for the beam-tube installation, recovered 1.0% in reactivity. This was almost proportional to the volumes involved. However, removal of the fillers from one beam tube at a time gave losses of 0.08, 0.2, and 0.6% sequentially for beam tubes No. 1, 2, and 3 in Fig. 82. Since tube No. 2 was far enough removed from tubes No. 1 and 3 to be free of interactions, it appears that interaction between tubes No. 1 and 3 must account for the failure of individual filler worths to add up to the worth of all three combined.

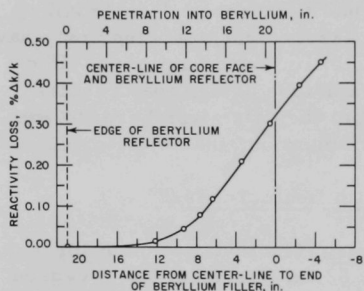
Rough measurements in Assembly 4a indicated that the combined reactivity worth of empty tubes No. 2 and 3 in Fig. 82 was about 0.78%, which was not significantly different from the individual worths measured in Assembly 3 for those tubes.

Measurement of the same tube worths in Assembly 5 gave a combined reactivity worth of 0.52%, which is roughly two-thirds as great as in Assemblies 3 and 4a.

Installation of a single large through tube 15.2 x 15.2 cm (6 x 6 in.) in cross section in Assembly 5, adjacent to the fuel zone as shown for tube 3, reduced reactivity by 1.14%. The reactivity ratio between the empty large and small through tubes was estimated to be 2.7, compared to a volume ratio of 2.3, when the tubes were installed adjacent to the fuel zone. Insertion of beryllium filler into the large through tube recovered $0.98 \pm 0.006\%$ in reactivity, which again is nearly proportional to the volume of beryllium restored. This reactivity measurement was incidental to other

experiments. The filler volume was estimated to be about 88% of the volume of beryllium removed during installation of the large through tube.

A crude measurement of the reactivity of the large radial through tube was obtained when the tube was repositioned so that 10.16 cm of beryllium was between the tube and the fuel region. The worth was measured to be $0.28 \pm 0.05\%$; however, the reference conditions were somewhat obscured by a preceding temperature-coefficient measurement, and the $\pm 0.05\%$ range of error may be questionable.



112-6140 Rev. 1

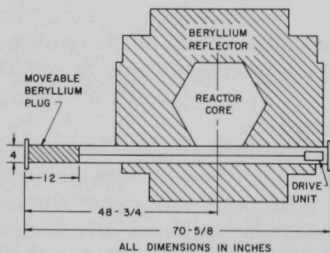
Fig. 91. Reactivity Loss vs Depth of Beam-tube Penetration into Beryllium Reflector

b. Differential-worth Measurements.

Measurements were made in the 10.16-cm-square beam tubes to indicate the spatial-reactivity effects of various fillers. Most of the incremental measurements were made in Assembly 3 using the through-tube positions indicated by Fig. 82 or 92. Figure 91 shows the reactivity loss as the normal beryllium filler of the through tube (shown by Fig. 82 as tube No. 3) was withdrawn toward one end. The integral worth of this filler was measured at 0.6%. The more accurate incremental measurements shown by Fig. 91 reach about 0.31 or 0.32% for the half-withdrawn filler. This indicated little or no asymmetry and is consistent with measurements in the vertical direction which indicate that interactions from void regions are hardly detectable at distances greater than 10 cm away from 10 x 10-cm beam tube. The interactions extend much farther in the radial direction, as shown in Chapter VII, and in Section E of this chapter.

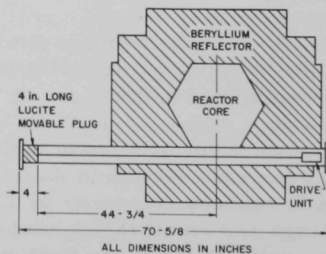
Figure 94 or 95 shows the reactivity effects of traversing a 30.5-cm-long beryllium plug or a 10.16-cm-long plastic plug along the empty through tube starting with the geometry shown by Fig. 92 or 93. The

Figure 94 or 95 shows the reactivity effects of traversing a 30.5-cm-long beryllium plug or a 10.16-cm-long plastic plug along the empty through tube starting with the geometry shown by Fig. 92 or 93. The



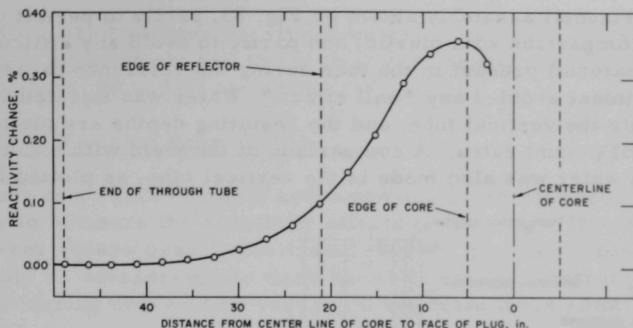
113-1224

Fig. 92. Through-tube Configuration for Measuring Reactivity Worth of 12-in.-long Beryllium Plug



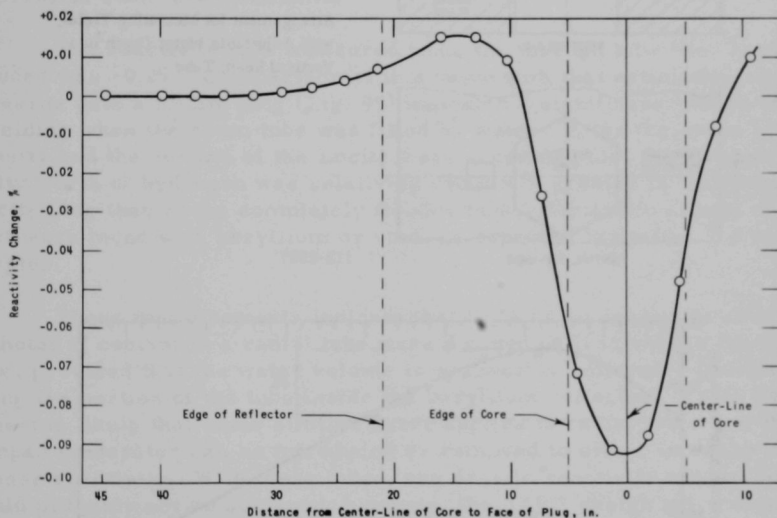
113-1225

Fig. 93. Through-tube Configuration for Measuring Reactivity Worth of 4-in.-long Lucite Plug



113-1586 Rev. 1

Fig. 94. Reactivity Worth of 12-in.-long Beryllium Plug along Through Tube



112-7351 Rev. 1

Fig. 95. Reactivity Effect of 4-in.-long Lucite Insert in Through Tube

points shown would have been plotted 6 or 2 in. to the right if the plots were for the positions of the centers rather than the left-hand faces of the plugs as shown.

C. Experiments with a Vertical Beam Tube

Experiments were performed in a vertical beam tube positioned as indicated by Fig. 96. The vertical tube was used to confirm results obtained

with the horizontal assembly shown by Fig. 85, partly to permit use of water for comparison with plastic, and partly to avoid any difficulty with unneeded material present in the tube during the reference measurement. This experiment avoided any "wall effect." Water was injected incrementally into the vertical tube, and the resulting depths are plotted against measured BF_3 count rates. A comparison of the yield with a Lucite slab rather than water was also made in the vertical tube, as plotted in Fig. 97.

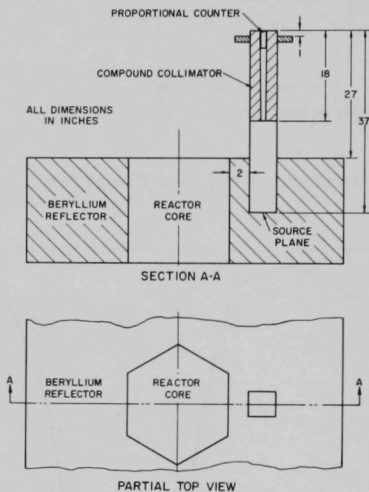
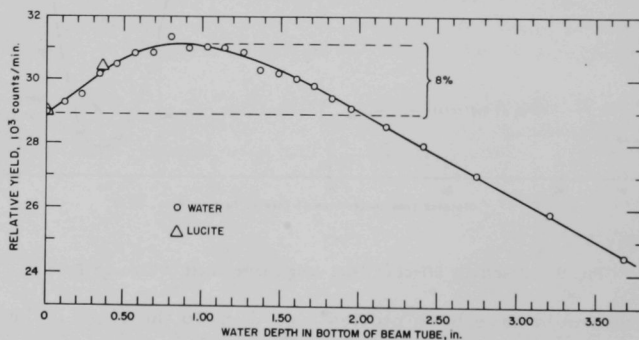


Fig. 96

Arrangement for Measuring Yields,
with Adjustable Water Depth in a
Vertical Beam Tube

112-8887



112-8821 Rev. 1

Fig. 97. Relative Neutron Yield as a Function of Lucite or Water
Thickness in a Vertical Beam Tube

Within the accuracy of the measurement, Lucite duplicated the effect of water, although it was expected that the measured point would fall below rather than above the line because of the lower hydrogen density in

Lucite (84% of the hydrogen density of water). The peaks of the curves appear to be of equal height and to occur at very nearly the same thickness of material if Figs. 90 and 97 are compared.

D. Effects of Flooding Beam Tubes

Fear of a reactivity gain accompanying beam-tube leakage made it necessary to measure the reactivity effects of flooding. This was done with the 10.16-cm-square beam tubes installed in the positions shown by Fig. 82, in Assembly 3. Measurements were based on critical control-blade configurations during consecutive runs, with the beam tubes empty or flooded with water.

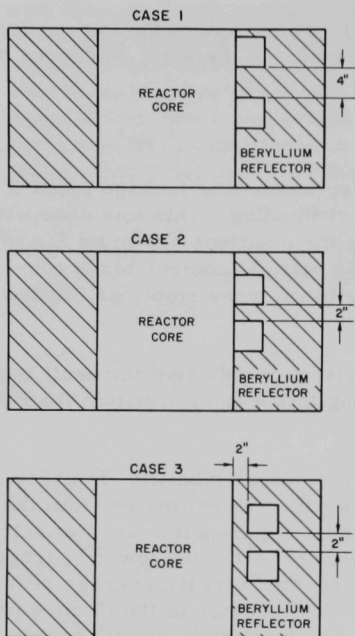
Although a very slight gain in reactivity was indicated to result from flooding radial tube No. 2, the amount was negligible and fell within the range of error of such measurements.

The reactivity loss measured when the through tube (No. 3) was flooded was -0.2%. Comparison of this value with that estimated from the traverse with a Lucite plug (Fig. 95) indicated a significant amount of self-shielding when the beam tube was filled by water. After the lower hydrogen density and the volume of the Lucite were accounted for, the average reactivity worth of hydrogen was relatively about 50% greater in the 10-cm-square Lucite plug than in the completely flooded tube. Negligible effects of this sort were found with beryllium or void, as reported in Section B.5 of this chapter.

These measurements indicate that little or no reactivity effect would be noted if coolant in a radial tube were drained or if inleakage filled the tube, provided that the water volume is reasonably uniformly distributed along the portion of the tube inside the beryllium reflector. From Fig. 95, it seems likely that some similar curve applies to radial tubes and that lumped moderator can be introduced or removed to either increase or decrease reactivity. With these tubes, any drastic reactivity change result could probably not be achieved; however, the AARR design may not have placed beam tubes close enough to the fuel region so that any of the negative portion of Fig. 95 will apply.

E. Beam-tube Interaction Experiments

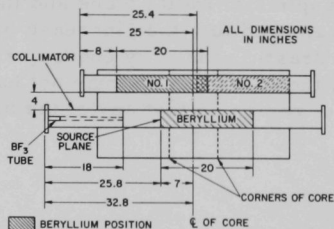
The interactions between beam tubes were measured typically by moving a beryllium filler plug along a through tube, simulating the installation of a tangential tube in the beryllium reflector. The yield from a second tube was measured using a collimated BF_3 detector to determine any detectable change in yield caused by movement of the filler. The filler had only 81% as large cross-sectional area as the opening required for installation of each tube in the beryllium reflector. The interactions are likely to have been



113-1569

Fig. 98. Cross Section of Beam Tubes and Reflector Used in Interaction Measurements

in yield were measured. Cases 1 and 2 represent typical tangential beam-tube arrangements, and Case 3 represents typical through-tube interaction.



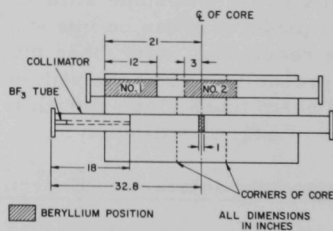
113-1590

Fig. 99. Configurations of Beam-tube Contents in Vertical Interaction Measurements, Cases 1 and 2

underestimated by this procedure, because of the physical limitations on the size of the filler. On the other hand, one purpose of these experiments was to determine the separation necessary to reduce interactions to a negligible level, which appears to have been accomplished.

Interactions were measured between parallel beam tubes separated vertically by 5.08 and 10.16 cm (2 and 4 in.) of beryllium as indicated by Fig. 98 for three separate arrangements labeled Cases 1, 2, and 3. Figures 99 and 100 show the positions of the fillers. Yield measurements were always made in the tube nearest the mid-plane, and different results might have been obtained if the yields of the upper tube had been measured. The movable filler was repositioned without shutting down the reactor.

In Case 1, with 10.16-cm vertical separation, no detectable change in yield was measured as a result of moving the beryllium filler incrementally from position 1 through position 2 in the upper tube. In Case 2, as much as 14% decrease, and in Case 3, as much as a 9% decrease



113-1583

Fig. 100. Configurations of Beam-tube Contents in Vertical Interaction Measurement, Case 3

Using the arrangement indicated by Fig. 101, we measured the effect of fillers in the through tube on yields of a radial tube positioned in the same horizontal plane. A 30.5-cm (12-in.) long beryllium filler plug was traversed along the through tube. The conditions of the radial tube were:

1. Void, yielding the highest peak in BF_3 count rate shown by Fig. 102.
2. With 7.6 cm (3 in.) of beryllium in the tip, yielding the next highest peak in BF_3 count rate shown.
3. With 10.16 cm (4 in.) of beryllium in the tip, showing about 11% increase in count rate as the movable beryllium block was centered.
4. With 7.6 cm (3 in.) of beryllium plus 2.5 cm (1 in.) of Lucite facing the collimator.

The fourth condition resulted in significantly reduced BF_3 count rate when the movable beryllium block was centered.

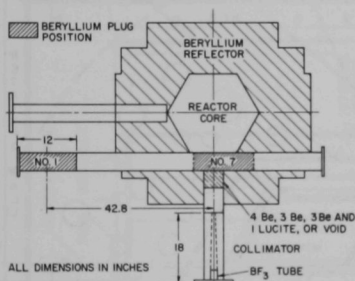
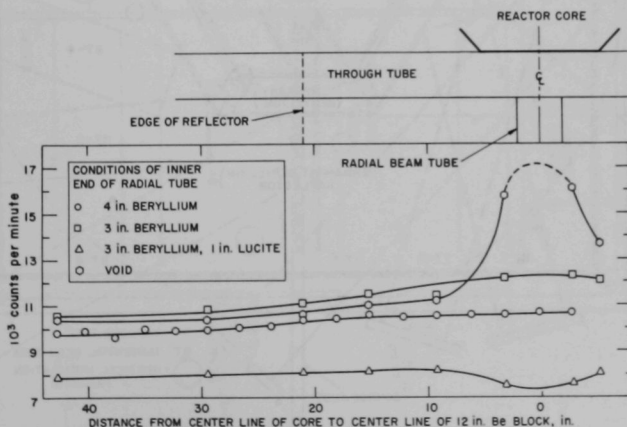


Fig. 101
Configurations of Beam-tube Contents
in Radial Interaction Measurement

113-1589

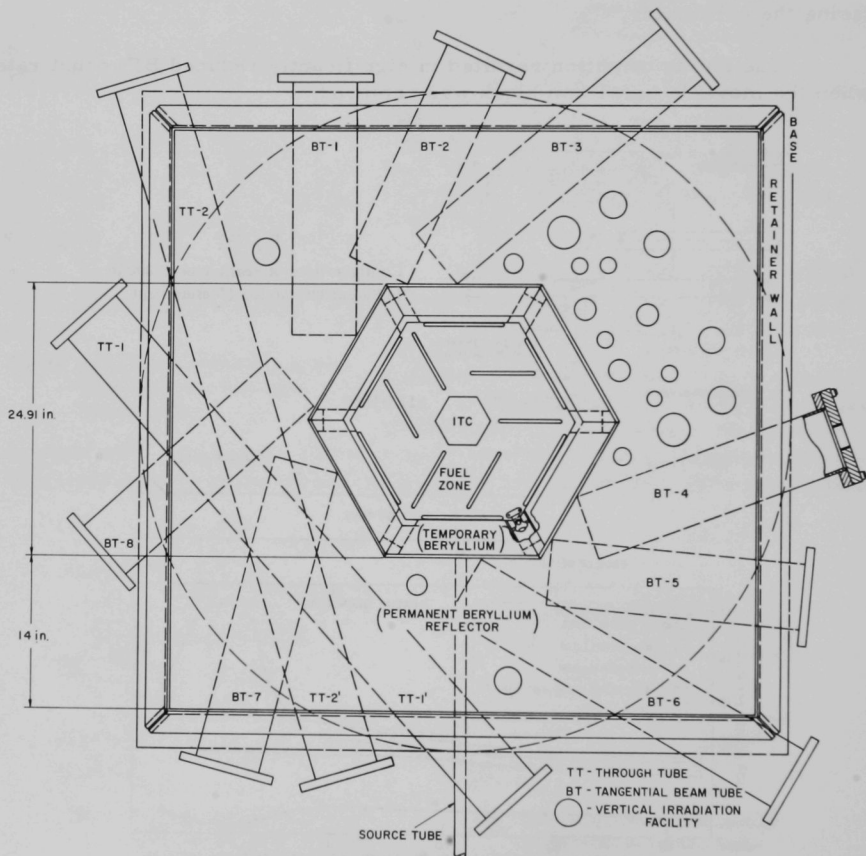


113-1571 Rev. 1

Fig. 102. Measurement of Radial Interaction between Beam Tubes

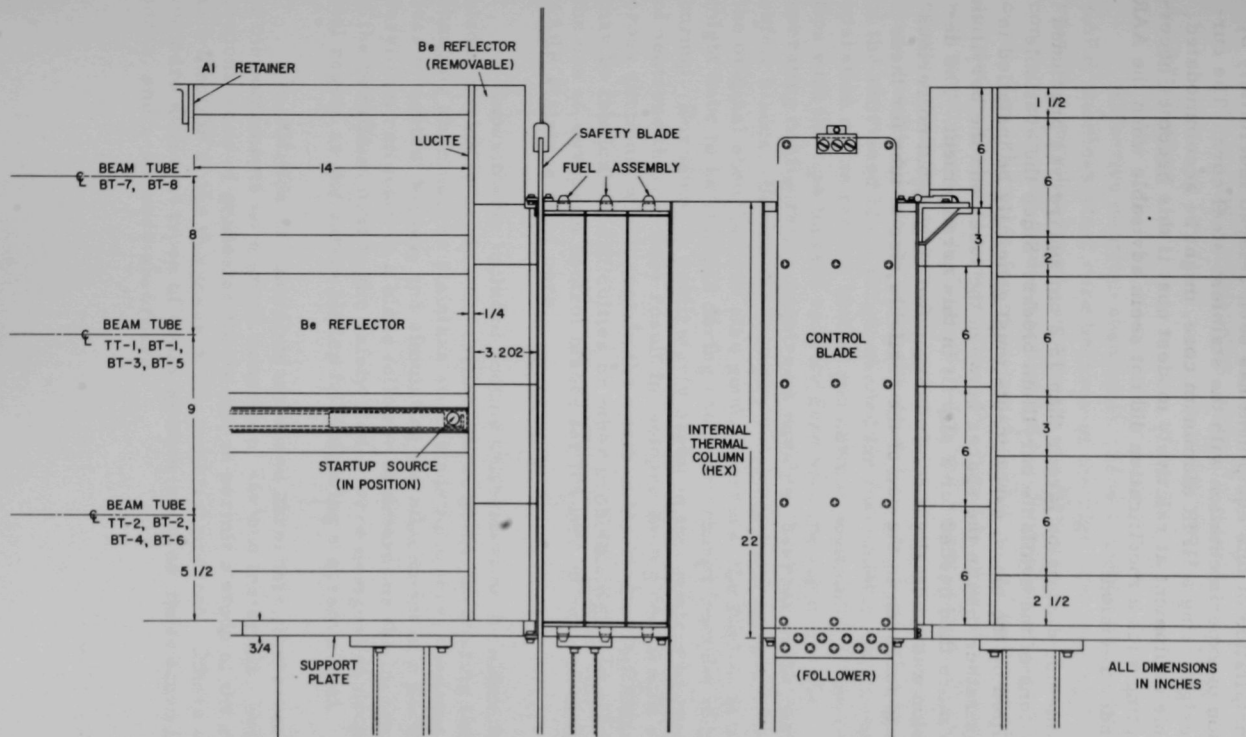
F. Status of Equipment Obtained for Future Experiments

The long lead time necessary for the preparation of a beryllium reflector that would accommodate a large number of beam tubes required the design and fabrication of a new reflector and a complete assortment of beam tubes while experimentation was still in progress using the old equipment discussed in Sections A-E above. Figures 103 and 104 show the new reflector and beam-tube arrangements. Two horizontal through tubes and up to eight horizontal, tangential beam tubes were provided, each 15.2 cm square. Nineteen vertical irradiation tubes were included, complete with screw tips which would fasten to the base plate to preclude displacement by buoyancy in the surrounding water.



112-9106 Rev. 1

Fig. 103. Plan View of Proposed Radial Reflector and Beam Tubes



112-9105

Fig. 104. Elevation View of Proposed Radial Reflector and Beam Tubes

The installation of this equipment has been delayed indefinitely by the termination of experimentation with the stainless steel core. The current AARR design, using a HFIR aluminum core, might be accommodated by the available equipment at relatively modest cost if this becomes necessary. Attempting such a modification did not seem advisable when the AARR design was under revision.

A beam-tube dimension larger than 15.2 cm square was precluded by the dimensions of the available beryllium blocks. Since the available spaces are filled by the tubes, experiments must generally be installed inside the tubes rather than in the spaces between the tubes and the beryllium, which are no more than needed for a slip fit in this arrangement. The desired dimension was nominally a centimeter or two larger, but no serious complication is foreseen in the use of the available size of tube for these experiments.

IX. EXPERIMENTS WITH CONTROL AND SAFETY BLADES, VARIOUS ABSORBERS, AND ^{235}U ALUMINUM COUPONS

A. Introduction

Effective neutron-absorption cross sections are quite small in the AARR stainless steel core because of the high fuel-loading density and the resulting very hardened neutron-energy distribution. The dimensions of control and safety blades are limited by the compact nature of a high-flux core. Thus the selection of materials and dimensions of control blades and safety blades is very restricted. Rapid burnup of absorber materials will result from the high-flux level in the AARR core and from a proposed operating configuration. An operating configuration of control and safety blades which results in quick shutdown following a scram signal, because of the shortened blade travel needed for maximum effect, involves banked operation of the control blades and normal positioning of the safety-blade tips with the tips located roughly even with the top of the fuel. Such an operating configuration requires a durable absorber in the control and safety blades. Unless the isotopes resulting from capture of neutrons by the original absorber are also good absorbers, the control and safety blades might have to be changed during each core change because of localized burnup. Europium is particularly useful in this respect because the capture of neutrons therein does result in isotopes having reasonable absorption cross sections, which sustain the worth of the blade. Unfortunately, there may be fabrication difficulties or other problems which would determine the use of europium control blades for the type of service involved in the AARR stainless steel core.

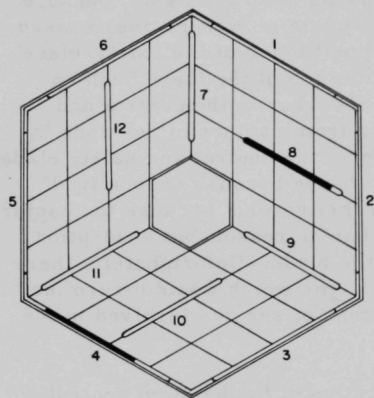
Experiments included routine calibration of the hafnium control blades normally used in the critical experiment, measuring the effects of changing aluminum to stainless steel blade followers, changing the thickness of control blades, and simulating the attachment of a portion of the beryllium reflector to a blade follower to determine the increased worth if the beryllium next to the safety blades were designed to drop below the fuel region as the safety blades fall following a scram signal.

In addition to control-blade-sized absorbers, there were a number of measurements with small coupons of various materials. Some of the coupons were of graduated thickness, to permit a study of the relative worth as a function of the thickness of the material present. Others were used to compare different types of cross section such as those found in cadmium, boron, and resonance absorbers.

B. Calibrations of Standard Hafnium Control and Safety Blades

1. Standard Blade Dimensions and Locations

The set of 12 hafnium blades originally obtained for the critical experiment consists of single sheets of hafnium 0.381 ± 0.013 cm (0.150 ± 0.005 in.) thick, except where joined to the follower. The joint was below the fuel region when the blade was fully inserted. The lower 3.81 cm (1.5 in.) of each hafnium sheet was cut to 0.127-cm (0.05-in.) thickness, and attached by screws to a 0.254-cm (0.10-in.) thick tongue of the blade follower. The tongue of the follower was sandwiched between the 0.127-cm-thick hafnium part and an equal thickness of stainless steel, which makes up the remainder of the 0.508-cm (0.20-in.) thick standard blade.



112-6841

Fig. 105. Diagram Showing Blade Numbers and Special Control-blade Orientations 4a and 8a

The control/safety-blade positions are designated by number as shown in Fig. 105; any two or more up to six were used as safeties. The six safety-blade slots as designated by AARR design are numbered 1 through 6, and the control-blade positions are numbered 7 through 12. The slots all have a thickness of 0.63 cm (0.25 in.). The orientation of fuel plates alongside the various positions affected the blade worths, so that the odd-numbered positions were slightly dissimilar from the even-numbered positions. The control blades are 15.2 cm (6 in.) wide; the safety blades are 19 cm (7.5 in.) wide. Thus, blades 1, 3, and 5 are positioned alike and have the same dimensions. Blades 2, 4, and 6 are positioned alike and have the same dimensions as 1, 3 and 5, but do not have the same arrangement of fuel in their vicinities. Blades 7,

9, and 11 and blades 8, 10, and 12 make up other sets of three, but are not as wide as blades 1 through 6. The blade suspension is indicated by the sectional view of the critical assembly, shown in Fig. 2.

As a matter of perhaps minor interest, the initial plan had been to use cadmium sheets instead of the 0.127-cm-thick stainless steel portions of the control blades. The stainless steel was substituted because of fear of binding between cadmium and the blade guides, because cadmium did not appear in the AARR design, and because the worths were adequate without the addition of cadmium in the critical assembly. The stainless steel was desirable for its mechanical strength, and this avoided any hazard of breakage. No cracks or other flaws have developed in the hafnium, and breakage is not considered likely with the material provided.

2. Shadowing of Blade Worths

The blade calibrations varied significantly because of shadowing by adjacent blades, if inserted. Because the excess reactivity was different with different core loadings (given in Table I), the number of control/safety blades inserted at criticality varied from loading to loading, and shadowing was sometimes encountered during calibration measurements. Assembly 1 had only 0.4% excess reactivity; consequently shadowing by control/safety elements normally was not detected. Shadowing effects were negligible in Assemblies 3 and 4a, which had less than 3% excess reactivity, because it was feasible to perform calibrations with as few as three blades inserted (separated 120° azimuthally around the core) during calibration runs. No significant shadowing was detected between blades separated 120° azimuthally around the core.

The amount of shadowing obtainable in Assembly 4b was measured. Using unshadowed blade-calibration curves, we could vary the critical configuration from 3.0 to 4.26% indicated excess reactivity. Since the core loading was unaffected by the blade configuration, it was concluded that the excess reactivity remained constant at 3.0% and that shadowing reduced the blade worths to as little as 0.7 of the unshadowed value, with blades 4, 5, and 11 fully inserted and blade 12 controlling at 45.35 cm withdrawn, which is 37.6 cm above the bottom of the fuel. Table XXVII summarizes the data taken during the shadowing measurement. Note that blade 11 was a "thin" blade at the time of this experiment, as described in Section C.1 below.

TABLE XXVII. Shadowing Data for Control Blades of Assembly 4b

Configuration No.	Blades Fully Inserted	Blades Partially Inserted	Indicated ^a Excess Reactivity, %	Measured Shadow Factors ^b
1	No. 10 and 12	No. 8 at 21.67 cm	2.996	1.000
2	No. 10 and 12	No. 11 at 14.43 cm	3.302	0.907
3	No. 4, 5, and 11	No. 12 at 37.60 cm	4.264	0.703

^aExcess reactivity indicated by unshadowed blade-calibration curves (obtained with blades separated 120° azimuthally).

^bRatio of excess reactivity to indicated excess reactivity.

Shadowing appears to be more pronounced with combinations of in-core and peripheral blades than with in-core or peripheral blades exclusively. The greatest shadowing indicated by Table XXVII is with the third configuration, which included two peripheral blades. Banked in-core blade worths were more nearly equal to the sum of the individual worths. A shadowing factor of 0.95 was found for banked peripheral blades in Assembly 5. Interactions affecting adjacent peripheral blades were also noted in the experiments with beryllium reflector removal, simulating attachment of a 5.08-cm-thick portion of reflector to a blade follower (see Section G below).

The worths of the peripheral blades should be affected by flux tilting to a greater extent than those of the in-core blades. Consequently, flux tilting is probably a major factor in the shadowing experiments. Another factor is the more hardened neutron-energy spectrum at the in-core positions than in the vicinity of the reflector, which suggests that thermal-flux depressions are greatest at the peripheral-blade locations.

3. Worths of Standard Hafnium Blades with Aluminum Followers

The usual selection of follower material for a hafnium blade is zirconium, which can be welded to hafnium. As a convenient substitute, aluminum followers were used instead of zirconium in the critical experiments. Calibrations were obtained in each of the assemblies loaded, for at least one of the control- or safety-blade groups. Accuracy of calibration was least with Assembly 1, because the calibration was necessarily by sub-critical methods and the stated results could be in error by $\pm 0.1\%$. Typical errors in rising period calibrations were estimated at $\pm 0.005\%$ in reactivity resulting from ± 1 -sec errors in determining each rising period, using plots from two or three instruments. Assuming seven rising periods, and random errors, for each blade calibrated, resulted in a standard error estimate of $\pm 0.013\%$ per blade, although about three times as large an error results from assuming cumulative systematic errors.

For three groups of blades in Assembly 1 and two groups in Assembly 2, only the critical configurations were measured. This established the ranks of the groups quite accurately, but the individual worths could not be estimated accurately because of the small excess reactivity. Only a short length of one blade was necessary to control the small excess reactivity, and the comparison of one blade with another by proportionality involved a number of difficulties inherent in early operation. Position indication and up and down limit positions were unsettled because of transmitter-shaft slippage, snubber adjustments, and blade-guide tolerances. In Assembly 2, two blades were fully inserted at criticality, and comparison was reasonably accurate. Table XXVIII gives the calibration data for the standard-dimension blades. Although the blades are listed by groups of three, there

TABLE XXVIII. Standard Control-blade Worths,
Using Aluminum Followers

Blade No.	Reactivity (%) by Assembly Numbers					
	1	2a	3	4a	4b	5
1, 3, 5	$\sim 1.2^a$	1.46 ^a	1.30	1.12	1.44	1.23
2, 4, 6	$\sim 1.3^a$	1.52	1.43	1.20	1.51	1.21
7, 9, 11	$\sim 1.5^a$	1.58 ^a	1.25	1.01	1.14	Varies
8, 10, 12	1.8 ± 0.1	1.66	1.41	1.07	1.18	1.20

^aThese worths were estimated from critical configurations and are not as accurate as worths measured by rising periods. The ranks are correct. (See discussion in text.)

were also some small differences within each group, which are not shown. The individual differences were attributed to clearances and other dimensional variations.

4. Conclusions

Generally, the worths of the blades positioned inside the fuel region decreased monotonically with increased fuel-loading density (Assemblies 1, 2a, 3, and 4a). The worths of the six peripheral blades were slightly less affected by fuel-loading density. Since the peripheral blades were 25% wider than the interior blades, the worth per unit area was fairly independent of location in Assemblies 4a and 4b.

The average unit worths per square centimeter of extent of 0.381-cm-thick hafnium (with or without an additional 0.127-cm thickness of stainless steel) ranged from 0.0013 to 0.0026% reactivity. (Effective dimensions assumed were widths of 15.24 and 19.05 cm and a length of 45.72 cm.) This range is about a tenth as great as that of absorber in the ITC, which is indicated by Tables X, XI, and XII and Figs. 9 and 10.

Comparison of worths in Assemblies 4a and 4b, involving primarily the change from the small to the large ITC, showed that the worths of peripheral blades were affected (increased) by a factor of 1.275 ± 0.02 while the worths of the in-core blades were affected by a factor of 1.115 ± 0.015 .

Comparison of worths in Assemblies 4b and 5, involving primarily the change to a graded fuel loading, indicated a factor of 0.82 ± 0.03 (decrease) in individual peripheral-blade worths. Worths of individual and banked in-core blades were typically changed by a factor of 0.95 ± 0.05 . These reductions in worth are contrary to the trend with uniform loadings where removal of fuel and boron would cause an increase in control/safety-blade worth. The peripheral-blade worths were affected (reduced) by a factor of 0.95 when banked, as compared to individual worths, in Assembly 5. The banked worths of the in-core blades are discussed under Section E.3.

C. Reactivity Worths of Thin Hafnium Blades

1. Description of Thin Blades

The thin hafnium blades were composed of the same 0.381-cm-thick pieces of hafnium used in the standard blades. The 0.127-cm-thick stainless steel portions present on the standard blades were removed, and the blade followers were changed to 0.381-cm thicknesses of aluminum, in making up the thin blades. These blades were normally used as safety blades after the change.

2. Purpose of the Thin-blade Experiments

Four thin blades were made up first for use as safety blades for the critical experiment. Two were in-core type (15.24 cm wide), and two were peripheral type (19.05 cm wide). The decreased thickness of the thin blades resulted in a thicker water gap between the blades (or the followers) and the fuel region. The increased clearance was needed because of a slight tendency of the fuel elements surrounding the blade slots to close in on the blades during temperature-coefficient experiments. A particular instance, including swelling of a jacketed fuel plate, had resulted in a stuck blade. Swelling of the stationary nylon guides that keep the blades in alignment was the major cause of friction on the blades during temperature-coefficient runs, and this condition was relieved by readjustment to leave space for expansion of nylon with increasing temperature.

At that time, the AARR design was being modified to allow greater clearance around the blades, and the thin blades in the critical experiment provided a similar increase in clearance. Consequently, further experiments were performed with the thin blades to determine what reactivity differences resulted from their installation. Flux measurements were also made to determine the magnitude of flux peaking in the fuel region adjoining the thickened water gaps, as described in Section V.E.

3. Comparison of Thin and Standard Blades

As shown by Table XXIX, the thin blades were, with only one exception, worth less than the standard blades when installed in the peripheral positions. Conversely, the thin blades were worth more than the standard blades when installed in the in-core positions where the neutron spectrum was very hardened. The thin blades were available only during Assemblies 3, 4a, 4b, and 5. Because of impending termination of the program, the calibrations were not carried out in as great detail in Assemblies 4b and 5 as was done earlier.

TABLE XXIX. Comparison of Worths of Thin and Standard Blades

Type Blade: Blade No.	Reactivity (%) by Assembly Numbers							
	3		4a		4b		5	
	Thin	Standard	Thin	Standard	Thin	Standard	Thin	Standard
1, 3, 5	1.20	1.30	1.11	1.12		1.44		1.23
2, 4, 6	1.29	1.43	1.20	1.20	1.18	1.51	0.93	1.21
7, 9, 11	1.31	1.25	1.04	1.01	1.22	1.14		
8, 10, 12	1.46	1.41	1.14	1.07		1.18		1.20

D. Reactivity Worths of Thick Hafnium Blades

1. Purpose of Measurement

Since hafnium control and safety blades generally are not clad, but europium blades would require roughly a 0.01- or 0.02-cm (or thicker) stainless steel cladding, it was desired to determine how significant a change in thickness of hafnium might be, for comparison with europium. Earlier in-core measurements with small coupons had indicated a reactivity effect less than a factor of 1.1 for an increase in thickness of hafnium from 0.38 to 0.51 cm. The hafnium data with small coupons are given in Section J below. The europium data are reported in Sections I and J below.

2. Description of Thick Blades

One peripheral thin hafnium blade (19.05 cm wide and 0.381 cm thick) was thickened by attaching a ~0.127-cm-thick hafnium sheet to it, and changing to a 0.508-cm-thick standard aluminum follower. Thus, the thickened blade included a full 0.508-cm thickness of hafnium, except at the joint with the aluminum follower. The joint was below the fuel region when the blade was fully inserted. Although the overall thickness of the blade was the same as that of a standard blade, it was all hafnium, whereas a 0.127-cm thickness of stainless steel was included in each standard blade.

The thickness of the added sheet of hafnium varied from 0.127 to 0.140 cm, except for areas totaling about 3 sq in., which had been ground down to remove surface flaws. These were scattered areas produced during rolling in fabrication and extended lengthwise along the blade. The minimum thickness in these areas was 0.10 cm.

3. Comparison of Thick and Standard Peripheral Blades in Assembly 4b

Comparisons were made in two peripheral positions, using thick and standard hafnium blades in Assembly 4b. In position No. 2, the worths were 1.509 and 1.449% in reactivity, or a factor of 1.04 in reactivity for an increase of a third in hafnium thickness. The results for position No. 6 were 1.426 and 1.331%, respectively, or a factor of 1.07. These values were obtained by rod-drop techniques, using an on-line computer for data analysis. Typical blade configurations during these experiments were with No. 2 or 6 inserted and No. 4 withdrawn 22-27 cm.

More accurate measurements of the differences in worth were obtained by measuring the changes in critical configurations of No. 4 calibrated control blade. These results were 0.084 and 0.090%, as compared to 0.060 and 0.095% by the rod-drop method. These differences indicated increases by factors of 1.058 and 1.068 in reactivity because of the increase in thickness, for peripheral positions 2 and 6, respectively.

E. Dependence of Worths of Standard Hafnium Blades on Temperature and on ITC Void Fraction

1. General Nature of Dependence

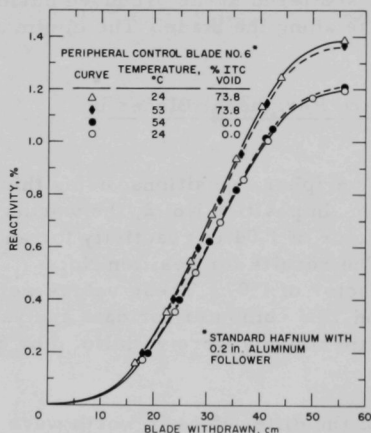
Control-blade worths probably affected the measurements of temperature coefficients in all the measurements attempted. Thus, the apparent temperature coefficient consisted of (1) a loss in reactivity as the system was warmed (except below $\sim 40^\circ\text{C}$, where the coefficient was not necessarily negative) and (2) a change in the worth of any control/safety blade inserted for operation of the facility. To retain criticality, both factors required blade motion, and the apparent coefficient was usually more negative than indicated by water-level control with all blades withdrawn from the reactor. The difference was not necessarily obvious in a temperature-coefficient measurement in Assembly 2 (see Fig. 113 later), which was hampered by a number of problems resulting in data scatter. The measurement with Assembly 3 was with better equipment and procedures, and a recalibration of blade No. 6 indicated 3.3% relatively greater worth at 53°C than at 24°C .

A massive void experiment in the ITC during Assembly 3 was with blade No. 12 fully inserted and blade No. 8 controlling. The blade worth at room temperature was the same whether the ITC was flooded with water or 73.8% voided. The blade worths were remeasured at 50 – 70°C and shown to have decreased by about 7% relatively when the ITC was voided, but increased 3% above the room-temperature worth when the ITC was flooded.

Thus, by the time Assembly 4a was available, it had become apparent that ITC void fraction and reactor temperature could affect blade worths significantly.

2. Calibrations of Blades No. 6 and 10 in Assembly 4a

Detailed calibrations were made of blades No. 6 and 10 in Assembly 4a. The plotted worths of blade No. 6 are shown in Fig. 106. The worth of the blade increased by about 15%, relatively, as a consequence of voiding the ITC by 73.8% at 24°C . Similar results were obtained with in-core blade No. 10. The calibrations of blade No. 6 at $\sim 54^\circ\text{C}$ were significantly affected by both temperature and voiding. The blade worth without void was relatively 1.3% greater at 54°C than at room temperature, but the worth with void in the ITC was 1.8% less at 54°C than



112-7458 Rev. 2

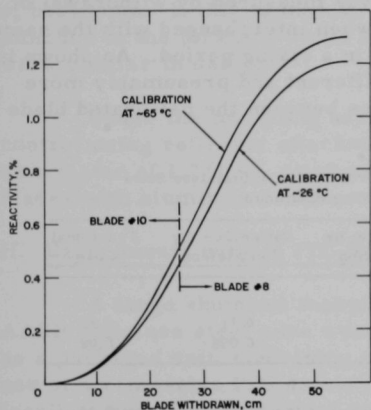
Fig. 106. Calibrations of Blade No. 6 with Different Temperatures and ITC Void Fractions in Assembly 4a

at room temperature, which was similar to the results with Assembly 3. The effect of voiding was much greater than that of temperature on the worth of blades No. 6 and 10. This was the opposite of the results in Assembly 3.

3. Calibration of Banked Blades 7-12 in Assembly 5

During a temperature coefficient test, in Assembly 5, critical water-height measurements and blade calibrations did not agree, as shown by Fig. 116 later. This experiment was with a banked configuration of blades No. 7-12, which matched the expected AARR operating configuration insofar as was feasible. Calibrations of blades No. 8 and 10 were carried out by rising-period measurement at ~ 26 and $\sim 65^\circ\text{C}$. Blade No. 8 was withdrawn incrementally, for each rising-period determination, and blade No. 10 was then used to compensate. Both started from the banked configurations, and blade No. 12 was used to supplement blade No. 10 when fully inserted.

These blade worths were 7% greater, relatively, at 65°C than at $\sim 26^\circ\text{C}$. These data are plotted in Fig. 107. The midplane of the core is at 30.6 cm on the scale of Fig. 107. The change in blade worth accounted for more than half the blade withdrawal during the temperature-coefficient measurement. Because the excess reactivity of AARR will change during the core life, the blade configuration will vary. This variation will affect the apparent temperature coefficient of the system. Shutdown margins generally would be greater when the system is hot than when it is cool.



112-8820

Fig. 107. Blade Worths at 26 and 65°C in Assembly 5

4. Conclusions

Changes in blade worths were large enough to complicate measurements of temperature coefficients and of massive ITC void worths. There were no measurements in which the combined effects of increased temperature and voiding reduced

blade worths below those measured at room temperature with no void in the ITC. The nature of the results obtained was not anticipated during Assemblies 1 and 2, and no obvious pattern has been found to rationalize the results.

F. Comparison of Aluminum and Stainless Steel Blade Followers

1. Purpose of Comparison

An aluminum follower absorbs fewer neutrons than does a stainless steel follower of the same size and in the same position. Thus a blade

followed by aluminum increases reactivity to a greater extent, as it is withdrawn, than if it is followed by stainless steel. However, one purpose of a follower is to prevent undue flux peaking in the blade slot when the blade is withdrawn, and stainless steel is more effective than aluminum in this respect.

Comparison of the two types of followers included reactivity measurements as well as flux plots. The flux measurements are given in Section V.E.

2. Measured Loss of Reactivity-control Worth on Substitution of Stainless Steel for Aluminum Blade Followers

The aluminum followers of blades No. 2 and 7 or 4 and 8 were replaced by stainless steel, and the blades were recalibrated giving the worths shown in Table XXX. In addition to recalibration, blades No. 2 and 7 were compared to No. 6 and 9, respectively, by interchange in Assembly 3. After the aluminum followers were replaced, the interchange was repeated and the difference in reactivity controlled was measured by withdrawal of blade No. 6 (or No. 9) to the level attained when interchanged with the same blade followed by stainless steel, resulting in a rising period. As shown in Table XXX, the comparison gave slightly different and presumably more accurate results than obtained by differences between the calibrated blade worths.

TABLE XXX. Loss of Reactivity-control Worth by Use of Stainless Steel Control-blade Followers, Replacing Aluminum

Blade No.	Worth with Al Follower, %	Worth with SS Follower, %	Difference, by Calibration	Difference, by Comparison	Fractional Loss
Assembly 3					
2	1.43	1.01	0.42	0.31	0.22
7	1.25	1.16	0.09	0.098	0.08
Assembly 4a					
4	1.19	0.91	0.28	-	0.24
8	1.07	1.02	0.05	-	0.05

The reactivity worths of stainless steel followers in the peripheral positions, No. 2 and 4, were sufficient that stainless steel followers may not be feasible for AARR safety blades. The in-core positions, No. 7 and 8, were in a region having a more hardened neutron-energy spectrum where the difference in effective cross sections of aluminum and stainless steel was not as great as at the periphery.

G. Measurements Related to Attachment of Beryllium Reflector to Safety-blade Follower

A proposed AARR safety device involved attachment of sections of beryllium reflector to the followers of the peripheral (safety) blades. Rather

than construct a detailed mockup, for testing the device, we removed a 5.1-cm-thick slab of beryllium reflector blocks alongside safety blade No. 3. This allowed a measurement corresponding roughly to attachment of a sixth of the temporary beryllium reflector to a safety-blade follower. However, a two-step procedure was needed. The critical configurations were measured first with the beryllium in place and safety blade No. 3 driven all out, and then all in. The procedure was repeated with the 5.1 x 25.4 x 48.3-cm beryllium slab removed, and the space filled with water.

The loss of reactivity attributed to beryllium removal was $1.8 \pm 0.2\%$. Recalibration of safety blade No. 3 by rising periods indicated a worth of -0.54%, compared to -1.44% initially. Since the width of the blade is only three-fourths of the width of the beryllium removed, a combination with beryllium would yield $(0.54 + 0.75 \times 1.8) = 1.9\%$, which is 1.31 times the worth of the safety blade with beryllium remaining in the reflector.

During review of the data, it was noted that both adjacent peripheral blades were somewhat shadowed (by about 0.1% in reactivity) after removal of beryllium. If this is mutual, the worth of a safety blade with beryllium attached to the follower would be reduced to 1.7% if the neighboring blades were similar in design.

Under the foregoing assumption of mutual shadowing, the reactivity control using reflector attachment to six safety-blade followers appears to be a factor of 1.7/1.44, or about 1.18, times the worth of six hafnium safety blades with aluminum followers.

H. Experiments with an ITC Safety-liner Mockup

A large shutdown margin would be needed during shipment if an AARR stainless steel core were to be received and loaded into the reactor as a packaged unit, containing about 60 kg of highly enriched uranium. The use of a removable ITC safety liner for increased shutdown margin appeared feasible, and a measurement was made of the reactivity worth of a mockup in Assembly 5, which included the ITC of Fig. 6. Although a thick, heavily absorbing liner would otherwise have been tested, the available supply of hafnium was limited to an 0.13-cm-thick liner, which was sufficient to replace the 0.16-cm-thick stainless steel wall of the small ITC or 80% of the perimeter of the large ITC. Since there were consistent thickness data from tests with small coupons and from safety-blade experiments, it seemed reasonable to measure the worth of the thin hafnium liner and to use that measurement as a basis for an estimate of the worth of a thick one. Another factor was that the excess reactivity of the available Assembly 5 equaled the anticipated worth of the thin liner; thus this experiment would not require reloading of the reactor. A thicker liner would require either reloading or resort to subcritical measurements, which are not very accurate.

After a reference run, the six 6.0-cm-wide, 0.16-cm-thick stainless steel sides of the large ITC were replaced by 0.13-cm-thick hafnium, but the re-entrant corners were not changed. This resulted in 80% of the ITC perimeter being hafnium, and 20% being stainless steel. This partial ITC liner controlled 3.16% reactivity, as measured by control-blade calibration based on rising periods, in the reference condition.

Cadmium sheet, 0.093 cm thick, was shaped to fit the re-entrant corners and was then inserted between the ITC and the adjacent fuel. The composite ITC liner controlled 3.93% in reactivity. The reactivity ratio between the cadmium portion and the hafnium portion of the ITC liner was $0.77/3.16 = 0.24$, as compared with the area ratio $0.20/0.80 = 0.25$. Since the cadmium was fitted into corners, its geometry was less favorable than that of the hafnium, and this measurement underestimated cadmium worth, relative to hafnium. Compared to the nearest control blades, of 0.38-cm-thick hafnium, the 0.13-cm-thick hafnium in the ITC liner was 1.13 times as effective per unit area.

Judging by the hafnium coupon data, one would expect a thick hafnium ITC liner to control up to twice as much reactivity as the thin liner. There are other factors to be considered, however. In the preceding sections, discussing the partial removal of beryllium radial reflector, and shadowing of adjacent blades, it was shown that control-blade calibrations could be affected at some distance from the location of a heavy absorber. A precise measurement of ITC liner worth would be possible only with mockups of the shipping and loading arrangements. The interaction between components is too great to obtain accurate indications of subcriticality during shipping without such a mockup.

I. Experiments with Europium Control-blade Specimen

1. Purpose

The use of europia-stainless steel blades in the AARR stainless steel core was studied as a means of obtaining greater control capability. The following reactor-physics considerations favored the use of europium. The thermal, epithermal, and resonance cross sections of a europium blade are greater than those of alternative materials. The isotopes resulting from neutron capture by the two stable isotopes of europium are long-lived and also have large neutron-absorption cross sections, which delay the effects of burnout. Thus a europium control blade might be expected to last much longer than a blade made of other materials, if burnup were the limiting factor.

As noted in Section F above, a major complication of a europia-stainless steel blade is a stainless steel follower, which absorbs more reactivity than aluminum in the peripheral positions near the beryllium

reflector. Thus the initial reactivity advantage of europium is cancelled. In the in-core positions, where the neutron-flux distribution is more hardened, the difference in effective neutron-absorption cross sections of various followers is much less, and consequently the europia-stainless steel blade is more effective, there, than is hafnium with an aluminum follower.

These europia-stainless steel specimens were tested only to the extent required for reactivity measurements and were not subjected to the normal stress, shock, and wear inherent in use as control elements. One specimen was cracked across nearly 90% of its width, to the extent that light passed through. The crack might have resulted from fabrication, mechanical testing, or shipping accidents. The additional precautions required with that specimen resulted in only one set of measurements of its worth. Although no deterioration was found when these specimens were used in the critical experiment, the fact that they were temporarily installed there should not be taken as evidence that such material is mechanically suitable for use in the dimensions provided. Noticeable variations were found in the reactivity worths of these specimens which also indicated dependence on fabrication process.

2. Description of Europia-Stainless Steel Plates

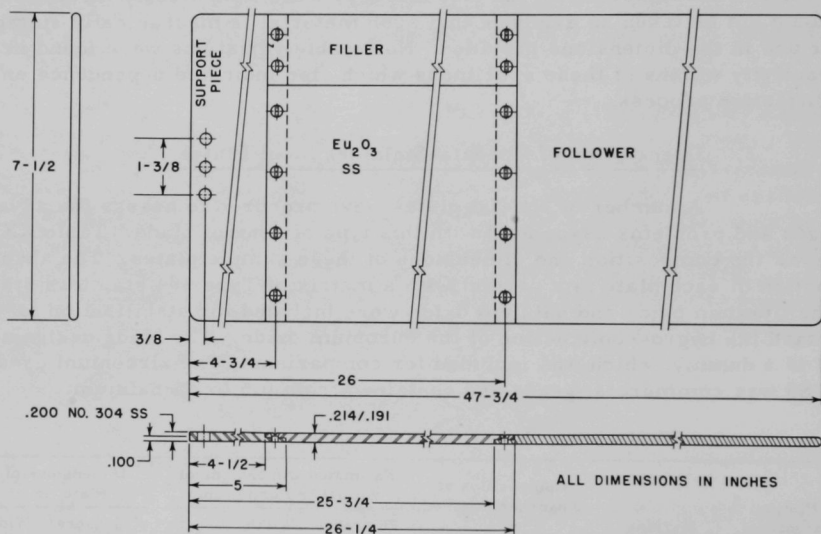
A number of special plates were procured to assess the advantages and problems associated with this type of control blade. Table XXXI shows the composition and dimensions of these sample plates. The absorber portion of each plate is a cermet with a matrix of Type 304 stainless steel. The titanium oxide and hafnium oxide were included for stabilization to retard the hygroscopic action of the europium oxide. The blade designated S3 is a dummy, which was included for comparison. The zirconium used in S3 was commercial grade and contained from 0.5 to 2% hafnium.

TABLE XXXI. Descriptions of Special Control-blade Plates

Plate Designation	Marking	Composition of Absorber Portion, w/o	Estimated Dimensions of Absorber Portion, in.			Dimensions of Plate, in.	
			Thickness	Width	Length	Thickness	Width
S1	ZGS-I	34.3 Eu ₂ O ₃ 15.6 TiO ₂ 50.1 SS	0.182	5.175	18 $\frac{1}{2}$	0.213-0.215	5.75
S2	ANL-50%	27.4 Eu ₂ O ₃ 12.4 TiO ₂ 60.2 SS	0.167	5.300	18 $\frac{1}{2}$	0.194-0.198	5.75
S3	ZGP-I	50.7 ZrO ₂ 49.3 SS	0.171	5.135	18 $\frac{1}{2}$	0.204-0.206	5.75
M1	Unmarked	28.8 Eu ₂ O ₃ 13.0 TiO ₂ 58.2 SS	0.18	5.35	18 $\frac{1}{2}$	0.209-0.211	5.59
M2	Unmarked and cracked	17.7 Eu ₂ O ₃ 21.2 HfO ₂ 61.1 SS	0.18	5.26	18	0.203-0.210	5.49

The plates listed in Table XXXI were framed and clad with stainless steel. The compositions and estimated dimensions of the absorber portions were obtained from the fabricators.

These special plates were used to make standard-size control blades for the AARR critical facility. Figure 108 shows in detail the assembly used for a peripheral control-blade position. For an in-core position, the overall blade width is 6 in. instead of the $7\frac{1}{2}$ in. shown in Fig. 108. The support pieces, followers, and fillers were Type 304 stainless steel. The plates were all machined to $21\frac{3}{4}$ in. overall length. However, as shown in Table XXXI, the widths of the plates were not the same. Fillers of various sizes had to be made to match the different plate widths. The assembled europia-stainless steel control blades had the same overall dimensions as the standard hafnium blades.



112-5683 Rev. 1

Fig. 108. Europa-Stainless Steel Blade Assembly

3. Measured Worths of Samples

Each special blade was calibrated in control-blade positions No. 4 and 8. Also, since the plates were narrower than the hafnium control blades, each blade was calibrated twice, with the blade rotated 180° in the control-blade slot after the first calibration. Table XXXII lists the total worths obtained from these calibrations in cores 3 and 4a. The estimated uncertainty in these tabulated values is $\pm 0.02\%$ in reactivity, except for blade S3 where the uncertainty is estimated to be $\pm 0.005\%$ in reactivity.

Figure 105 is a diagram of the core, showing the 45 rhombic fuel assemblies and the 12 control-blade locations. The shaded areas in control-blade slots No. 4 and 8 represent the positions of the absorbing regions of the special control blades when they were in the 4a and 8a orientations. Table XXXII indicates that, within the accuracy of the measurements, the blade worth is independent of orientation.

TABLE XXXII. Total Worths of Special Control Blades

Blade Designation	Measured Reactivity Control Worths, %							
	Assembly 3				Assembly 4a			
	In-core Blade		Peripheral Blade		In-core Blade		Peripheral Blade	
	8a	8b	4a	4b	8a	8b	4a	4b
S1	1.13	1.14	0.88	0.87	1.00	1.00	0.80	0.82
S2	1.15	1.11	0.89	0.93	0.99	0.97	0.80	0.82
S3	0.023	0.022	-0.024	-0.025	0.030	0.022	-0.017	-0.025
M1	1.15	1.15	0.89	0.87	1.03	1.02	0.82	0.81
M2	1.08	1.07	0.83	0.84				

The negative values shown for blade S3 indicate that in the peripheral position, when the zirconia portion of the blade was withdrawn from the core, there was a resultant loss of reactivity.

No data were taken for blade M2 in core 4. This blade was worth less in core 3 than the other europia blades, and the condition of the blade was such that continued use in an operating reactor was not considered advisable.

Direct comparison of the total worth of these special blades with each other and with the standard hafnium blades is misleading because of the differences in the dimensions of the active portions of the blades. To obtain a useful comparison, the measured values have been adjusted in several ways. To eliminate the effect due to different active lengths, the worth of each blade was determined from an equivalent full-out position to a position where the bottom of the active region is at the midplane of the core. For the hafnium blades, the worth was obtained for the portion from 12.30 in. out to 22.05 in. out. An equivalent change in the europia blade position was obtained by using the portion from 10.30 in. out to 20.05 in. out. A survey of previous hafnium-blade calibrations shows that the range from 12.30 to 22.05 in. represents about 47.5% of the total blade worth.

The "partial" blade worths obtained in the above manner for the two orientations were averaged and then adjusted for the differences in the widths of the absorbing portions. For this adjustment, the blade worth was assumed to be directly proportional to the width of the absorber portion of the blade. As mentioned earlier, the hafnium blades are 6 and $7\frac{1}{2}$ in. wide for the in-core and peripheral blades, respectively. If europia is used for the control material, the cermet must be clad. For comparison with the

hafnium blades, it was assumed that the europia blades would be of the same overall width with $1\frac{1}{8}$ in. of stainless steel at the blade edge, giving the cermet widths of $5\frac{1}{4}$ and $7\frac{1}{4}$ in. for the in-core and peripheral blades, respectively. The final adjustment was made by multiplying the "partial" blade worth by the ratio of the assumed cermet width to the actual cermet width. Table XXXIII lists these adjusted results with appropriate hafnium-blade data for comparison. The hafnium data in the table were obtained from calibrations of hafnium blades with stainless steel followers. As already mentioned, the hafnium thickness was 0.150 in. Measurements indicate that an increase in the hafnium thickness from 0.150 to 0.200 in. would increase the relative blade worth less than 10% as described in Sections D above and J below.

TABLE XXXIII. Adjusted Partial^a Worths of Control Blades

Plate Designation	Reactivity Control Worth ^b			
	Assembly 3		Assembly 4a	
	In-core Blade	Peripheral Blade	In-core Blade	Peripheral Blade
	No. 8	No. 4	No. 8	No. 4
Hf	0.54	0.48	0.48	0.43
S1	0.66	0.62	0.58	0.58
S2	0.63	0.62	0.55	0.55
M1	0.67	0.62	0.59	0.59
M2	0.59	0.58		

^aSee text for explanation of method used.

^bEstimated uncertainty in the tabulated values is $\pm 0.01\%$ in reactivity.

4. Conclusions

Table XXXIII shows that europia blades of the type described here are worth more, in terms of reactivity control, than hafnium blades of comparable size, provided the same blade follower is used.

The blade designated M1 has the greatest adjusted worth of any of the blades studied. This result is unexpected in view of the compositions given in Table XXXI. The relative ineffectiveness of M2, as compared to S2 and M1, is rather surprising. One would expect the hafnium stabilizer to augment the europium absorption, thus giving a greater overall blade worth. These apparent anomalies may be due to nonuniformities within the cermet or perhaps significantly different microstructures resulting from different fabrication processes.

J. Reactivity Worths of Small Samples in the AARR Critical Assemblies

1. Introduction

The reactivity worths of several small samples were measured at the midplane of Assemblies 1, 2a, 3, and 4a. In addition to these, some vertical traverses were taken in Assembly 4a, because of interest in the problems arising from banked control-blade operation and other factors resulting in nonuniform burnout of core materials. These measurements were made for comparison with calculations and to indicate the worths of various materials making up the core and the control blades. As far as is known, no previous comparisons have been made in a similar neutron spectrum.

2. Description of Samples and Methods of Measurement

Reactivities associated with the following materials were measured:

- a. Boral (22.2 w/o natural boron as B_4C-Al). This sample was taken from ~0.64-cm-thick plate and was ground to 0.508-cm thickness, removing the aluminum cladding layers.
- b. Boron-stainless steel (1.01 w/o natural boron). These samples were cut from a 0.025-cm-thick boron stainless steel strip similar to those used in the core loading to simulate burnable poison. Various thicknesses were obtained by combining these foils.
- c. Cadmium (pure metal). These samples were cut from rolled sheets of cadmium available from a stock pile, and scrap pieces that have accumulated over several years.
- d. Dysprosium. This is a pure metal, normally stored in mineral oil, which was obtained by special order.
- e. Europium-stainless steel (31 w/o europium). The europium oxide-stainless steel samples were taken from material obtained as a demonstration of the feasibility of a fabrication process. The outer cladding of stainless steel was ground away, but three remaining layers were observed in the thicker samples. Investigation indicated that the three layers were separated by ~0.001-in.-thick stainless steel foils, which had been included as moisture barriers to limit possible diffusion of water vapor about any point of failure in the cladding.
- f. Gadolinium oxide-stainless steel (0.7 w/o gadolinium). The use of gadolinium resulted from interest in its unusual neutron cross section, which involves a much lower effective cutoff energy than that of

cadmium. Because of its 49,000-barn thermal-neutron-energy cross section, the 0.7 w/o gadolinium sample is black to any thermal-energy neutrons falling below the cutoff energy. It was anticipated that this sample worth would be quite sensitive to the hardened neutron-energy distributions of these assemblies.

g. Hafnium-zirconium (97.5 w/o hafnium). This material was taken from samples remaining after completion of earlier experiments.

h. Nickel (commercial grade)

i. Stainless steel (Type 304)

j. Uranium-aluminum (17.44 w/o uranium, of which 93.17 w/o is ^{235}U)

Measurements were made for samples of different thicknesses and with the samples at different radial locations within the fuel region at the vertical midplane of the core. The samples were inserted into the core by means of a dummy control blade-sample holder in one of the three radial control-blade slots. The sample holder had the same dimensions as the control blades and was made from 2S aluminum. The maximum sample thickness was limited to the thickness of the sample holder (0.51 cm). The sample positions were in the lower portion of the sample holder so that the samples were below the core during reactor startup. The samples could then be raised to the midplane of the core with the standard control-blade drive mechanism. Three 2.18 x 2.18-cm sample holes were in a horizontal row across the width of the sample holder. The centers of these sample positions were at radii of 9.5, 15.7, and 21.9 cm. A later modification of the sample holder provided larger sample holes for the purpose of investigating edge effects. The larger holes were at the same radial distances from the center of the reactor. Sample holes that were not in use were always filled with aluminum blanks. When a sample thinner than 0.51 cm was used, the remaining volume of the sample hole was filled with an aluminum spacer to bring the total thickness to 0.51 cm.

The worth of each sample was obtained by observing either a rising period or a change in position of a calibrated control blade when the sample was moved from the midplane of the core to a position some distance below the core. This movement of the sample holder was equivalent to replacing the sample by 0.51-cm-thick aluminum. Thus the measured reactivity values were relative to a 0.51-cm-thick aluminum sample in the same position.

The set of space-dependent worth measurements in Assembly 4a was obtained using a sample traversing system with "on-line" computer processing of the data. Starting with the reactor critical, samples were

moved vertically between the midplane of the core and a position below the reactor. The samples were traversed in both directions to reduce the probability of systematic error. The resulting change of the neutron-flux level in the reactor was detected by an ion chamber and transmitted to the computer by means of an electrometer and a voltage-to-frequency converter system. The sample position and neutron-flux data were received simultaneously by the computer, which was equipped with on-line data-input scalars. The reactivity was calculated by the computer from the flux data using a set of one-energy-group, space-independent kinetic equations. The results were presented in the form of plots of reactivity versus sample position.

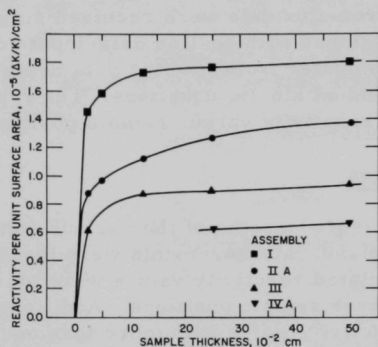
3. Measured Worths of Samples

Table XXXIV gives the measured worths of the various samples, which were positioned at the core midplane. Measurements were made in Assemblies 1, 2a, 3, and 4a. The tabulated reactivity values were obtained with identical samples in each of the three sample positions. Additional measurements have shown that the reactivity worth with more than one sample in the core is equal to the sum of the worths of the individual samples. This indicated that the samples are spaced sufficiently far apart so that there is very little interaction. The estimated error in the tabulated values is 0.001% in reactivity.

TABLE XXXIV. Comparison of Reactivity Worths of Small Samples in Fuel Regions

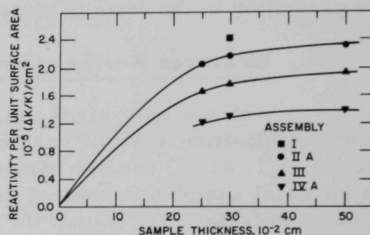
Sample Description	Sample Thickness, cm	Sample Weight, g	Sample Reactivity, %				
			Assembly 1	Assembly 2a	Assembly 3	Assembly 4a	
						By Period	By Traversal
Boral (B ₄ C-aluminum) (22.2 w/o B)	0.508	17.86	-0.1207	-0.1015	-0.0845	-0.0596	-0.0599
Boron-stainless steel (1.01 w/o B)	0.508	53.96	-0.0571		-0.0372	-0.0221	-0.0221
	0.254	26.98		-0.0288	-0.0191		
	0.127	13.49		-0.0146	-0.0115		
Cadmium	0.508	62.70	-0.0753	-0.0570	-0.0389	-0.0280	-0.0289
	0.254	31.35	-0.0618	-0.0447	-0.0315	-0.0209	-0.0212
	0.127	15.68	-0.0549	-0.0356	-0.0278		
	0.051	6.27	-0.0471	-0.0288			
	0.025	3.14	-0.0421	-0.0253	-0.0178		
Dysprosium	0.025	3.06				-0.0138	-0.0139
Europium oxide-stainless steel (31 w/o Eu)	0.396	43.30	-0.1218	-0.1065	-0.0863	-0.0656	-0.0667
Gadolinium oxide-stainless steel (0.7 w/o Gd)	0.508	56.05	-0.0358	-0.0234	-0.0154	-0.00935	
Hafnium-zirconium (97.5 w/o Hf)	0.508	92.27		-0.0997	-0.0800	-0.0608	-0.0612
	0.302	55.13	-0.0878	-0.0789	-0.0637	-0.0464	-0.0459
	0.254	46.14		-0.0715	-0.0583	-0.0431	
Nickel	0.508	63.72				-0.0043	
Stainless steel (Type 304)	0.508	56.87	-0.0076	-0.0053	-0.0046	-0.0027	
Uranium-aluminum (17.44 w/o U, 93.17 w/o ²³⁵ U)	0.462	19.91	0.0146		0.0042	0.0054	0.0050
	0.198	8.54		0.0036	0.0023		
Water	0.508	21.66	0.0076	0.0068	0.0051	0.0040	

Figure 109 shows the relative worth of cadmium as a function of sample thickness for the four assemblies. The data have been plotted in terms of worth per unit surface area (not extent, as in the ITC work). Figure 110 is a similar plot of the hafnium data.



113-1565

Fig. 109. Cadmium Sample Worth vs Thickness



113-1566

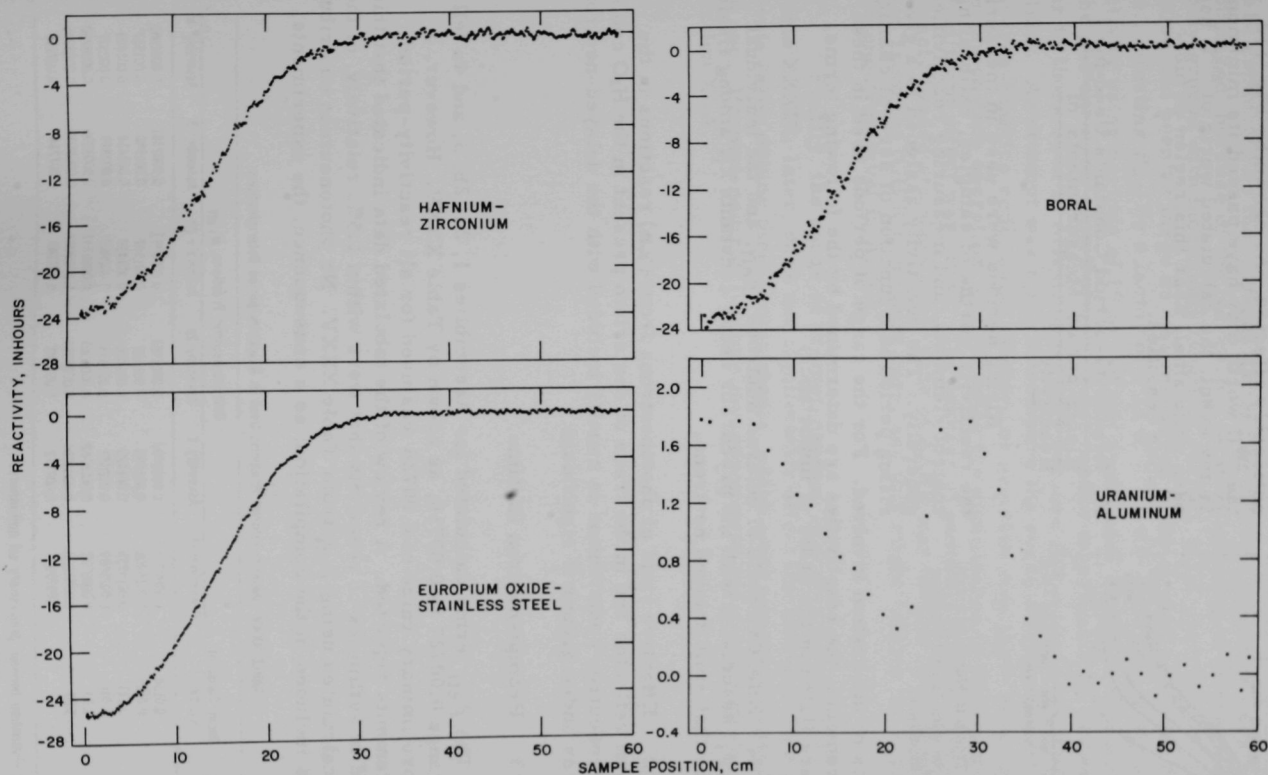
Fig. 110. Hafnium Sample Worth vs Thickness

Figure 111 shows the vertical traverses taken with hafnium, europia-stainless steel, boral, and uranium-aluminum. The worth of uranium is greatest at a peak located ~4 cm above the lower edge of the fuel region, rather than at the midplane. This is attributed to the influence of the reflector. The averaged midplane worths from this measurement were included in Table XXXIV, to permit comparisons with period measurements. The comparisons indicate that the vertical distributions obtained by this method are almost as accurate, when averaged, as if taken by rising periods, which would be prohibitively time-consuming.

4. Conclusions

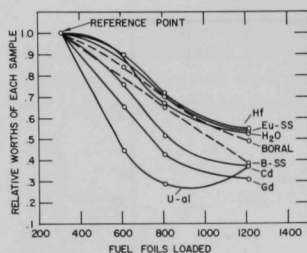
The tabulated data indicate that the europia-stainless steel sample controlled more reactivity than any other sample tested, in each assembly. Boral and hafnium were about 90% as effective as the equal volume of europia-stainless steel, in Assembly 4a, and almost equal to it in the earlier loadings. Since a hafnium blade would not be clad, it would be more effective initially than boral and very nearly equal to europia-stainless steel, if of equal thickness, including any cladding, and equipped with a zirconium follower. This europia-stainless steel coupon may not have been quite as effective as the material used in Section I.

As expected from the gadolinium neutron cross section, which has an effective cutoff in the vicinity of 0.1 eV, the worth of this sample was more drastically affected by increased fuel-loading density than that of cadmium. The highly enriched uranium-aluminum sample was even more



112-8585 Rev. 1

Fig. 111. Worths of Various Samples Traversed from Midplane of Assembly 4a through Bottom Reflector



113-1568

Fig. 112. Trends in Worths of Small Samples As Fuel Loadings Increased

noticeably affected. As shown by Fig. 112, the ^{235}U worth may have passed its minimum. In any event, the calculated worth of ^{235}U has been quite small near this region of fuel-loading densities.

K. Reactivity-period Constants Used for Rising-period Measurements of Reactivity

Rising periods were used in measuring the reactivity worths of samples, calibrating control elements, and measuring reactivities generally. The reactivity assigned to a given rising period is a function of several characteristics of the system involved. For the range of periods used in these measurements, the reactivities are determined by the following terms, which are listed in the order of importance:

1. Effective yield of delayed neutrons, β_{eff} , and the individual yields, β_i , associated with the precursor decay constants λ_i , among fission products that emit delayed neutrons.
2. Effective yield of photoneutrons from (γ, n) reactions in the beryllium reflector and in the trace of deuterium present in the H_2O coolant. The photoneutron contribution is usually included with the delayed-neutron groups as added groups if significant.
3. Prompt-neutron lifetime.

The β_{eff} terms calculated for Assemblies 1, 2a, 2b, 3, and 4a fell in the range 0.00727 to 0.00716, as shown by Table XXXV. However, a single preliminary value of 0.00726 was used for all reactivity-period measurements reported. A review of the tabulated data indicated that this resulted in estimates of reactivity that were within 1.5%, relatively, of the values calculated using β_{eff} from Table XXXV. No photoneutron contribution was included in the compilation; as a consequence, the experiments

TABLE XXXV. Delayed-neutron Fractions Used in Reactivity-period Determinations

Delay Group (i)	Decay Constant $\lambda_i, \text{sec}^{-1}$	Delayed-neutron Fractions, $\beta_i \text{ eff}$					
		Preliminary ^a	Assembly 1	Assembly 2a	Assembly 2b	Assembly 3	Assembly 4a
1	0.0124	0.0002397	0.0002400	0.0002383	0.0002391	0.0002381	0.0002362
2	0.0305	0.0015906	0.001593	0.001582	0.001587	0.001580	0.001567
3	0.111	0.0014235	0.001425	0.001416	0.001420	0.001414	0.001403
4	0.301	0.0028689	0.002872	0.002853	0.002862	0.002849	0.002827
5	1.13	0.0008352	0.0008362	0.0008305	0.0008332	0.0008296	0.0008230
6	3.00	0.0003050	0.0003054	0.0003033	0.0003043	0.0003030	0.0003006
Totals		0.007263	0.007272	0.007222	0.007245	0.007214	0.007156

^aSee text for distinction between preliminary set and others.

were conducted so that periods as long as 100 sec generally were not encountered, because of the increasing relative importance of photoneutron delay groups with increasing length of period. If the photoneutron contribution had been as large as was measured in the aluminum cores of AHFR,¹ i.e., affecting β_{eff} by a factor of 1.12 to 1.16, the underestimation of reactivity using periods of 10 to 100 sec would have been 1 to 5% relatively. The photoneutron contribution was not readily measurable by methods similar to those used in AHFR, apparently because it was much smaller than in AHFR. An attempt was made to compare the reactivities indicated by the inverse-kinetics code, using positive or negative step-input reactivities during on-line operation, to determine the significance of photoneutrons. No significant effect was found. The leakage of gamma radiation from the densely loaded stainless steel core of AARR was thought to be much less than from the AHFR aluminum core, and this might explain the negligible photoneutron level in AARR.

Finally, the range of prompt-neutron lifetimes indicated by Table XXXIX, later, does not significantly affect the rising-period measurements taken during these experiments, which were generally longer than 10 sec. Prompt-neutron lifetime measurements are discussed in Section XI.A.

X. MEASUREMENTS OF TEMPERATURE COEFFICIENTS AND RADIAL-H₂O VOID WORTHS

A. Introduction

Originally, only mild interest was evident in the temperature coefficient and the radial-void worth of the critical experiment because the calculated value for AARR had indicated satisfactory self-limiting behavior in the event of an accident. Only rough measurements of temperature coefficient were made with Assemblies 2a and 3, and none with Assembly 1. Results of these measurements indicated less effective temperature coefficients rather than the AARR calculated values that had been expected.

We now believe that the use of aluminum top and bottom spacer plates (shown in Fig. 1) in the critical facility has caused a significantly larger expansion coefficient than would be found in a similar system constructed entirely of stainless steel. Although no hazard results from this, because the spacer plates would remain at the temperature of the surrounding water during any accident, the isothermal measurements performed during critical experimentation cause the core to expand with the linear-expansion coefficient of aluminum, in the radial direction. The resulting coefficient is different from that expected for AARR, but an analysis indicates that the difference is reasonable.

Because the temperature coefficient was not as great as expected over the range of temperature feasible in this facility, the equipment and procedures used for the measurements had to be improved.

Variations in blade worths were suspected during the temperature-coefficient measurement in Assembly 2a, but it was not feasible to recalibrate the blades at temperatures much above room temperature, because of the condensation of water vapor on the high-voltage and signal leads from the flux detectors at elevated temperature. The length of runs was limited by frequent scrams. This difficulty was eliminated during the experiments in Assembly 3, and some recalibration was done with and without massive voids in the ITC at two different temperatures. The variations in blade worth with temperature are discussed in Section IX.E for measurements in Assemblies 3, 4a, and 5.

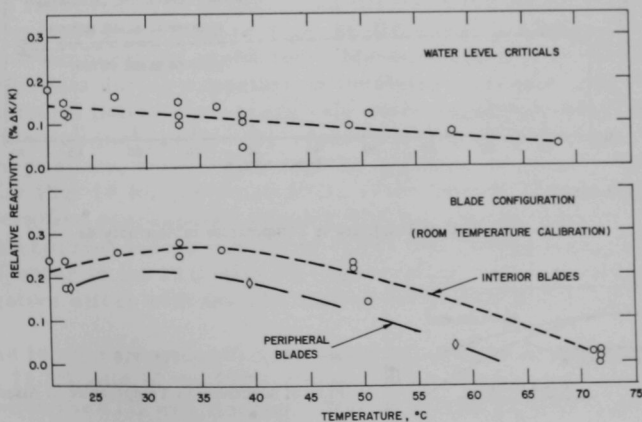
Presence of fuel extending above the water level during water-level criticals and the stationary nature of the beryllium reflector cast some doubt on the reliability of measurements of temperature coefficients by critical water height, with all blades withdrawn. The eventual outcome was in reasonably good agreement between the corrected measurements obtained by control blades and the results of the water-level measurements.

B. Results of Temperature-coefficient Measurements with the ITCs Flooded

Temperature coefficients were measured under isothermal conditions obtained by using an external water heater and by stirring the reflector and moderator water with a 3-hp electric-motor-driven mixer while waiting until uniform temperatures were indicated by thermocouples placed in the core and reflector. Reactivity changes were measured by rising-period calibrations of the worth of the H_2O level at or near the critical level, with all control blades withdrawn, and also by calibration of the critical control-blade configurations with water raised to provide a thick top reflector. The shape of the plot of temperature coefficient versus temperature is not shown accurately by the blade configurations because the calibrations changed with temperature. Only a few points were obtained for which k_{ex} was measured by recalibration of the control blades at elevated temperature.

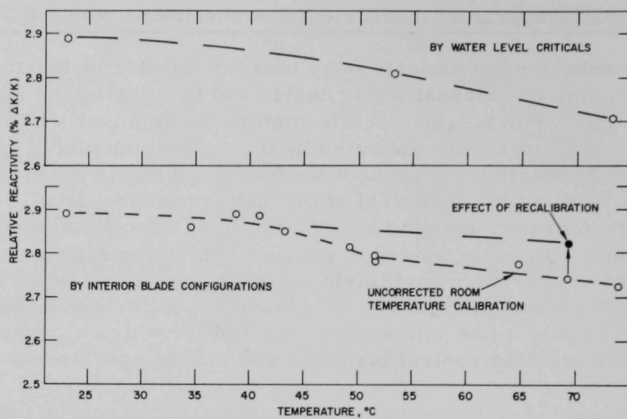
Figures 113-116 are plots of reactivity trends versus temperature for Assemblies 2a, 3, 4a, and 5, respectively. Although several differences in blade configurations were tried, there is no great difference in the trends obtained. The measurements with banked control blades in Assembly 5 are similar to the expected AARR operating configurations. The apparent coefficient indicated by blade motion includes the change in reactivity of the core and the change in blade worths as the temperature was changed. The apparent coefficient will vary from time to time in AARR as the core cycle progresses, because of changes in blade configuration as fuel and poison burnout.

Table XXXVI gives a rough comparison of the temperature coefficients for these assemblies. Extrapolation to AARR operating conditions



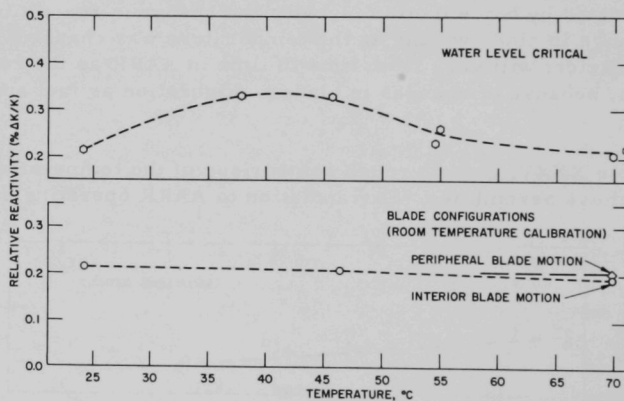
113-1581

Fig. 113. Plots of Reactivity vs Temperature in Assembly 2a



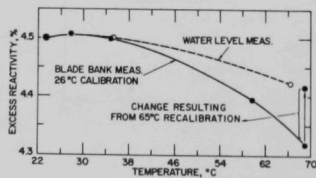
113-1584

Fig. 114. Plots of Reactivity vs Temperature in Assembly 3



113-1582

Fig. 115. Plots of Reactivity vs Temperature in Assembly 4a



112-8938

Fig. 116

Plots of Reactivity vs Temperature in Assembly 5

TABLE XXXVI. Comparison of Measured Temperature Coefficients of Assemblies 2a, 3, 4a, and 5

Assembly No.	Coefficient at ~65°C by Water Level, Percent Reactivity per °C	Coefficient at ~65°C by Blade Configuration, Percent Reactivity per °C
2a	-0.002	-0.009 ^{a,b,c}
3	-0.005	-0.002 ^{b,d} -0.003 ^{a,b}
4a	-0.002	-0.000 ^{a,b,c}
5	-0.003	-0.003 ^{d,e} -0.006 ^{a,e}

^aUncorrected blade calibrations obtained at room temperature.

^bIn-core control blades used for measurement.

^cPeripheral blades used for measurement.

^dBlade calibration obtained at ~65°C.

^eBanked in-core blades used for measurement.

may not be justified using measurements taken in this limited range. All coefficients measured appeared to be negative in the vicinity of 65°C, but the Assembly 5 coefficient is positive in the region below 30°C, and some of the others are questionable in that region.

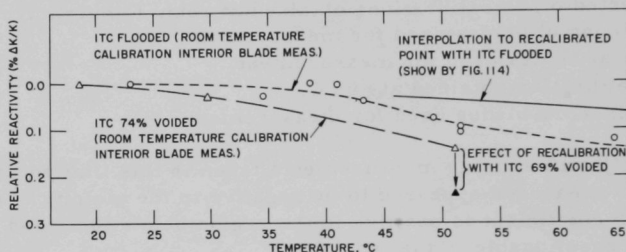
C. Temperature-coefficient Measurement in Assembly 3 with Massive Void in ITC

The installation of samples and fillers in the AARR may change the ITC water volume from time to time, as discussed in Chapter IV, and thereby affect the temperature coefficient. Measurements of isothermal temperature coefficients during experiments involving increased ITC void fractions were expected to indicate progressively more negative coefficients as the void fraction was increased. The reason for this is the change in ITC void worth from positive, below ~50% void, to negative, at greater than ~50% void as shown by Fig. 14 for the small ITC. If the density change of ITC water with temperature corresponds equally with the change in water density by voiding, the corresponding reactivity effect will change sign. Thus the expansion of water in the ITC with increased temperature should be a significantly negative effect with the ITC voided more than 50%.

The temperature coefficient was measured in Assembly 3 with an estimated 73.8% void in the ITC. Control-blade motion was almost twice as great as when the ITC was flooded. The room-temperature calibrations of the control blade were identical in this assembly, whether measured with the ITC voided or flooded. However, at elevated temperatures, the calibrations

diverged. The blade calibration with the ITC voided was only ~ 0.93 as great at 51.1°C as at room temperature. (One void tube leaked during the startup for this recalibration, which was obtained with 69% ITC void.) On the other hand, the calibration with the ITC flooded showed the blade worth to be 1.03 times greater at $\sim 75^\circ\text{C}$ than at room temperature. This increase in blade worth would tend to shut down the reactor if there had been no compensating withdrawal of the control blade.

Plots of the temperature-coefficient measurements when the ITC was 74% voided, and when flooded, are given by Fig. 117. Not only was there greater motion of the control blades when voided than when flooded, but the blade calibrations changed so that the reactivity difference was greater, rather than less. (The effect of recalibration when the ITC was flooded is shown by Fig. 114.)



113-1578 Rev. 1

Fig. 117. Plots of Reactivity vs Temperature with ITC Voided and Flooded, in Assembly 3

On the basis of the measurement, it appears that the ITC water volume is a significant factor in the isothermal temperature coefficient, and that the effect of voiding is qualitatively the same as predicted.

D. Measurements of Radial Void Worths

1. Simulation of Small Voids by Teflon

Small voids were simulated by installing 1.27-cm-diam Teflon rods in the ITC (as described in Section IV.D) and by inserting 1.26-cm-wide by 0.081-cm-thick Teflon strips into the coolant channels of the fuel region to displace water. This was a continuation of the method used in the AHFR Critical Experiment.¹

The rods extended from 4 cm above to 4 cm below the fuel region, and the strips from ~ 4 cm above to ~ 2 cm below the fuel region. Figure 8 shows the positioning of the rods in the ITC. The Teflon strips were bunched because they were inserted into the fuel region through holes in the top spacer plate which correspond to the 1/2-in.-diam drain holes indicated by Fig. 1.

The Teflon rods were shown to interact in the ITC by as much as 8%, by reversing the sequence of withdrawal in Assembly 4a. No interaction was detected between the control blades and the simulated voids during the small void experiments. Interactions during massive ITC void experiments are described in Sections IV.E and IX.E.

Displacement of water by Teflon is not quite equivalent to displacement by air or steam voids, because of the presence of carbon atoms in Teflon. The calculated equivalence factor for the Assembly 4a (under-moderated) fuel region⁶ was 1.1 volumes of Teflon per volume of void. A factor that is very close to unity applies in the ITC because moderation by carbon is relatively inconsequential in comparison to moderation by water.

Consequently these uncorrected measurements underestimate the reactivity of void in the fuel region water by about 10%. Only negligible error is thought to have occurred, because of the use of Teflon instead of equally large void volumes in the ITC. The Teflon rods used in the ITC were rather large (1.27-cm diam), and there may have been a small error in the average worth measured therein, compared to genuine small void worths. The center rod alone was worth relatively about 8% less than when measured with the other four Teflon rods in place, during a radial-worth measurement in Assembly 4a.

2. Volume-averaged Void Worths

ITC void worths were measured in Assemblies 2a, 3, 4a, and 4b, and void worths in the fuel-region coolant space were measured in Assemblies 1, 2a, 3, and 4a. Radial distributions through the fuel region were obtained only in Assemblies 3 and 4a. However, all the measurements were planned to yield volume-averaged void worths.

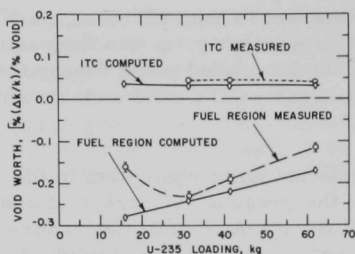
Table XXXVII and Fig. 118 give the volume-averaged results for all the measurements. Extrapolation of the data for the fuel region

TABLE XXXVII. Average Void Worths (Small Void Measurement at Room Temperature)

Assembly No.	ITC Void Worth ^a	Fuel-region Void Worth ^b	Assembly Average
1		-0.159	
2a	+0.044	-0.228	-0.184
3	+0.044	-0.190	-0.146
4a	+0.040	-0.116	-0.076
4b	+0.053		

^aIn percent reactivity per percent of H₂O displaced from the ITC by 1.27-cm-diam Teflon rods. These measurements were in the small ITC having 100 cm² area of water, except for Assembly 4b. Values for Assemblies 3 and 4b were from Tables XIII and XIV. Data for Assembly 4b have estimated errors of ± 0.005 ; those for Assemblies 2a, 3, and 4a have estimated errors of ± 0.002 .

^bIn percent reactivity per percent of H₂O displaced from the coolant channels by 1.26-cm-wide by 0.081-cm-thick Teflon strips.



112-6542

Fig. 118. Average Void Worths in Assemblies 1, 2a, 3, and 4a

of a fixed size are nearly identical in these ITCs and the difference in coefficients results mostly from normalizing to reactivity per percent of ITC volume.

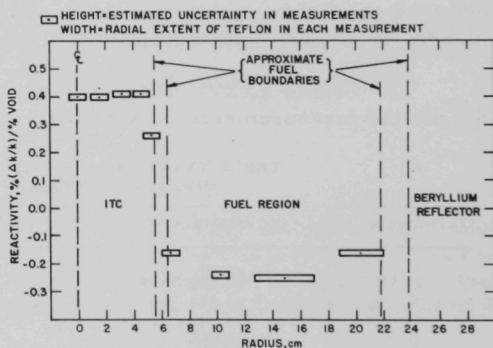
3. Distributions of Radial Void Worths

The radial distributions of void worth were measured in the fuel regions of Assemblies 3 and 4a, and in the ITCs of Assemblies 2a through 4b. The purpose of these measurements was to investigate the transition regions near the inner and outer boundaries of the fuel zone where the void coefficient changes from positive, in the ITC and in the radial reflector, to negative, in the fuel zone. These radial measurements did not indicate that any significant area-weighting error had occurred in the volume-averaged results reported in Section 2 above. The transitions from positive to negative values occurred within a very short distance along the radius. Apparently the transitions took place mostly outside the fuel region, as indicated by Fig. 119, which is a plot of radial void worth for Assembly 3.

If the loading is graded or power-flattened so that boiling commences fairly uniformly throughout the fuel region, the volume-averaged coefficient should apply. Thus the radial distribution was of no interest in the AARR Assembly 5, which had a graded fuel loading. In the AHFR aluminum core experiments,¹ the region of positive void worth extended into the edge of the fuel zone, which was not graded, and it was thought that instability might accompany incipient boiling in such a system.

suggests that the void coefficient might become positive if the uranium loading were increased by ~25% beyond that of Assembly 4. A similar trend is evident in Fig. 112, which indicated both a reduction in water worth and an increase in ²³⁵U worth as the fuel loading was increased from 810 to 1215 fuel foils.

The average void worth for the ITC of Assembly 4b (in percent reactivity per percent of void in the ITC volume) is larger than for Assemblies 2a and 3 because of the larger ITC size. The worths of small voids



112-5727

Fig. 119. Radial Dependence of Void Worth in Assembly 3

The distributions of radial void worth in the ITC of Assembly 4a was measured with two withdrawal sequences of the Teflon rods. As listed in Table XXXVIII, differences as large as 8% in relative worth occurred in Assembly 4a because of changing the central piece from first to last in the sequence of removal. This difference was attributed to interactions between the Teflon rods.

TABLE XXXVIII. Distributions of Radial Void Worths

Assembly No.	Sample- removal Sequence	Radius, cm	Reactivity Change, ^a	Localized ^a
			%	Void Coefficient, % per % Void in H ₂ O
<u>ITCs</u>				
2a	Last	0.0	0.060	0.047
	Fourth	1.59	0.060	0.047
	Third	3.18	0.062	0.049
	First	4.58 (edge)	0.059	0.046
	Second	5.33 (edge)	0.041	0.032
3	Last	0.0	0.059	0.046
	Fourth	1.59	0.059	0.046
	Third	3.18	0.061	0.048
	First	4.58	0.061	0.048
	Second	5.33	0.039	0.031
4a	Last	0.0	0.051	0.040
	Fourth	1.59	0.051	0.040
	Third	3.18	0.055	0.046
	Second	4.58	0.059	0.046
	First	5.33	0.039	0.031
4a	First	0.0	0.055	0.043
	Second	1.59	0.055	0.043
	Third	3.18	0.053	0.042
	Fourth	4.58	0.055	0.043
	Last	5.33	0.037	0.029
<u>Fuel Region</u>				
3		6.67		-0.141
		10.24		-0.206
		14.85		-0.218
		20.32		-0.141
4a		5.74		-0.027
		6.58		-0.091
		10.09		-0.136
		12.31		-0.149
		15.11		-0.123
		19.44		-0.100
		22.47		-0.050
		5.5 ^b		+0.12 ^b
		5.7 ^b		-0.03 ^b
	22.1 ^c		+0.11 ^c	

^aReactivity loss measured on withdrawal of 1.27-cm-radius Teflon rod from small ITC containing 100-cm² area of water space.

^bApproximate results for single Teflon strips positioned on the ITC side of an inner fuel plate (5.5 cm) and between an inner fuel plate and the one next farther out (5.7 cm).

^cApproximate results obtained in the peripheral (or safety) blade slot.

In addition to the radial-worth data described in this chapter, the information on the worth of water and of plastic fillers in the beam tubes, and the change from Assembly 2a to 2b, might be used to indicate the radial worth of water or voids in the beryllium reflector.

E. Estimated Effects of Thermal Expansion on Temperature Coefficient

1. Expansion of Core Structure with Temperature

The volume expansion of the core was taken to be the sum of the linear coefficients in three directions. The height was controlled by the thermal coefficient of linear expansions of uranium or stainless steel, which is about $15 \times 10^{-6}/^{\circ}\text{C}$. The radius was controlled by the top and bottom aluminum spacer plates having a linear coefficient of about $24 \times 10^{-6}/^{\circ}\text{C}$. The volume coefficient is therefore the sum of $(15+24+24)10^{-6}$ or $\sim 63 \times 10^{-6}/^{\circ}\text{C}$.

Differential water-height measurements ranged from 0.09 to 0.20% reactivity per centimeter of height near the top of the fuel. Since a centimeter of core height is about 2% of the core volume, a rough estimate of worth is therefore $0.07 \pm 0.03\%$ reactivity per percent of core volume.

Multiplying the reactivity per percent volume by the volume expansion coefficient yields the reactivity coefficient of structural expansion, or approximately $0.0005 \pm 0.0002\%$ reactivity per $^{\circ}\text{C}$ in these assemblies.

2. Expansion of Water with Temperature

The combined reactivity coefficient of water volume and structural expansion is positive up to a temperature at which the two effects cancel, and negative above that temperature. This results from the increasing volume-expansion coefficient of water with increasing temperature. (The coefficient is negative below $\sim 4^{\circ}\text{C}$.)

From Table XXXVII, the range of average void worths is -0.076 (for Assembly 4a) to -0.181 (for Assembly 2a) percent reactivity per percent of water volume. Taking these two values, we calculate the temperatures at which the reactivity effects of expansion cancel, as well as expansion temperature coefficients at 65°C corresponding with those given by Table XXXVI. Cancellation occurs at 45°C or higher for Assembly 4a, and between 20 and 40°C for Assembly 2a. The temperature effect at 65°C is small but probably negative for Assembly 4a, and about $-5 \times 10^{-4}\%$ per $^{\circ}\text{C}$ for Assembly 2a. (Water densities were taken from Ref. 25.)

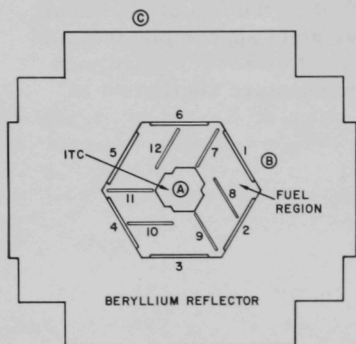
3. Conclusions

The foregoing results are in reasonable agreement with Figs. 113 and 115 and Table XXXVI. This suggests that the expansion of water and of structural members with temperature provides practically all the temperature coefficients of these assemblies. The expansion of the core in the critical facility was exaggerated by the use of aluminum spacer plates at the top and bottom. Stainless steel spacer plates would have reduced the structural expansion coefficient by about a third, and would have increased the magnitude of the temperature coefficient at 65°C by about $2 \times 10^{-4}\%$ per °C.

XI. MISCELLANEOUS MEASUREMENTS

A. Measurement of Prompt-neutron Lifetime by Rossi-alpha Technique

Prompt-neutron lifetime (ℓ_p) was measured to confirm the method of calculating the lifetime in the multiregion AARR system as indicated by Fig. 120. Both the importance and the moderating ratio vary radically in different regions such as the ITC, the graded fuel region, and the beryllium reflector. The prompt-neutron lifetime affects the transient behavior of a reactor, particularly during prompt critical excursions; hence accurate values are needed for accident analyses.



112-9157

Fig. 120. Top View of AARR Critical Facility

Table XXXIX lists values of the measured prompt-neutron lifetime (ℓ_p) along with calculated values of effective delayed-neutron fractions⁶ and control/safety-blade configurations. The measured values of ℓ_p were determined by using the following equation:

$$\alpha = \frac{1 - k_p}{\ell_p} = \frac{1 - k + \beta_{\text{eff}}}{\ell_p} = \frac{-\Delta k + \beta_{\text{eff}}}{\ell_p}, \quad (14)$$

which includes the usual correction for subcriticality. The choice of control/safety-blade configuration had a significant effect (on the prompt-neutron lifetime of the system) because the peripheral blades tended to decouple portions of the beryllium reflector from the remainder of the assembly.

TABLE XXXIX. Summary of Measurements of Prompt-neutron Lifetimes in AARR Critical Facility

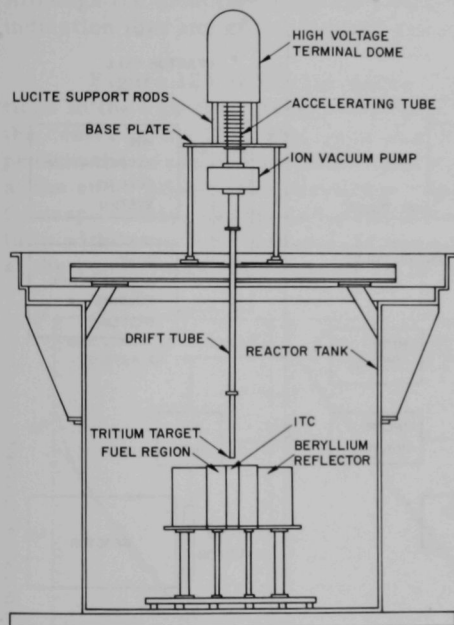
Assembly No.	Calculated β_{eff}^a	Prompt-neutron Lifetime, μsec	Number and Type of Control Blades Inserted during Experiment
1	0.00727	39.5 ± 1.0	0.3 interior
2b	0.00721	33.0 ± 2.0	2.5 peripheral
3	0.00718	31.9 ± 2.0	2.3 peripheral
4a	0.00712 ^b	26.7 ± 1.0	2.0 peripheral
4b	0.00712 ^b	27.8 ± 2.0	2.3 peripheral
5	0.00712 ^b	33.7 ± 2.0	3.6 interior
5	0.00712 ^b	22.3 ± 2.0	3.3 peripheral

^aTaken from Ref. 6.^bAssumed to be equivalent to 1215/2000 loading of Ref. 6.

Subcritical operation, typically with a Δk of about -10^{-3} , was necessary to avoid obscuring the correlated counts by uncorrelated (or randomly occurring) counts. The normal startup source level gave a count rate which was much too high for use in measurement of α , and the startup source was withdrawn far enough to lower the count rate by about two decades, during these measurements.

B. Pulsed-neutron Measurements

A pulsed-neutron generator was installed in the ZPR-5 cell for a series of experiments with the AARR Critical Facility. Figure 121 shows its location on the main support platform directly above the critical facility. Measurements were made with the target just above the core, as shown in Fig. 121, and with the target inserted into the ITC to the midplane of the core by using a longer drift tube. With minor modifications, the generator could be removed from its position above the reactor and set up for operation in a horizontal position.



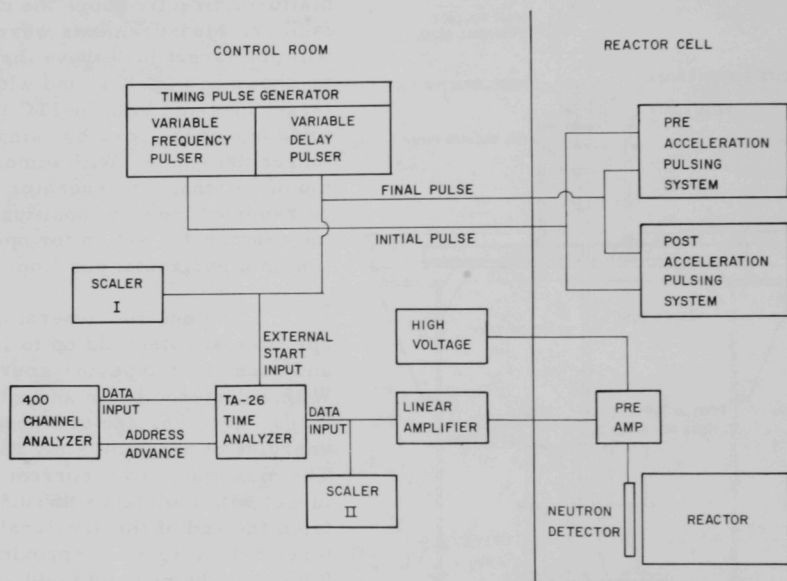
112-9164

Fig. 121. Sectional View of AARR Critical Facility
Showing Reactor and Pulsed-neutron Generator

The neutron generator operates at potentials up to 150 kV and uses an rf-type ion source. With a deuteron beam and a tritium target, neutrons are produced with energies of approximately 14 MeV. The maximum beam current at the target with a distance of 10.5 ft from the end of the accelerating tube to the target is approximately 0.5 mA. The neutron yield at 150 kV and 0.5 mA is estimated to be 5×10^{10} neutrons/sec. The neutron generator is equipped with pre- and postacceleration pulsing, providing a very low between-pulse

neutron-production rate. The width of the beam pulses is continuously variable from 1 μ sec to 5 sec, compatible with a pulse-repetition rate continuously variable from 5×10^5 pulses per sec to one pulse every 10 sec and a maximum duty cycle of 90% in pulsed operation. There is also provision for external triggering of the pulsing system, thus permitting nonperiodic pulsing, which would be of value for pseudorandom impulse response studies, for example.

Figure 122 is a block diagram of the pulsing and time-analysis system. The pre- and postacceleration pulsing systems operate simultaneously to minimize the beam current between pulses. The deuteron beam is allowed to reach the tritium target only during the time interval between the initial and final pulses from the Timing Pulse Generator. The final pulse was also used as the start signal for the time analyzer. Signals from a neutron detector in the reactor were analyzed in time relative to this start signal, which coincided with the trailing edge of the accelerator beam pulse. A 400-channel analyzer provided memory and readout equipment. The time interval covered by a "sweep" of the analyzer is equal to the product of the number of channels (400) and the preselected channel width. For this set of experiments, channel widths of 16, 20, 40, and 80 μsec were used.



112-9156

Fig. 122. Schematic Diagram of Time-analysis System

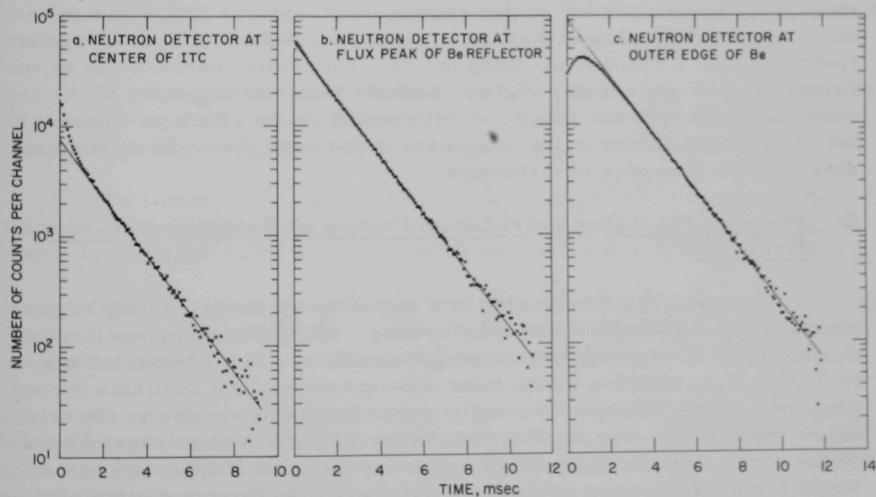
The initial phase of operation was directed toward familiarization and debugging. This was followed by a series of exploratory measurements. The first of these measurements was to determine which combinations of pulse width, repetition rate, beam current, and generator voltage would be compatible with normal reactor operation. Different detector types were compared, and the effect of detector location was studied. A search for fundamental modes was made with different critical configurations. The magnitude of higher-order modes was determined in different locations in order to ascertain the optimum detector location for different measurements. Data-analysis programs were developed concurrently.

Four types of neutron detectors were used in the pulsed measurements:

1. BF_3 proportional counter, 1-in. diam, 2-in. active length, 65-cm-Hg filling pressure,
2. BF_3 proportional counter, 1-in. diam, 15-in. active length, 120-cm-Hg filling pressure,
3. BF_3 proportional counter, 0.5-in. diam, 6-in. active length, 140-cm-Hg filling pressure,
4. ^{235}U fission chamber, 0.5-in. diam, 1-in. active length.

Although the detection efficiency varied over a wide range, there was no indication that any of the results were dependent on detector type.

Figure 123 shows the decay of the neutron population at three locations in the reactor. Figure 123a was obtained with the neutron detector at the center of the ITC, Fig. 123b was obtained with the detector at the flux peak in the beryllium reflector, and Fig. 123c was obtained with the detector at the outer edge of the beryllium. These locations are shown as A, B, and C, respectively, in Fig. 120. For these three runs, control blades 1-6 were fully withdrawn and blades 7-12 were fully inserted. The tritium target was at the centerline of the reactor 14 in. above the midplane of the core.



112-9398 Rev. 1

Fig. 123. Response Curves a, b, and c (Left to Right) for Detector Positions

The solid lines in Fig. 123 represent least-squares fits to the experimental data, assuming a single exponential decay after an appropriate

waiting time. The decay constants were consistent within 1%. The transient response, on the other hand, is significantly different in each of the three locations. A detector location near B seems to be desirable for fundamental-mode measurements because of the small contribution of transients to the decay in this region.

In most runs, after subtraction of background (predominantly delayed neutrons), the resulting data indicated an asymptotic exponential decay. For the far subcritical case in which all control rods were inserted, the existence of a pure exponential decay was not definitely established.

As observed in the Rossi-alpha experiments, decay constants were more sensitive to peripheral control-blade position than to interior control-blade position. Again, this is attributed to the fact that neutrons returning to the fuel region from the beryllium reflector tend to have relatively long lifetimes and thus tend to increase the average prompt-neutron lifetime of the reactor. Control elements that preferentially remove "older" neutrons from the reactor have a strong influence on the rate of decay of the neutron population in the reactor.

Digital-computer programs were developed to correct the time-analyzer data for dead-time losses and to estimate and subtract background. Final data fitting was done with PHY-141, which uses the variable metric method for minimization²⁶ in performing least-squares fitting to one or more exponentials plus background. Subroutine FCN of PHY-141 was modified to include a channel-dropping option. This option permits one to successively drop any number of data channels from the beginning of the decay curve and then refit the data to an exponential decay. Such an option is useful for eliminating errors in the evaluation of the asymptotic decay constant by detecting the presence of transients.

C. Measurement of Gamma-radiation Heating by Thermoluminescent Dosimetry

Gamma-radiation heating is a major factor in the cooling requirements of the AARR reflector and shielding. Although thermoluminescent dosimetry (TLD) had not been used previously in critical experiments, this technique was judged to be the most appropriate method available for mapping the gamma-radiation heating at power levels obtainable in the critical experiment, which was limited to no more than 300 W total (fission) power in the core. The heating rate was of the order of 10^{-30} C/hr, which was too small for accurate calorimetry, but quite adequate for irradiation of thermoluminescent powder.

The TLD measurements made in the critical experiment are only summarized here. The method and the results obtained are reported separately.²⁷

The development of materials, equipment, and procedures suitable for measurements in the critical experiment was necessary in order to avoid difficulty with neutron activation, contaminants, and other complications. The phosphor used for the TLD measurements was manganese-activated calcium fluoride ($\text{CaF}_2\text{:Mn}$), which, as was confirmed by experiments in the course of this work, yielded results that were not significantly perturbed by any effects due to either slow- or fast-reactor neutrons. The irradiations were performed with the powdered phosphor in thin layers, surrounded only by the material in which gamma-ray heating was to be measured. The Bragg-Gray theory of cavity ionization²⁸⁻³⁰ was used in analyzing the data.

The absolute dose rates were determined by comparing the TLD samples with standards composed of phosphor from the same batch, exposed in a calibrated ^{60}Co gamma-ray irradiation facility.

A correction factor is needed to allow for the difference in gamma-ray spectra between the calibration facility and the critical assembly. The correction was determined empirically, for a position in the beryllium reflector 10 cm from the core, in an experiment in which the response of TLD samples was compared with that of an ion-current chamber, both in the ^{60}Co irradiation facility, and in the critical assembly. For the position at which the measurement was made, the factor was 1.20 ± 0.12 . All TLD measurements in the reactor were corrected by this factor, which would be expected to vary somewhat with the point of measurement, but the uncertainty in this correction is a small part of the overall experimental error.

The factor thus determined included any sensitivity to neutrons, but on the basis of calculations and other experiments we concluded that, for this method, any such sensitivity was small.

The result of the above experiment indicated that the gamma spectrum in the beryllium reflector of the reactor near the core had an appreciable low-energy component, in qualitative agreement with calculations.

Other experiments indicated that local heating in the beryllium near the core was a function of the nearby fuel-plate orientation, presumably because of gamma-ray streaming in the water channels.

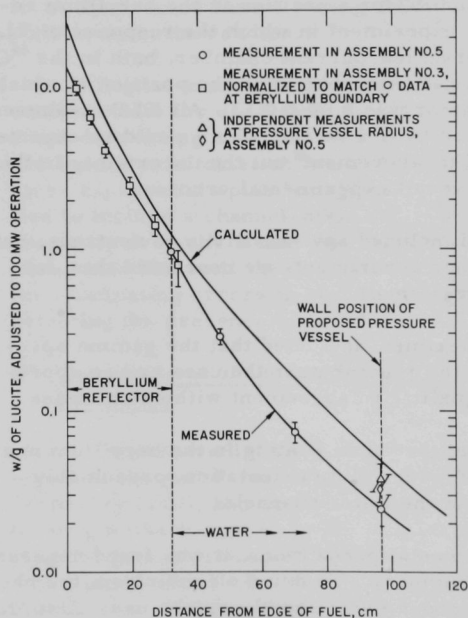
As one of the major experimental precautions, it was found necessary to avoid exposing the phosphor to humidity. To drive off moisture, the phosphor was baked for a few hours at about 400°C shortly before use. Also, for irradiation, the powder was enclosed in capsules of the material under investigation, and the capsules were closed by O-ring seals.

Among the heating-rate measurements made in the critical assembly were: radial traverses outward from the core; traverses along the walls of

beam tubes; vertical traverses in the ITC; and heating rates and gradients at the planned location of the wall of the pressure vessel.

Relative measurements were typically reproducible to within 5 or 10%. The absolute measurements were subject to an additional uncertainty of $\pm 15\%$ in the determination of the reactor power, and there was also the uncertainty in the spectrum correction factor, amounting to $\pm 10\%$ at the point where the factor was measured. The experimental program was discontinued before this factor was determined more accurately or at more locations. When the errors were combined quadratically, the net uncertainty in the absolute measurements ranged from $\sim 20\%$ near the core to $\sim 35\%$ at a 48-in. radius. Further improvements in the TLD technique could reduce these uncertainties somewhat, but the principal source of error--the power calibration--was unrelated to TLD.

These measurements were in a reflector that is undersized compared with the present AARR design, as indicated in Section VIII.F. The data are useful to indicate the accuracy of computational methods, but cannot be extended to the detailed reflector mockup until experimentation is resumed.



112-9091

Fig. 124. Measured and Calculated Gamma-ray Heating outside the Core

The gamma-ray heating rates to be expected in the critical facility were calculated by McCarthy and Shaftman,³⁰ using simplified geometry and the computer program MAC. A homogeneous core with a flat power distribution was assumed. The calculated heating rate as a function of radial distance from the outer edge of the fuel is plotted in Fig. 124 along with the results of some of the measurements.

Reference 27 contains the details of these measurements, and Refs. 31 and 32 contain general discussions of thermoluminescent dosimetry.

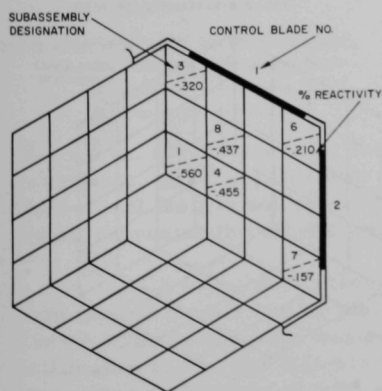
The experimental errors indicated in Fig. 124 represent the estimated reproducibility of the TLD measurements. The experimental curve is also subject to a systematic calibration and spectrum-correction uncertainty, as mentioned

above. Thus there is some indication of disagreement between calculation and experiment in the beryllium region. The discrepancy is worse for the water outside the beryllium. However, the heating rates calculated by some other codes, which have recently become available, indicate that the MAC results are too high and otherwise inconsistent.³³ Thus the significance of the calculated curve in Fig. 124 is questionable. Also, the entire experimental curve is based on a single power calibration. Time did not permit more experiments to confirm the results. Indicative of what might have been found are the two extrapoints plotted at the position of the pressure-vessel wall, which come from two different, independently calibrated measurements. Although the consistency of the three measurements at that position is not as good as one would like, the scatter is not incompatible with the experimental calibration uncertainties. The three measurements were made at different azimuthal locations; how much difference this would make is not known.

D. Experiments to Confirm Loading Predictions

The early loadings were left in the assembly until enough fuel had been received for reloading to the next heavier loading density desired. The delivery of fuel was by relatively small quantities in scattered shipments, so that enough was available to reload a few subassemblies long before the entire core could be reloaded. This permitted tests with one or two heavily loaded subassemblies. An effort was made to confirm the predicted loading of Assembly 4a in advance, because of the long lead time required in ordering fuel, if more should be needed.

A heavily loaded subassembly was substituted for various standard subassemblies to measure the gain or loss in reactivity to be expected for such a loading change. The combination of the subassembly data with that from small samples (see Section IX.J) appeared to permit reasonably accurate predictions of loading requirements. These predictions were in good agreement with calculated values, and also with the fully loaded cores which were assembled later.



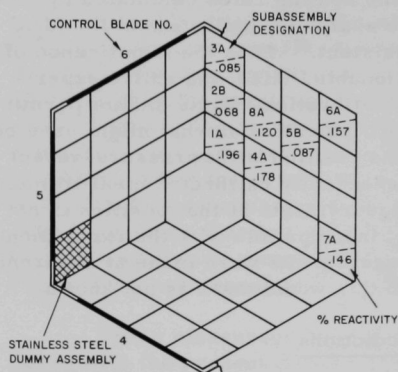
113-1577

Fig. 125. Loss of Reactivity When a 27/54 Type Subassembly Replaced an A Type 14/10 Subassembly in Assembly 2a

In Assembly 2a, a subassembly containing 27 fuel foils and 54 boron stainless steel strips (designated a 27/54 type subassembly) was exchanged with certain of the regularly loaded 14/10 or A-type subassemblies. The results of these substitutions are given by Fig. 125, which shows the positions tested. During these substitutions, control blade No. 1 was entirely withdrawn and No. 2 was fully inserted, affecting the worths at nearby positions.

A-TYPE: (14 FUEL FOILS AND 10 BORON STRIPS)

B-TYPE: (13 FUEL FOILS AND 8 BORON STRIPS)



113-1576

Fig. 126. Gain of Reactivity When a 27/27 Type Subassembly Replaced an A or B Type in Assembly 2a

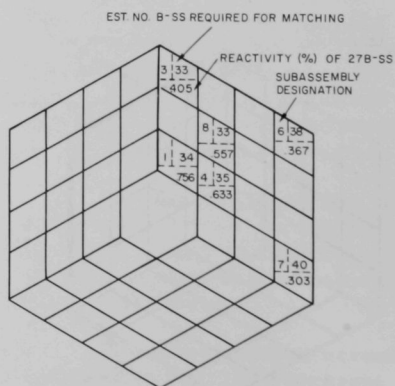
TABLE XL. Worth of Added Boron Strips

	Percent Reactivity by Location Numbers					
	1	3	4	6	7	8
54 Boron Strips/27 Fuel Foils	-0.560	-0.320	-0.455	-0.210	-0.157	-0.437
27 Boron Strips/27 Fuel Foils	0.196	0.085	0.178	0.157	0.146	0.120
Difference	0.756	0.405	0.633	0.367	0.303	0.557

Figure 127 indicates the worth of 27 boron-stainless steel foils and the number estimated by proportionality to match the reactivity of a 27-fuel-foil subassembly to the Type A or B subassemblies in Assembly 2a. This number ranged from 33 to 40, with an average of $35\frac{1}{2}$.

From these measurements we estimated that Assembly 4a should consist of forty-five 27/36 type subassemblies, resulting in a 1215/1620 assembly loading. This was about 2% less reactive than Assembly 2b, but part of the loss in reactivity resulted from a difference in fuel weight and from the additional boron-stainless steel. The loading of Assembly 4a would have

To make a heavily loaded subassembly freely available for further testing, a stainless steel dummy subassembly (i.e., containing stainless steel foils instead of fuel and boron stainless steel) was loaded into Assembly 2a. The subassembly originally in that position was reloaded with 27 fuel foils, 27 boron stainless steel foils, and 27 stainless steel foils. Thus only half as much natural boron (14.05 g) was present as had been used in the measurements indicated by Fig. 125. Figure 126 gives these measurements, and Table XL compares the results in the two figures. Among the differences affecting the comparison was the use of control blades No. 4, 5, and 6 rather than No. 2, with some shadowing of the subassembly designated No. 3 by the partial insertion of blade No. 6.



113-1572

Fig. 127. Estimated Numbers of Boron-Stainless Steel Pieces for Reactivity Matching of 27-fuel-foil Subassembly to A or B Type Subassembly in Assembly 2a

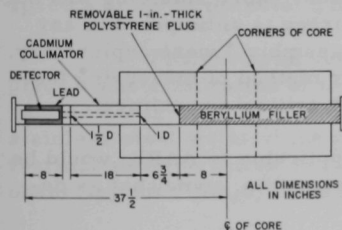
contained about 260 g more ^{235}U if the average weight of the fuel foil were as heavy as that of the 27 fuel foils used for this measurement. With the uranium worth from Table XXXIV as a guide, this accounts for about a fourth of the discrepancy. The extra half boron-stainless steel piece per subassembly accounts for another fourth.

The actual selection of 1620 boron-stainless steel foils for Assembly 4a was influenced by the loading pattern for 36 boron-stainless steel pieces per subassembly, which was more uniform and convenient than for 35 or 37, as examples.

E. Fast-neutron Yields from Beam Tubes

1. Measurement of the Fast-neutron Yield of a Tangential Beam Tube

The fast-neutron component of the beam from a research reactor limits some experiments, because of fast reaction cross sections or susceptibility to radiation damage. The fast flux was measured³⁴ in Assembly 3 using the No. 3 beam tube (10.16 cm sq) indicated by Fig. 82. Figure 128 shows the flux detector position, the lead shielding about the detector, and the position of the beryllium filler in the beam tube. For this experiment, the beam tube was extended by the addition of a thimble of the same size.



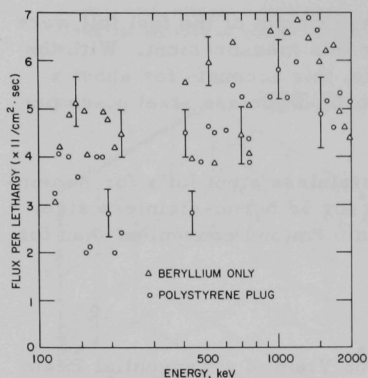
113-1580

Fig. 128. Position of Detector, Collimator, and Through Tube during Measurement of Fast-neutron Yield for Tangential Beam Tube

was 1.5 in. in diameter, and the counter was centered on the axis of the collimator. A solid filler was used to estimate the source of neutrons from the critical facility not associated with the collimator hole (~25%). Spectra shown represent the difference between the two configurations.

A 1-in.-thick piece of polystyrene was placed against the beryllium face of the beam-tube plug, and a measurement made from 100 keV to 2 MeV. The polystyrene was removed, the beryllium was moved toward the collimator so that the distance from the face of the scatterer to the collimator was maintained at 6.75 in., and another spectrum was taken. Figure 129 shows the two spectra.

A proton-recoil counter was placed as shown by Fig. 128. Neutrons from the beryllium filler passed through a compound collimator (see insert of Fig. 83) and were incident upon the counter as shown. The front collimator hole was 1 in. in diameter and was covered with cadmium foil black to thermal neutrons. The rear collimator hole



113-1575

Fig. 129. Yields of Fast Neutrons for Tangential Beam Tubes

the critical facility, which resulted in positioning the detector close to the reactor. Otherwise more gamma shielding would have been used, to reduce the number of counts caused by gamma radiation. More shielding was not feasible in such close quarters. Greater accuracy is anticipated in any future measurements. Those performed in Assembly 3 were exploratory, to determine whether the proportional-counter method of measuring fast-neutron energy distribution was feasible in the critical experiment.

A more accurate measurement, applicable to AARR, would be possible in a detailed reflector and beam tube mockup, somewhat as described in Chapter VIII.

2. Comparison of the Fast-neutron Yields from a Radial Beam Tube and a Tangential Beam Tube

The advantage of a tangential beam tube over a radial tube, as judged by a lower fast-flux yield, was investigated by joint ANL-ORNL measurements³⁵ in the High Flux Isotope Reactor (HFIR). The measured yields were for HFIR radial tube HB-2 and tangential tube HB-3. The advantages found in HFIR are expected to apply to AARR as well, because of the use of beryllium radial reflectors around both cores. Only a synopsis of that work is included in this report because it is expected that a separate report will be issued covering the measurements. This work is much more accurate than was the measurement in the critical experiment, because of the much higher power level. Otherwise the measurement was similar to that described under Section 1 above.

A collimator having an exit hole 3.2 mm (0.125 in.) in diameter and referred to as the "needle beam" was used to reduce the neutron intensity

No corrections for various distortion effects to the spectra were made. The poor data (due chiefly to a bad gamma-to-neutron ratio) does not warrant these corrections, which would probably amount to less than statistics.

The fast-neutron component is only mildly influenced by the polystyrene plug over the energy region covered. The total neutron intensity from 0.1 to 2 MeV is about 130/cm² sec at the power level used for the experiment, which was estimated at 0.1 W. The thermal-neutron flux was roughly double the fast flux.

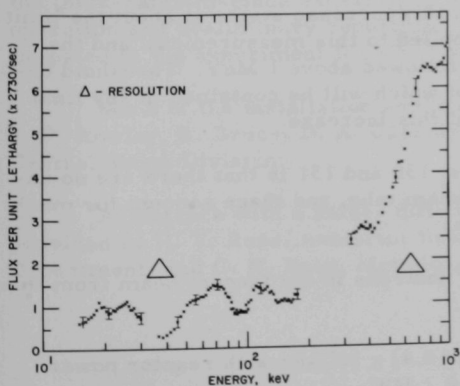
This measurement was hampered by the limited flux level available from

to a level sufficiently low to be acceptable by the proton-recoil counters. A boron shutter (0.47 g of boron per cm^2) was placed across the beam to cut off the thermal neutrons from the counter when observed.

The technique of proton-recoil proportional counting has been described elsewhere.^{36,37} The counters were conventional cylindrical tubes with a five-wire anode. Two counters were used, one to cover the energy region above 100 keV and one for energies below this value. The first was 3.71 cm in diameter and was filled to a pressure of about 3 atm of methane (and nitrogen was added for calibration, to a pressure of 5 cm Hg). The second was 2.54 cm in diameter and was filled to a pressure of about 3.5 atm of hydrogen, which included some methane for quenching and some nitrogen for calibration. The nitrogen calibration was through the $^{14}\text{N}(n,p)^{14}\text{C}$ reaction occurring when thermal neutrons were incident upon the counter. Protons of about 615 keV are released through absorption of thermal neutrons, and these serve to calibrate the observed pulse heights from the counters in terms of proton energy. The counters were aligned perpendicular to the beam (counter axis at an angle of 90° to the beam direction). The beam traversed the counters along a diameter, and the macroscopic scattering cross sections were calculated from the diameters and pressures. Measured spectra refer to the total number of neutrons in the needle beam.

Fast-neutron spectra were measured with the boron shutter in place. The elimination of thermal neutrons reduces the amount of capture gamma background caused by absorption of neutrons in the 0.8-mm-thick stainless steel walls of the counters. The counters were calibrated, and thermal-neutron fluxes were estimated by removing the boron shutter and observing the $^{14}\text{N}(n,p)^{14}\text{C}$ reaction that produces protons of about 615 keV.

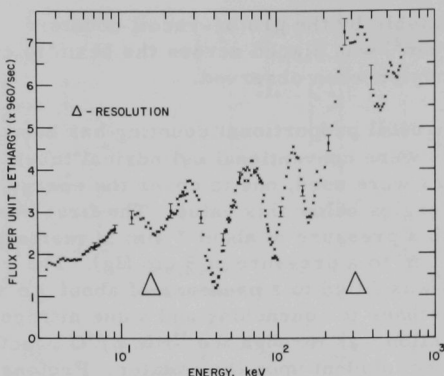
The integrated number of reaction protons was determined, and this number, together with the value of 1.8 barns for the reaction cross section, was used to estimate the thermal-neutron flux in the beam.



112-6306 Rev. 2

Fig. 130. Neutron-energy Distribution, Emergent from Radial Beam Tube of HFIR

The spectra shown by Figs. 130 and 131 are for the radial and tangential beams, respectively, and relate to an operating reactor power of 16.2 MW. Gamma background during the radial measurements was high, and the results are of relatively poor quality (no data exist below 15 keV). The blank region from 200 to 300 keV was caused by a malfunction; the data that would have covered this region were not preserved.



112-6308 Rev. 2

Fig. 131. Neutron-energy Distribution, Emergent from Tangential Beam Tube of HFIR

across the beam path inside the reactor-shield tank to provide a region for flooding the tube as a safety precaution.

Direct $1/v$ absorption of neutrons through the boral shutter, though effectively eliminating thermal neutrons, would not affect the spectrum above 3 keV to any appreciable extent.

A comparison between the radial and tangential spectra indicates that, for energies below about 500 keV, the magnitude and shape of leakage spectra do not differ greatly. A rapid increase in the fast-neutron component above 500 keV is clearly indicated for the radial beam, but not for the tangential beam. Unfortunately, this increase starts at about the limit of the proton-recoil technique as applied to this measurement, and the detail of this increase could not be followed above 1 MeV. Threshold detector measurements, the results of which will be contained in any final summary, should reveal more about this increase.

The significance of Figs. 130 and 131 is that there are no uncollided neutrons in the tangential beam tube, and these account for much of the visible difference in the plots.

An estimate of thermal neutrons in the tangent beam from the $^{14}\text{N}(n,p)^{14}\text{C}$ reaction gave the result:

$$\text{Tangent thermal flux} = (2.6 \pm 0.4) \times 10^5 / \text{sec with reactor power at } 16.2 \text{ MW.}$$

Data for the tangential beam are better; gamma background was less, and more of the low-energy response was recorded. Data above 1 MeV are not reliable because of wall-and-end effects that occur as the range of the recoil-proton track becomes significant relative to the diameter of the counter used.

The spectra appear to possess a rather complicated dependence upon energy. The dips that appear are thought to be related to scattering resonances in aluminum. Aluminum was used widely in construction of the beam tube, and covers of aluminum were placed

ACKNOWLEDGMENTS

The Argonne Advanced Research Reactor Project Physicists, first C. N. Kelber, and later D. H. Shaftman, requested experimental verification of several physics characteristics of the AARR design, and thereby indicated the general program for the resulting critical experiment. Many of the analytical and computational results quoted in this report, for comparison with the experimental measurements, were provided by D. H. Shaftman, R. P. Savio, and A. E. McArthy.

The design and procurement of a core for the critical experiment were started under the direction of S. G. Kaufmann. The experiment was continued by K. E. Plumlee through the safety review, assembly, startup, operation, and final reporting. E. F. Groh prepared much of the design of the core and components and guided the initial installation.

The general areas of activities were as follows among the staff members and their assistants in the critical experiment: G. S. Stanford--flux and power distributions, spectral indices, and thermoluminescent dosimetry measurements; J. W. Daughtry--Rossi-alpha, pulsed-neutron, and small-sample reactivity measurements; W. R. Robinson--void worths, temperature coefficients, and assistance with flux and power measurements; R. A. Schultz--electronic maintenance and instrumentation for the reactor and many experiments, as well as assistance in many measurements; T. W. Johnson--assistance with thermoluminescent dosimetry, beam-tube measurements, and many other experiments; F. F. Kodrick--mechanical upkeep, fuel records, and participation in many experimental runs; F. H. Martens (available for a brief time only)--the ITC safety liner, and the thick-hafnium-blade experiment; J. W. Armstrong--assistance with operation and preliminary reporting. H. F. Reed and A. R. Boynton participated in the experiment for short periods.

Much of the installation and many components were provided by J. P. Rowley, R. Bruce, D. A. Cassidy, C. Kotora, and A. Siebert of the Central Shops Division.

Assistance with a rather difficult fuel-procurement contract was provided by H. V. Ross, Assistant Business Manager; H. L. Walner, Legal Department; and C. H. Bean, Metallurgy Division.

REFERENCES

1. J. W. L. de Villiers (ed.), *Critical Experiments for the Preliminary Design of the Argonne High Flux Reactor*, ANL-6357 (June 1961).
2. D. H. Shaftman and R. P. Savio, "Argonne Advanced Research Reactor (AARR)," *Seminar on Intense Neutron Sources*, CONF-660925, p. 215 (Sept 1966).
3. K. E. Plumlee, *Flux Trap Experiments in D₂O-moderated Thoria-Urania Cores*, ANL-6915 (Oct 1964).
4. E. M. Pennington, *Calculations for ZPR-VII Flux-trap Reactors with Heavy Water-moderated Cores*, ANL-6406 (Aug 1961).
5. *ANL Reactor Development Program Progress Report: December 1965*, ANL-7132, p. 66 (issued Jan. 25, 1966).
6. R. P. Savio and D. H. Shaftman, "Argonne Advanced Research Reactor Calculations--Analysis of the Critical Experiments," Paper No. II-17, *Reactor Physics Division Annual Report: July 1, 1965 to June 30, 1966*, ANL-7210, pp. 80-82 (Dec 1966).
7. F. H. Helm, *Numerical Determination of Flux Perturbation by Foils*, Nucl. Sci. Eng. 16, 235-238 (June 1963).
8. W. R. Robinson and G. S. Stanford, "Argonne Advanced Research Reactor Critical Experiments--Activation and Power Distribution Measurements," Paper No. II-12, *Reactor Physics Division Annual Report: July 1, 1965 to June 30, 1966*, ANL-7210, pp. 59-70 (Dec 1966).
9. C. H. Westcott, *Effective Neutron Cross Sections for Well-moderated Thermal Reactor Spectra*, AECL-1101 (CRRP-960) (Nov 1960).
10. G. M. Jacks, *A Study of Thermal and Resonance Neutron Flux Detectors*, DP-608 (Aug 1961).
11. N. P. Baumann, *Resonance Integrals and Self-shielding Factors for Detector Foils*, DP-817 (Jan 1963).
12. B. G. Chidley, R. B. Turner, and C. B. Bigham, *Neutron Temperatures in a CANDU-type Power Reactor*, Nucl. Sci. Eng. 16, 1, 1963.
13. A. E. McCarthy, P. J. Persiani, B. I. Spinrad, and L. J. Templin, *ANL Reactor Physics Constants Center Newsletter No. 1, Neutron Resonance Integral and Age Data* (1961).
14. E. J. Axton and T. B. Ryves, *Scattering Resonance Shelf-shielding Correction for Manganese Sulphate Solutions*, J. Nucl. Energy 21, 543 (1967).

15. "Experiments on Neutron Spectra," *Reactor Physics Constants*, ANL-5800 (Second Edition), pp. 91-98 and Table 3-5 (July 1963).
16. K. E. Plumlee and M. T. Wiggins, *Automatic Foil Activity Counting Facility and Data-reduction Program*, ANL-6628 (Oct 1962).
17. G. S. Stanford, *The Codes NURF, COMBO, and TWO SORCE for Processing Foil Counting Data*, ANL-7356 (1967).
18. R. H. Lewis, T. C. Engelder, D. M. Roberts, and D. M. Wehmeyer, *Thermal Activation Method for ρ^{28} Measurements in Slightly Enriched Uranium Oxide Lattices*, BAW-1268 (1963).
19. G. S. Stanford, "Determination of the K-constant for the Dysprosium Substitution Method," Paper No. V-12, *Reactor Physics Division Annual Report: July 1, 1965 to June 30, 1966*, ANL-7210, pp. 325-327 (Dec 1966).
20. G. S. Stanford, "Attenuation of Epicadmium Neutrons by Cadmium Foil Covers," Paper No. IV-11, *Reactor Physics Division Annual Report: July 1, 1963 to June 30, 1964*, ANL-7010, pp. 203-206 (Jan 1965).
21. G. S. Stanford, K. E. Plumlee, and W. R. Robinson, "Linear Relationship between Cadmium Ratio and Reactor Core Moderating Ratio," *Reactor Physics Division Annual Report: July 1, 1964 to June 30, 1965*, ANL-7110, pp. 31-34 (Dec 1965).
22. G. S. Stanford and K. E. Plumlee, *Linear Relationship between Cadmium Ratio and Reactor Core Composition*, Trans. Am. Nucl. Soc. 8, 1 (1965), pp. 270-271.
23. H. Kouts, *Beam Tube Design for the High Flux Beam Reactor*, J. Nucl. Energy 17, p. 153 (1963).
24. C. N. Kelber, *Enhancement of Experimenters' Fluxes in the Argonne Advanced Research Reactor*, Trans. Am. Nucl. Soc. 6, 1, p. 5 (1963).
25. *Handbook of Chemistry and Physics*, Chemical Rubber Publishing Co., 46th ed., p. F-4.
26. W. C. Davidon, *Variable Metric Method for Minimization*, ANL-5990 (Rev.) (Nov 1959).
27. G. S. Stanford and T. W. Johnson, *Determination of Gamma-ray Heating in a Critical Facility by Thermoluminescent Dosimetry*, ANL-7373 (Feb 1968).
28. L. H. Gray, *An Ionization Method for the Absolute Measurement of γ -Ray Energy*, Proc. Roy. Soc. (London), 1936, A-156, pp. 578-596.
29. L. V. Spencer and F. H. Attix, *Theory of Cavity Ionization*, Radiation Research 3 (1955), pp. 239-254.

30. A. E. McCarthy and D. H. Shaftman, Argonne National Laboratory (private communication).
31. F. H. Attix, *Present Status of Dosimetry by Radiophotoluminescence and Thermoluminescence Methods*, NRL-6145 (1964).
32. Z. Spurny, *Thermoluminescent Dosimetry*, At. Energy Rev. 3, No. 2, pp. 61-115 (1965).
33. D. H. Shaftman, Argonne National Laboratory (private communication).
34. E. F. Bennett, "Neutron Beam Spectra Extracted from the High Flux Irradiation Reactor," Paper No. II-7, *Reactor Physics Division Annual Report: July 1, 1965 to June 30, 1966*, ANL-7210, pp. 45 and 46 (Dec 1966).
35. E. F. Bennett, Argonne National Laboratory (private communication).
36. E. F. Bennett, *A Study of the 1/E Slowing-down Neutron Spectrum Using 4π -recoil Proportional Counters*, ANL-6897 (Sept 1964).
37. E. F. Bennett, *Fast Neutron Spectroscopy by Proton-recoil Proportional Counting*, Nucl. Sci. Eng. 27, 16-27 (1967).

ARGONNE NATIONAL LAB WEST



3 4444 00011243 3